Nanoscale Advances

REVIEW

View Article Online
View Journal | View Issue

Cite this: *Nanoscale Adv.*, 2023, **5**, 5717

Comprehensive advances in the synthesis, fluorescence mechanism and multifunctional applications of red-emitting carbon nanomaterials

Tuhin Mandal, [ab] Shiv Rag Mishra[ab] and Vikram Singh *[ab]

Red emitting fluorescent carbon nanomaterials have drawn significant scientific interest in recent years due to their high quantum yield, water-dispersibility, photostability, biocompatibility, ease of surface functionalization, low cost and eco-friendliness. The red emissive characteristics of fluorescent carbon nanomaterials generally depend on the carbon source, reaction time, synthetic approach/methodology, surface functional groups, average size, and other reaction environments, which directly or indirectly help to achieve red emission. The importance of several factors to achieve red fluorescent carbon nanomaterials is highlighted in this review. Numerous plausible theories have been explained in detail to understand the origin of red fluorescence and tunable emission in these carbon-based nanostructures. The above advantages and fluorescence in the red region make them a potential candidate for multifunctional applications in various current fields. Therefore, this review focused on the recent advances in the synthesis approach, mechanism of fluorescence, and electronic and optical properties of red-emitting fluorescent carbon nanomaterials. This review also explains the several innovative applications of red-emitting fluorescent carbon nanomaterials such as biomedicine, light-emitting devices, sensing, photocatalysis, energy, anticounterfeiting, fluorescent silk, artificial photosynthesis, *etc.* It is hoped that by choosing appropriate methods, the present review can inspire and guide future research on the design of red emissive fluorescent carbon nanomaterials for potential advancements in multifunctional applications.

Received 23rd June 2023
Accepted 12th September 2023

DOI: 10.1039/d3na00447c

rsc.li/nanoscale-advances

1. Introduction

Fluorescent carbon nanomaterials (FCNMs) are a predominant star of the new era among fluorescent nanomaterials, which

[a]*Environment Emission and CRM Section, CSIR-Central Institute of Mining and Fuel Research Dhanbad, Jharkhand, 828108, India. E-mail: vikku.010@gmail.com; vikramsingh@cimfr.nic.in*

[b]*Academy of Scientific and Innovative Research (AcSIR), Ghaziabad, 201 002, India*

Mr Tuhin Mandal received his BSc and MSc degrees in chemistry from Guru Ghasidas Vishwavidyalaya, Bilaspur, India in the year 2016 and 2018 respectively. He also completed his Bachelor of Education degree from Burdwan University in 2020. Currently, he is working as a research scholar under the guidance of Dr Vikram Singh at the Environment Emission and CRM section in the CSIR-Central Institute of Mining and Fuel Research, Dhanbad. His research mainly includes the 'Synthesis of fluorescent carbon nanomaterials from coal and its derivatives'.

Mr Shiv Rag Mishra completed his BSc (2003) and MSc (2005) in chemistry at Bundelkhand University, Jhansi, India. He also qualified for the UGC-CSIR NET examination in Chemical Science (2010). He is a regular employee (Assistant Professor) of D. V. P. G College, Orai, UP, India and for his doctoral study, he joined the Environment Emission and CRM section, CSIR-Central Institute of Mining and Fuel Research Dhanbad as a research scholar under the supervision of Dr Vikram Singh in Aug 2022. His research interest focuses on the 'Development of fluorescent carbon nanomaterials for white-light-emitting devices'.

griped a lot of scientific attention for the promising area of research over the past few decades. The FCNMs have a lot of advantages such as biocompatibility, cost-effectiveness and environmental friendliness over the conventional semiconductor nanocrystals, organic dyes and rare earth-based fluorescent materials. These advantageous properties make them potential candidates for biomedical applications such as medication administration, biosensing, optical imaging, and cell labeling. Apart from biomedical applications, FCNMs are also widely used in various technologies such as light-induced catalytic water splitting, optoelectronics, photocatalysis, sensing, anti-counterfeiting, *etc.*[1–8] Numerous types of FCNMs have been developed so far. However, the majority of them only exhibit an intense blue-to-green fluorescence short emissive spectrum when excited by ultraviolet light. The majority of carbon nanomaterials (CNMs) show bright fluorescence in the blue-green region, whereas they show comparatively poor quantum yields in the red region under ultra-violet light exposure. The application of blue emitting CNMs has various disadvantage in biomedical applications and in the fabrication of white light emitting devices such as the interference of autofluorescence of the biological matrix and retinal damage by blue dominating light-emitting diode (LED) chips, respectively. As a result, such disadvantages limit their potential uses, notably in the realms of biomedical and other potential applications in various fields.[1,9–16]

Recently, red-emitting CNMs have gained a lot of attention from the scientific community because of their deep tissue penetration, minimum autofluorescence, large Stokes shift, low photon scattering and long fluorescence lifetime. The red emitting CNMs are very essential materials for developing warm white light-emitting diodes (WLEDs) with a high colour rendering index (CRI > 80) and low correlated colour temperature (CCT 4000 K), which prevent eye tiredness and eye toxicity. These advantages are successfully applied in a variety of fields for the sustainable development of society and help to overcome the drawbacks of short wavelength emissive FCNMs.[17–26]

The synthesis of red/infrared emitting CNMs with high quantum yields is crucial and the origin of their fluorescence is still a matter of debate. The fluorescence originates in CNMs may be due to the presence of sp^2-conjugation units, surface defects, quantum confinement, crosslinked enhance emission and the presence of heteroatom containing functional groups. The tunability in the fluorescence emission of CNMs also depends on the type of precursor, reaction conditions, solvents, purification and post-treatment. The size of isolated sp^2 domains, hydrophilicity, the level of oxidation, surface charges, surface functional groups and heteroatom doping are also regarded as important factors for shifting the emission in the red region.

In this review, we have compiled a comprehensive overview of existing and emerging research techniques, choice of carbon-rich precursors, fluorescence mechanisms and factors affecting the optical properties to achieve red emission. Furthermore, we have explored the applications of red emitting CNMs in various fields such as biomedicine, optoelectronics, photocatalysis, chemical sensing, solar technology, anticounterfeiting, fluorescent silk, artificial photosynthesis, fluorescent nanothermometers, *etc.*

Dr Vikram Singh received his PhD degree in Chemistry from the Indian Institute of Technology Madras in Jul 2016. After completing his doctoral research, he worked as a National-PDF (SERB) and Institute-PDF at CSIR-CDRI Lucknow (2016–2018) and IIT Kanpur (2018–2021) respectively. He has been awarded various prestigious awards such as the 'Langmuir Best PhD Thesis Award in Physical & Theoretical Chemistry' at IIT Madras, 'Gandhian Young Technological Innovation Award' at Rashtrapati Bhawan New Delhi, etc. He has published more than 20 scientific articles in leading peer-reviewed journals and patents. Currently, he is working as a Scientist in the Environment Emission and CRM section, CSIR-Central Institute of Mining and Fuel Research Dhanbad. His research group focuses on the development of fluorescent carbon nanomaterials using green and cost-effective processes for biomedical, energy and environmental applications.

2. Synthesis of red-emitting FCNMs

Red emissive fluorescent carbon nanomaterials can be achieved using surface and conjugation chemistry. The optical properties of FCNMs depend on the presence of auxochromes at the surface and the type of conjugation present in the carbon core. Increasing the number of sp^2 hybridized carbon atoms, oxide surface content, nitrogen and sulfur heteroatoms results in the shifting of wavelengths towards the longer wavelength region. It is very crucial to choose cost-effective and environmentally friendly carbon precursors, solvents and methods for the synthesis of red emitting CNMs by employing two classified processes: top-down and bottom-up (Fig. 1).

2.1. Crucial aspects for the synthesis of red-emitting FCNMs

Various factors such as carbon precursors, methodology (reaction conditions), surface functionalization, and purifying FCNM blend influence the emission properties of FCNMs. Therefore, researchers are making significant attempts to synthesize extremely effective FCNMs that can emit in the longer wavelength region.

2.1.1. Organic-based precursor. The choice of organic precursors is one of the most important causes to achieve red emission as it decides the structure and functional groups of FCNMs. In this regard, a variety of precursors have been described in the literature for the synthesis of red emitting CNMs ranging from bulk carbon materials to tiny organic molecules including aromatic compounds and biomass. These

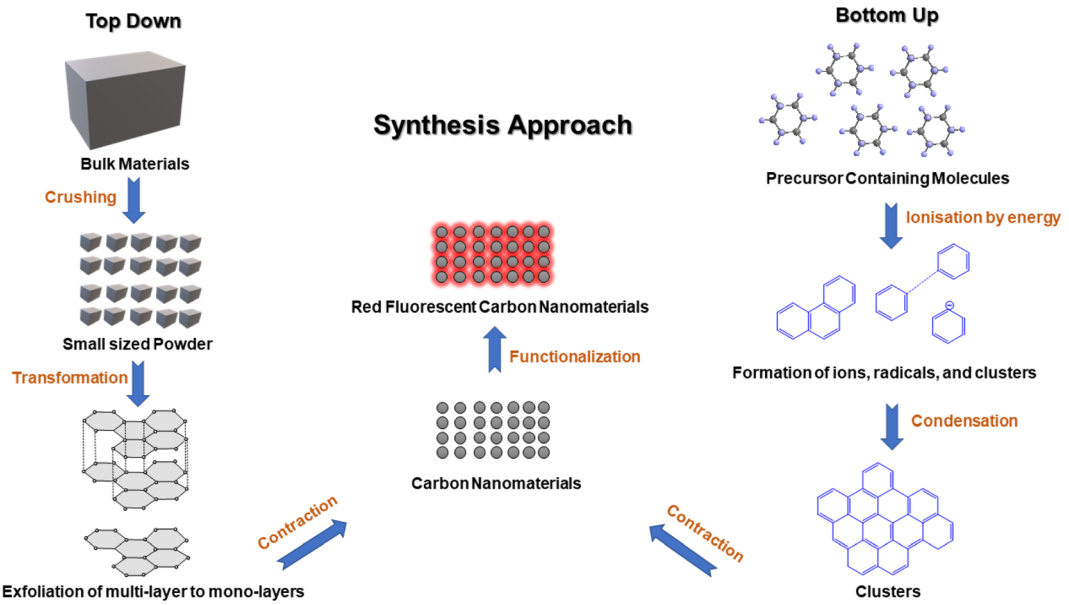

Fig. 1 Schematic representation of the synthesis approach.

precursors influence the optical characteristics of the final product. The new energy levels might be introduced in the visible region, mainly towards the red region by doping with heteroatoms, auxochromes and sp^2 core structures. The FCNMs aromatized themselves and hence the bandgap of FCNMs automatically is close to sp^2 domain bandgaps. These methods are advantageous for adjusting the absorption and emission of FCNMs to the long-wavelength region.

2.1.1.1. Large organic materials. Organic materials made of bulk carbon are typically non-luminescent because the band gap transitions either did not occur or occurred outside the UV-visible region. Only the organic compounds with nanoscale carbon can emit fluorescence as the band gap transition occurs in the UV-visible region.[27–29] As technology advances, specific larger organic materials, including coal, graphene oxide, graphite, carbon fibers, tyre soot, and carbon nanotubes, have been employed as a precursor through a top-down and a bottom-up process.[30–32] The prepared FCNMs showed a broad emission profile, excitation dependent emission and solvent concentration-dependent properties.[33,34] The tunable emission suggests that the fluorescence is originated from the defect state emission and the excitation-dependent emission from the sp^2 clusters in carbon cores.[35–37] The FCNMs with abundant oxygen, nitrogen and sulfur-related functional groups showed broad excitation-dependent emission spectra with moderate quantum yields and nanosecond fluorescent lifetimes.[38,39] Song *et al.* developed humic acid mixed coal-derived multicolor carbon dots by using solvothermal treatment in dimethyl formamide for utilization as a cold white light emission material.[40] Hu *et al.* reported a red colour fluorescent center *via* embedding phosphorus on the surface of carbon dots, which were developed from coal using diammonium phosphate. The synthesized carbon dots were used as a ratiometric fluorescent probe for the determination of the pH of metal-complex systems.[41] Tripathi *et al.* synthesized green to red and near infrared multicolour emissive carbon dots from diesel-based pollutant carbon soot through a reflux reaction in the presence of concentrated nitric acid for 10 hours. The as-prepared carbon dots had been used for the imaging of *Escherichia coli* and the sensing of cholesterol.[42] Meng *et al.* reported red to blue multicolour fluorescent carbon dots from coal tar pitch using a mixture of formic acid and hydrogen peroxide. The as-synthesized red carbon dots showed a shift of their emission wavelength to the blue region with increasing the degree of the reduction process.[43] Ko *et al.* demonstrated oxidative treatment of tire carbon soot using nitric acid to develop infrared emissive carbon dots. The carbon dots showed excitation dependent fluorescent emission with the excitation range of 430 nm to 710 nm and were used as a fluorescent probe for the bioimaging of cancer bearing cells.[44] Tan *et al.* produced red-emitting fluorescent carbon dots *via* an electrochemical reaction of graphite in potassium persulfate solution. The red emission was attributed to the lower energy gap, caused by the larger sp^2 domain. The carbon dots were applied for the bioimaging of HeLa cells.[45] Tunable red carbon dots were prepared *via* an oxidative reaction of carbon fibers in nitric acid followed by ultrafiltration. The tunability in the emission wavelength was caused by the surface state electronic transitions and the size of the carbon dots.[46] Ke *et al.* reported a one-pot synthesis method of red emissive graphene quantum dots from graphene oxide *via* a hydroxyl radical and heteroatom doping technique, using ammonium hydroxide and thiourea-mediated dissociation of hydrogen peroxide.[47]

2.1.1.2. Small organic materials. Small organic molecules are amorphous or crystalline and made of a lot of polar functional groups and often employ bottom-up techniques, mainly solvothermal and hydrothermal for the preparation of FCNMs.[48–51] Amino acids, citric acids, naphthalene,

saccharides, phenylenediamines, polythiophene, *etc.,* are the most frequently employed small organic materials to synthesize far-red or near IR emissive CNMs.[52,53] Citric acid has a carboxylic functional group, which rapidly reacts with nitrogen containing amino groups to form fused α, β or α, γ bi-amines. This alkylation reaction results as the increasing of carbonization degree with nitrogen content, continuing the formation of –C=C–, –C=N–, –C=O–, and –C–NH– bonds to produce 2-pyridone fused large organic rings, followed by the reduction of the band gap between the HOMO and LUMO. This outcome brings about a noticeable red shift in emission spectra as a contribution of multiple emission centers and the different types of bonds. Hence, the blend of citric acid and polyamines can be used as a precursor to synthesize an N-doped sp^2 core, responsible for far red or near IR FCNMs.[25,54–60]

Similarly, amino acids contain both amino and carboxylic acid groups and are used as suitable precursors for the synthesis of far red or near IR FCNMs. Several derivatives of amino acids contain nitrogen and sulfur heteroatoms, enrich the electronic states and facilitate the generation of in-gap states that could act as non-radiative and recombination centers. As a result, it showed a strong bathochromic shift in emissions.[61–63]

Aromatic precursors having multiple rings (two or more) or –R–NH–, –OH, and –R–S–H polar functional groups as substituents are also important for the development of red emissive CNMs. Poly-benzene ring containing aromatic precursors have produced a large number of conjugated sp^2 domains in their core by dehydration and carbonization mechanisms. The conjugated sp^2 core reduced the energy level between the HOMO and LUMO, which shifts the excitation and emission wavelength towards the red region.[64–68] Aromatic precursors consisting of aromatic amines, phenols and polythiophene derivatives are dominating precursors for red emissive CNMs, since there are many options and definable chemical structures. The presence of a stiff π-conjugated skeletal structure with the passivation of the –R–NH–, –OH, and –R–S–H functional groups on the surface plays a vital role in the induced charge transfer excited state in the π-conjugated systems of FCNMs with the formation of π-type and n-type carriers. As a result, it contributes to narrowing the optical band gap of FCNMs, followed by the emission in the far red or near IR region with high fluorescence quantum yield.[69–74]

Other atoms like selenium, boron, and fluorine are also utilized for shifting the wavelength to the red region after doping at edges on the surface of the organic precursor. The band gap is opened by the incorporation of these heavy atoms into the carbon core. It also weakens the nonradiative recombination through the increase of surface defects. The fluorine has the highest effect among heavy atoms due to the electron-withdrawing capacity of fluorine, decreases the energy gap between the HOMO and LUMO, and leads to the shifting of excitation and emission wavelengths towards the red region.[75–80] Li *et al.* developed tetraphenyl porphyrin-derived red-emitting carbon dots *via* a simple solvothermal method using a sulfonation reaction with sulfuric acid. The developed carbon dots were utilized for the bioimaging of HeLa cells.[81] Shao reported highly water-dispersible red fluorescent carbon dots from glutathione as a precursor using a solvothermal method. The carbon dots showed intense near infrared emission with a very narrow emission band and were utilized for the sensing of carcinoembryonic antigens in pleural effusion.[82] Zhao *et al.* synthesized near-infrared emissive carbon dots with a large conjugated sp^2 core. The charge transfer properties between the electron donor and acceptor lead to the longer wavelength absorption of the carbon dots. The as-synthesized carbon dots were used for photothermal therapy and multiphoton therapy.[83] Ji *et al.* synthesized microwave-assisted near infrared carbon dots from *o*-phenylenediamine through a hydrothermal method. The developed carbon dots showed a red-shift *via* protonation, while deprotonation resulted in a three times higher quantum yield, and were demonstrated as a red phosphor.[84] Geng *et al.* produced tunable green to red emissive fluorescent carbon dots from citric acid and *m*-aminophenol *via* a microwave irradiation method. The carbon dots exhibited excellent competence of biocompatibility properties and were utilized for bioimaging.[85] Wei *et al.* developed blue, green, yellow, and orange multicolour emitting carbon dots from a mixture of glucose and amino acid *via* a microwave-assisted Maillard reaction. The multicolour emission of the carbon dots originated from the carbon cores and the surface defect states. The teams reported that the emission of the carbon dots could be controlled by modifying the precursors. They also showed that the carbon dots were also applied for multicolour display and cell imaging.[86] Li *et al.* reported *p*-phenylenediamine and hydroquinone derived red fluorescent carbon dots *via* a mild solvothermal treatment by merely changing the relative ratios of the precursors, which were used for the detection of Fe^{3+} and pyrophosphate.[87] Wang *et al.* produced red fluorescent carbon dots *via* a surface modification with polyetherimide through a microwave heating technique. This synthesis technique promotes the surface charges from negative to positive and shielding the red colour emission from being quenched by water. These characteristics encourage bioimaging and cell absorbtion.[88] Niu *et al.* produced phloroglucinol and boric acid derived excitation dependent boron doped red carbon dot powder. The red carbon dots exhibited solid state fluorescence and showed intense red fluorescence under UV light excitation and were utilized for fingerprint detection.[89]

2.1.1.3. Renewable organic materials. An organic material that can be recycled from both plants and animals is called biomass. So, it is a renewable organic material.[90–92] Cellulose is the most plentiful organic compound present in this world and the main component of biomass. It is a complex carbohydrate composed of chiral carbon, oxygen and hydrogen.[93–96] Biomass is one of the most commonly used carbon precursors for the development of red-emitting CNMs using solvothermal and hydrothermal methods. The optical properties of biomass-derived red emissive CNMs depend on the excitation and the functional groups of the solvent used. The addition of sulfinyl and carbonyl functional groups on the surface leads to the rising of discrete energy levels due to the gaining of oxygen atoms and losing of electrons on the surface. These processes

boost the absorption in the red region or near the IR region and increase the red fluorescence.[97–104] Zhang *et al.* fabricated *Arabidopsis thaliana*-derived nitrogen and sulfur co-doped multicolour carbon dots through a Maillard reaction using sulfuric acid. The developed red carbon dots exhibited excellent biocompatibility, fluorescence properties, and solubility. The team used the carbon dots for the labeling and imaging of a plant.[105] Liang *et al.* developed rose red emissive fluorescent carbon dots from wedelia trilobata biomass *via* microwave-assisted solvothermal treatment using ethanol and water solution. The red carbon dots were used for the detection of glutathione and the imaging of cells.[106] Tang *et al.* synthesized red emissive carbon dots from black pepper through a solvothermal method. The red carbon dots showed strong biocompatibility, selectivity, sensitivity and low toxicity. These properties of the as-synthesized carbon dots were utilized for the sensing and imaging of ascorbic acid in living cells.[107] Zhang *et al.* synthesized red fluorescent carbon dots from herbaceous *Andrographis paniculata via* solvothermal synthesis using ethanol. The carbon dots were used as a smartphone integrated green optosensor.[108] Wang *et al.* derived blue-to-red emissive fluorescent carbon dots using solvothermal methods from spinach. The modification of the boiling point and polarity of solvents causes the red-shifted emission. The team used the as-synthesized carbon dots for the anticounterfeiting and the sensing of Cr^{6+}.[109] Tariq *et al.* reported microwave-assisted fig biomass extracted red emissive carbon dots, which exhibited excellent antibacterial properties and were used as a antibacterial agent for the diagnosis of bacterial infection.[110] Yang *et al.* developed glutathione-supported waste tobacco leaf-derived red emissive fluorescent carbon dots *via* a simple hydrothermal method. The red carbon dots exhibited large stoke shift with the advantages of selective and sensitive detection of analytes.[111] Zhang fabricated red, green and blue emissive fluorescent carbon dots using a solvothermal method from waste leather scrap. The size of the carbon atoms and the functional group cause the addition of a new energy level for electronic transition, leading to red fluorescence emission.[112]

2.1.2. Reaction conditions. The shifting of the fluorescent emission wavelengths of the FCNMs heavily depends on the reaction circumstances. With the knowledge of exploring the optical characteristics of FCNMs with solvents, time, temperature, pH and the reactants ratio, one can achieve red emissive CNMs.[1,113–115] Solvent-influenced emission behavior can be established by choosing the solvent. The solvent may be protic or aprotic, and sometimes polar or nonpolar. The addition of aprotic solvents to the organic precursor causes increase in dehydration and the carbonization process. Consequently, this process led to the formation of sp^2 conjugated carbon domains in the core of the FCNMs, resulting in a red shift in the emission wavelengths.[116–121] The reaction temperature affects the carbonization degree and the dehydration condensation of the synthesis process of the FCNMs. The rising temperature contributes to increasing carbonization degree and dehydration of the FCNMs, resulting in the loss of the auxochromes on the surface. However, increasing temperature results in a permanent loss of fluorescence because it reduces the intensity of the fluorescence, gradually.[122–126] The elevated temperature also increased the rate of the reaction process of FCNMs. The motion of the atoms of the organic material collides frequently with each other as a result of the elevated temperature.[127] The reaction time influences the degree of synthesis process completion of FCNMs, greatly. The reaction between the organic materials is more significant with a longer reaction time but excessive time follows the overreaction. The excessive time did not encourage the production of unlimited FCNMs.[128–130] Varying reactant concentrations and ratios will directly impact the surface functional groups of FCNMs.[131] An acidic environment leads to the red shift of the emission wavelength, while an alkali environment leads to the blueshift of the emission wavelength.[132] Khan *et al.* reported excitation-dependent multicolour fluorescence emission spectra of carbon dots on a nanosecond time scale.[133] pH-dependent blue to red emissive carbon dots are achieved by changing the acid–base behavior of the group present on the surface.[134] Zhao *et al.* developed red, green and blue emitting carbon dots with excitation-dependent emission properties. The tunability in emission spectra is due to the conjugation and presence of oxygen atoms.[135] Yang *et al.* demonstrated sulfuric acid assisted blue to red-shifted emission of carbon dots caused by the surface-defected state and the carbonization degree.[136]

2.1.3. Purifying FCNM blend and post-modification. Following the top-down and bottom-up treatment of carbon precursors, various sizes of FCNMs are created as a product. The mixed FCNM solution generated an overlapping fluorescent emission spectrum.[137–139] So, it is necessary to purify the mixture of FCNMs by the size or size/charge ratio.[140] Various sizes with different functional groups of FCNMs possess different significant photophysical properties.[141,142] One can get red emissive CNMs easily by using effective techniques for separating and purifying the synthetic mixtures of FCNMs to get certain sizes of fluorophores or groups of fluorophores, responsible for the red emission.[143–145] The most common methods used for the separation and purification of synthetic mixtures of FCNMs are filtration, centrifugation and dialysis.[146–149] Large particles (*i.e.*, soot) are frequently removed from derived FCNM suspensions using centrifugation and filtration,[99,150,151] whereas low molecular weight entities are removed using dialysis.[14,152,153] Particularly, the centrifugation techniques help to achieve the different core sizes of the same mixture of FCNMs.[154–156] Size exclusion chromatography and gel electrophoresis methods are also used for the separation and purification of the synthetic mixtures of FCNMs.[157–159] FCNMs with different sizes have different bandgap widths, resulting in different photo-luminescence (PL) emission peaks. When the size of the FCNMs increases, their band gap energy continuous to decrease and photons are more likely to transition, which results in a bathochromic shift (red shift) of the PL emission peak.[160–162] Alternatively, the addition of functional groups on the surface of the FCNMs can generate abundant structural configurations and introduce new energy levels into their electronic structures. Therefore, more opportunities for an electronic transition arise, which is followed by a tunable emission of FCNMs. The increase of nitrogen-containing amino groups, graphitic nitrogen cores and carboxylic

groups on the surface of the FCNMs leads to the bathochromic shift.[163–169] Sometimes post-modification treatment has a significant impact on the optical properties of FCNMs. Nitrogen functionalization, dehydration and strengthening the π-conjugation, *etc.*, were used as post-modification treatments to get red emissive CNMs.[170–175] Wang *et al.* reported blue to red color fluorescent carbon dots through a slight modification of the reaction conditions including temperature and pH. The multicolour emitting carbon dots were utilized as a white light emitting diode with a high colour rendering index.[176] Yang *et al.* synthesized red emissive fluorescent carbon dots which showed the shifting of emission wavelength towards longer regions by adding $NH_3 \cdot H_2O$. The nitrogen group of the amine water solution formed a conjugated amide ring causing the red-shifted emission.[177] Tetsuka *et al.* shifted the emission of nitrogen-functionalized graphene quantum dots from blue to red in the post-modification method.[171] Lyu *et al.* showed the shift of blue fluorescence to green, green to yellow, yellow to orange and orange to red for graphene quantum dots *via* enhancing the π-conjugation and the graphitic nitrogen by chemical modification. The team showed that the carbon dots were utilized for a highly photostable white light emitting composite film and bioimaging of liver cancer cells.[178] Zheng *et al.* developed a post-modification technique to shift the fluorescence emission of carbon dots from blue to green and red. The group introduced auxochrome nitrile and carbonyl groups to shift the emission to the red region.[179]

Thus, these demonstrated aspects including choosing organic precursors, reaction conditions and purifying the FCNM blend with post-modification techniques are so vital to focus for the development of red-emitting CNMs (Table 1).

3. Fluorescence mechanisms of red-emitting FCNMs

The fluorescence mechanism is so important to explore the red region and near IR region very widely. Recognizing the fluorescence mechanism is essential for obtaining FCNMs with the desired optical properties. However, it is still challenging to understand the precise fluorescence process of red FCNMs. Numerous plausible theories have been put out to increase the understanding of red fluorescence origins.

3.1. Quantum confinement effect

The significant characteristics of FCNMs are responsible for the featured optical properties. Bandgap transition is one of the most fundamental methods, engineered in the conjugated π-domain for achieving the quantum confinement effect.[203–205] The quantum confinement effect occurs when FCNMs have a smaller size than the exciton Bohr radius.[206,207] The phase "quantum confinement" means the energy of confined electrons. When the potential dimension comes close to the de Broglie wavelength of the electron, the confined electron wavefunction of nanomaterials emerged as a discrete set of energy levels. The changes are named "quantum confinement". It has an impact on material behavior in terms of electrical, optical, and mechanical properties of nanomaterials.[208–211] When nanomaterials are compressed to sizes and shapes of 100–10 nm or even smaller, the quantum confinement phenomenon takes place. These modifications are brought about by a distinct set of electron energies and lead to size confinement. Solid-state physics states that the energy band gap is split into the valence band and conduction band. The absorption of photons or the thermal excitation supplies adequate energy to the valence band electrons to surpass the energy gap and transit to the conduction band. As a result, holes act as a positive charge and are created at that place of the surpass electrons. The hole might be filled by an electron from the valence band, leaving another hole in its stead. In this way, the holes travel to the conduction band. Excitons are developed when electron and hole pair combinations occur.[212–220] When the size of the three-dimensional materials is reduced to the nanoscale, the band gap expands. It causes the electronic transition between the band gaps in the ultraviolet to visible range and sometimes in the infrared region.[221–223] Nanosized carbon cores containing conjugated π-domains with significant functional groups produce multicolour fluorescence due to the quantum confinement effect, one of the main mechanisms among the others.[224–226] It is plausible to tweak the characteristic bandgap transition by modifying the size of the π-domains. The increase in the size of the π-domain carbon core causes a smaller bandgap. As a result, a redshifted emission wavelength is noticed.[46,227,228] The valence band of the carbon core is separated from the conduction band by the conjugated π-domains of finite size. When there is an excess population of electrons and holes, a direct transition of the electrons present in the conduction band to an empty state of the valence band occurs. During this transitions a electron released a photon as a energy. This process is called "direct radiative recombination".[229–231] The quantum confinement effect helps in the $\pi-\pi^*$ transition of the sp^2 carbon core, which causes the direct radiative recombination of excitons. This direct radiative recombination process of excitons leads to multicolor fluorescence emission.[232–234] Increasing the number of conjugated π-domains through quantum confinement phenomena is directly responsible for redshift in the emission wavelength.[235–238]

3.2. Surface state defects

Surface engineering with functional groups of the carbonaceous core is very essential for red emission since the surface defects act as a vital factor for this phenomenon. The addition of different functional groups helps in the $n-\pi^*$ transition of the aromatic sp^2 carbon core to exhibit different energy states, resulting in the development of multiple surface defect states.[239,240] A border zone or spherical shell that is different from the carbon core region or body is referred to as a surface defect. The complex diversity is caused by the functional groups present on the surface or sp^2 and sp^3 hybrid carbon cores, leading to the defect state.[241–243] Different types of reasons cause different defect states, which leads to different colors of fluorescence in CNMs.[244] Surface oxidation is the primary cause, which can serve as a center for the attraction of excitons and

Table 1 Comparison summary of the synthesis processes, optical properties and applications of red emitting CNMs prepared from various kinds of carbon precursors

CNMs	Carbon precursor	Synthetic route	$\lambda_{exc}/\lambda_{emi}$ (nm)	Application	Reference
CDs	Carbon fibres	Acid oxidation	360/610	Bioimaging	Bao *et al.*[46]
CDs	Waste expanded polystyrene	Solvothermal	365/630	White light-emitting diodes	Song *et al.*[180]
CDs	Sugarcane bagasse	Carbonization	372/630	Ammonia sensing	Jiang *et al.*[181]
CDs	Spinach	Solvothermal	620/680	Bioimaging	Li *et al.*[182]
CDs	Lemon juice	Solvothermal	610/704	Bioimaging	Ding *et al.*[183]
CDs	Watermelon juice	Hydrothermal	808/925	Imaging and photothermal therapy	Li *et al.*[184]
CPDs	Taxus leaves	Solvothermal	420/673	One and two photon bioimaging	Liu *et al.*[185]
GQDs	Graphite rods	Electrochemical exfoliation	500/610	Cellular imaging	Tan *et al.*[45]
GQDs	Graphene oxide	Chemical degradation	420/630	Bioimaging	Ke *et al.*[47]
CDs	Coal pitch	Acid oxidation	365/630	—	Meng *et al.*[43]
CDs	Citric acid	Solvothermal	561/627	*In vitro* and *in vivo* bioimaging	Ding *et al.*[9]
CDs	*Bougainvillea* leaves	Microwave charring	420/678	Photodegradation of dye	Bhati *et al.*[186]
CDs	Cyanine dye	Solvothermal	720/820	Cancer imaging & therapy	Zheng *et al.*[187]
CDs	Resorcinol	Carbonization	490/600	—	Ghosh *et al.*[188]
GQDs	Graphene nano-particles	Mechanical exfoliation & oxidation	380/650	Optoelectronic device	Tetsuka *et al.*[171]
CDs	Glutathione	Microwave-mediated heating	420/683	Bioimaging	Pan *et al.*[189]
GQDs	Trinitro pyrene & boric acid	Ultra-sonication	380/617	—	Juang *et al.*[190]
CDs	Malic acid & neutral red	Hydrothermal	400/627	Per-manganate & pH sensing	Dan Chang *et al.*[191]
CQDs	*p*-Phenylene-diamine & urea	Solvothermal	286/614	—	Song *et al.*[192]
CNPs	Eucalyptus leaves	Hydrothermal	620/680	Theranostics	Damera *et al.*[193]
CDs	*p*-Phenylene-diamine & hydro-quinone	Solvothermal	455/590	Fe^{3+} & pyro-phosphate detection	Li *et al.*[87]
CDs	Citric acid & urea	Solvothermal	520/614	Light-emitting diodes	Qu *et al.*[194]
CDs	Diaminobenzene-sulfonic acid & amino-phenyl-boronic acid hydro-chloride	Hydrothermal	520/595	Dual-mode sensing of ClO^-/GSH	Li *et al.*[195]
CDs	Diamino-benzoic acid & catechol	Solvothermal	545/619	Detection of peroxynitrite in living cells	Fu *et al.*[196]
CDs	Citric acid & bi-naphthyl diamine	Solvothermal	540/603	Solid state luminescence & sensing of Fe^{3+} and F^-	Wang *et al.*[197]
CDs	4-Chloro-benzene-1,2-diamine & diluted HCl with deionized water	Sonication assisted solvothermal	540/650	Detection of tea polyphenols & cellular imaging	Cao *et al.*[198]
CDs	Neutral red & thiourea	Hydrothermal	520/637	Detection and reduction of Au^{3+}	Li *et al.*[199]
CNDs	Perilla leaves	Ultrasonication	420/670	Bacterial imaging	Zhao *et al.*[200]
CDs	Citric acid & *p*-phenylene-diamine	Hydrothermal	360/650	Mitochondria-targetable imaging and monitoring of biological processes in living cells	Jin *et al.*[201]
CDs	3-Dimethyl-amino-phenol	Solvothermal	540/632	Detecting and tracking lipid droplets in live cells	Jing *et al.*[202]

produce surface defect state fluorescence.[245,246] Surface oxidation occurs in the presence of significant functional groups, which causes the addition of oxygen atoms, loss of electrons, or removal of hydrogen.[247–250] The more oxidized surface helps to develop more defects frequently. The result is accompanied by the red shift in the emission wavelength of FCNMs.[251,252] Relaxation achieved *via* the radiation from the excitation state to the ground state is the reason for the surface defect state.[253,254] A variety of emission traps are produced by various functional groups, each with a unique energy level that results in a varied degree of defects. The ability of a functional group to deliver electrons, making them used on the surface of the

carbon core, would make it possible to modify the colour emission.[255–257] When a beam of photons of a specific wavelength is incident on the surface of the carbon materials, the photons whose energy fulfills the band gap energy will transit and assemble at the nearest surface defect traps. Then the photons return to the ground state to radiate tunable emission in the UV-visible region.[258–261] It is found that the functional groups support the π*–n and σ*–n transitions, following the molecular type of fluorescence and fixed spectral band changes with the excitation energy and size of the particles.[262–265] The functional group also causes structural deformation to the aromatic core, resulting in mid-gap states or energy traps, which contribute to π*–mid-gap–π transitions. Consequently, these transitions broaden the emission wavelength to a longer wavelength.[262,266–269]

4. Optical properties of red-emitting CNMs

The red-emitting CNMs are highly photobleaching resistant and have strong absorption and biodegradability in the red region or near infrared region. They have a very high penetration depth because of their high wavelength. The electronic and optical properties of luminescent CNMs can be studied using UV-visible and fluorescence spectroscopy followed by the determination of the steady-state and lifetime. The red emissive properties of FCNMs can be tuned by several factors including size, surface state, element doping, hydrogen bond, surface functionalization, energy transfer, crosslink-enhanced emission effect, and solvent effect.

4.1. Factors influencing the optical properties of red-emitting CNMs

4.1.1. Size controlling. The changes in the size of FCNMs influence the shifting of the fluorescence emission wavelength. By transmission electron microscopy (TEM) and scanning electron microscopy (SEM) of FCNMs, followed by size distribution plot analysis, we can easily predict the average core sizes, particle size distribution and morphology of FCNMs. Different size FCNMs have different bandgap widths, resulting in different fluorescence emission peaks. Increasing the size of FCNMs at the nanoscale results in narrowing of the energy band gap by the quantum confinement effect between the bonding and antibonding orbitals of FCNMs.[270–272] Therefore, illuminated photons are more likely to transition, which results in a shifting of the fluorescence emission peak to the red region or near infrared region. We can easily synthesize red FCNMs by controlling the size of the carbon nanomaterials by ultracentrifugation.[273,274] Huang *et al.* reported tunable size affected red-shifted fluorescence caused by increased intra-carbon dot Förster resonance energy transfer between the emitter homologs. They showed that the emission wavelength shifted from blue to red when increasing the size of the carbon dots from small to large.[275] Liu *et al.* described the size-dependent fluorescence of carbon dots. The team showed that increasing the size of the carbon dots resulted in red-shifted fluorescence. The TEM images showed that the particle size increased with red shifting. The red fluorescence is attributed to the rising density, which resulted in enhancing the HOMO energy level. Thus, the HOMO–LUMO energy gap decreased, causing the result, Fig. 2(a) and (b).[276] Zhan *et al.* showed the multicolour band gaped fluorescence of carbon dots as a result of variable size. The team observed that the fluorescence colour of carbon dot solution changes from blue to green to yellow to red with changes in the size of carbon nanomaterials.[277] Gao *et al.* described band gap-influenced multicolour emissive fluorescent graphene quantum dots with and without a coating of polyethyleneimine caused by the variation in the sizes of the graphene quantum dots. The individual graphene quantum dots showed yellow fluorescence and after embedding with two separate amounts of polyethyleneimine, blue and red fluorescence graphene quantum dots were prepared. The team showed that red and blue fluorescence was attributed to the size of nanomaterials, followed by the influence of the energy gap. Red fluorescence was caused by the large size induced narrow energy gap of the graphene quantum dots whereas the blue fluorescence was caused by the small size induced enlarged energy gap of the graphene quantum dots, Fig. 2(c) and (d).[278]

4.1.2. Surface functionalization and passivation. It has been found that surface functionalization and passivation techniques significantly alter the fluorescence characteristics of FCNMs.[279] Surface functionalization and passivation techniques are achieved by the recombination of electrons and holes, nearly associated with the sp^2 conjugated π-domain and surface chemistry.[280] An X-ray photoelectron, Fourier transform infrared, and RAMAN spectroscopy study will be done for the determination of the surface functional group present at the surface. The X-ray diffraction and zeta potential measurement will also reveal the nature of the carbon nanomaterials.[281] The addition of functional groups on the surface of FCNMs can generate abundant structural configurations and introduce new energy levels into their electronic structures.[282] As a result, the development of multiple defect state occurs, caused by surface oxidation. The bandgap energy is slowly reduced with increasing the degree of surface oxidation causing red-shifted emission.[283] The presence of electron-withdrawing or oxidizing groups increases the surface oxidation process, resulting in red emissive CNMs.[284] Li *et al.* showed that the surface modification of sulfinyl and carbonyl groups caused the generation of another discrete energy level, caused by the increasing degree of surface oxidation. The increasing surface oxidation reduced the energy gap of the outer layer, and as a result, the emission wavelength is shifted towards the red region, Fig. 3(b).[285] Ding *et al.* explained the surface state-controlled fluorescence mechanism of full-color light-emitting carbon dots. Excitation independent fluorescence from blue to red was observed as a result of surface defects. The surface defect state was generated by surface oxidation, followed by the narrowing of the energy gap. The band gap between the HOMO and LUMO strongly depends on the addition of several oxygen atoms. The increasing number of oxygen atoms on the surface results in surface oxidation, which generates more surface defects. The surface defect reduced the energy band gaps, result

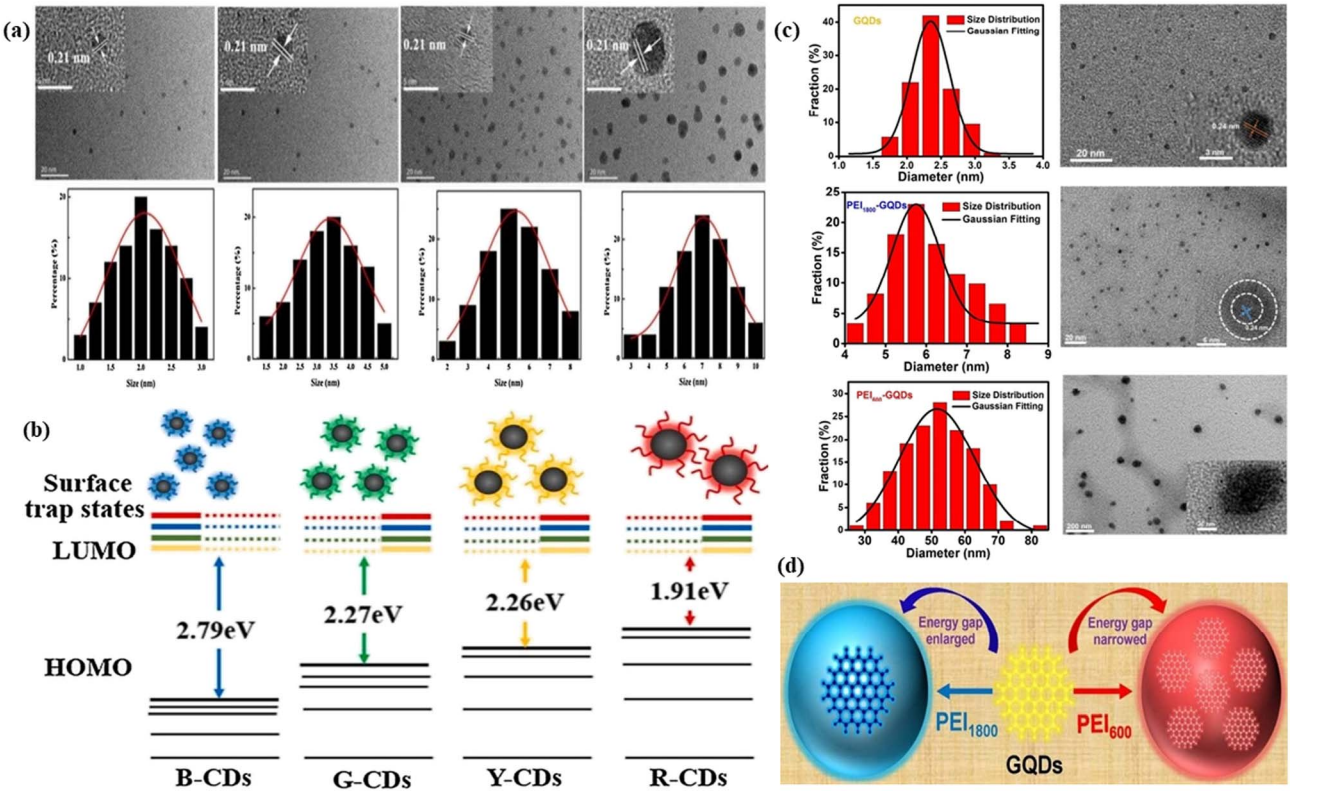

Fig. 2 Representation of the size effect on the red fluorescence of FCNMs: (a) TEM and HRTEM images of blue, green, yellow and red carbon dots respectively with size distribution plots; (b) tunable fluorescent carbon dots with their respective electronic energy level diagram, starting from blue, green, yellow and red respectively. Reprinted with permission from ref. 276, Copyright 2021, Elsevier; (c) TEM and HRTEM images of blue, green, yellow and red graphene quantum dots respectively with diameter distribution plots. Gaussian fitting curve is also plotted by the black line; (d) graphical representation of the transformation of yellow fluorescence graphene quantum dots to red fluorescence graphene quantum dots by narrowing the energy gap and yellow fluorescence graphene quantum dots to blue graphene quantum dots caused by enlarging the energy gap. Reprinted with permission from ref. 278, Copyright 2017, American Chemical Society.

in the red shifted emission, Fig. 3(a).[286] Gao *et al.* reported green to red tunable fluorescence through a solvent engineering method by using water. The water engineering caused an increase in the number of oxygen atoms followed by an increase in the oxidation degree. As a result, an increase in the number of carboxyl groups on the surface occurred, which leads to reduction of the energy gap and results in red-shifted fluorescence, Fig. 3(c).[287] Hola *et al.* described the red-shifted emission of carbon dots after introducing the carboxylate groups on the surface by mild hydrolysis of carbon dots.[288] Ding *et al.* reported that the graphitization degree, graphitic nitrogen content and oxygen-containing functional groups cause the shifting of fluorescence toward the red region *via* regulating the deamination and dehydration process, Fig. 3(d).[289]

4.1.3. Solvatochromism. Solvatochromism is a reversible process of changing absorption and emission wavelengths, which is initiated by the process of solvent. This phenomenon is commonly observed in FCNMs, when different solvents are added. Tunability is observed as a result of the maximum absorption shift. It occurs as a result of variations in the solvation energies of initial and excited states in different solvents.[290–292] This effect is associated with hydrogen bond capability, hydrogen bond acceptability and polarization on dipole moment. The energy difference between the ground and excited states as well as the orientation polarizability of solvents are both influenced by interactions between the solvent and carbon core.[293,294] For polar solvents, there is a hypsochromic shift with decrease in the polarity of the solvents and the shift is bathochromic with increase in the polarity of the solvent. The nonradiative charge recombination on the surface of FCNMs can be prevented by increasing the protonation capacity of the solvent and decreasing the viscosity of the FCNM solution, which will increase the ability to absorb and emit light in the red or near infrared region. Furthermore, increasing the alkynation, carbonization, and oxidation reactions using suitable solvents (containing the amino and carbonyl groups) lead to the amine and carboxylic acid functional groups containing ligands, which is also a good strategy to achieve red-emitting CNMs.[295–297] Gao *et al.* reported solvatochromic effect induced emission shift from green to red of carbon dots. The presence of a distinctive featured polymer chain with different functional groups and an effective π-conjugated carbonized core was the main reason for the shifting of the emission wavelength.[298] Lin *et al.* demonstrated the shifting of the emission wavelength from 520 nm to 630 nm, towards a long wavelength as an effect of the solvent polarity of bright carbon dots.[299] Alaş *et al.*

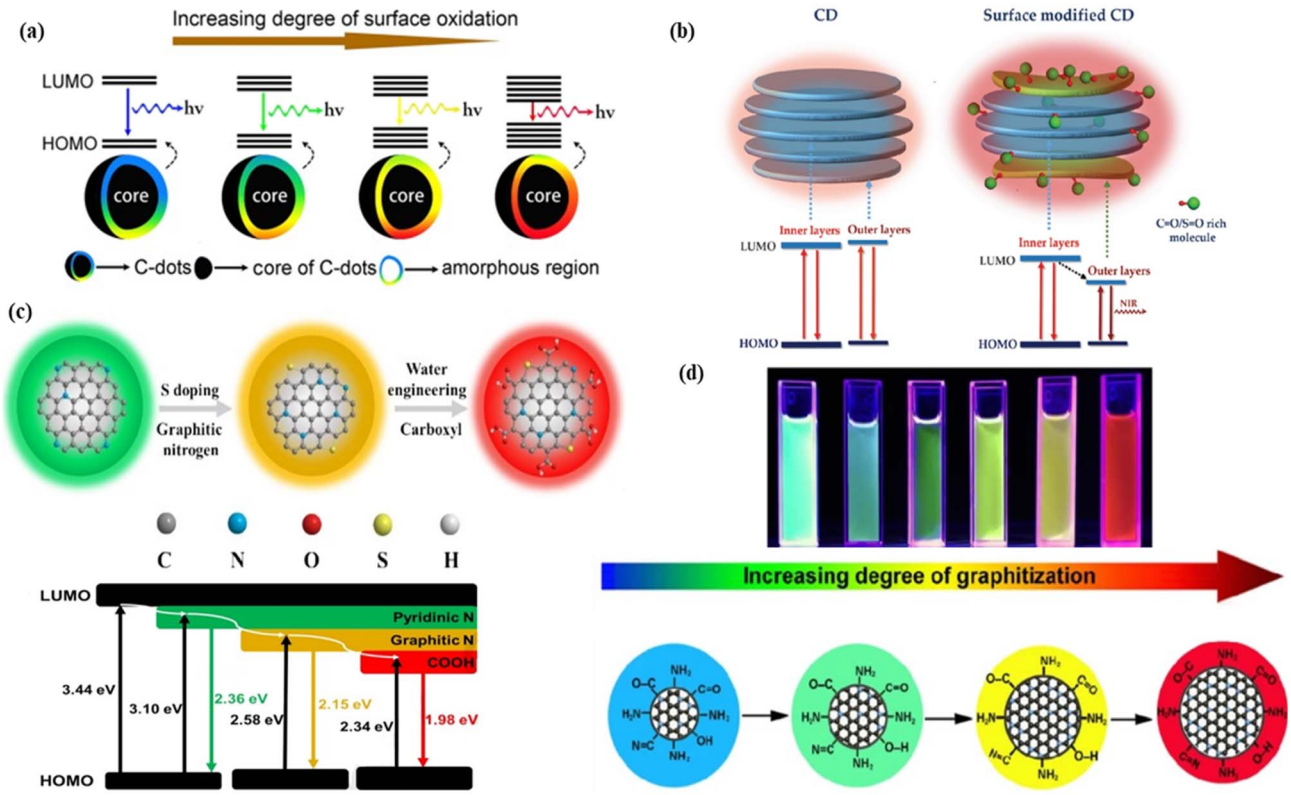

Fig. 3 Representation of the surface functionalization and passivation effect on the red fluorescence of CNMs: (a) graphical representation of the increasing degree of surface oxidation causing decrease in the energy gap, followed by red colour fluorescence. Reprinted with permission from ref. 286, Copyright 2016, American Chemical Society; (b) representation of the effect of sulfinyl and carbonyl groups on the red fluorescence of the carbon dots with the energy level diagram. Reprinted with permission from ref. 285, Copyright 2018, WILEY-VCH Verlag GmbH & Co. KGaA, Weinheim; (c) shifting of green fluorescence to red fluorescence by increasing the graphitic nitrogen content and the number of surface carboxyl functional groups with decreasing the energy gap between the HOMO and LUMO. Reprinted with permission from ref. 287, Copyright 2020, Elsevier (d) shifting of the fluorescence colour based on the graphitization degree, graphitization nitrogen, and oxygen containing functional group. Reprinted with permission from ref. 289, Copyright 2022, Springer.

showed the solvatochromic features of red fluorescence carbon dots by changing the solvent polarity. The carbon dots switched the green fluorescence colour to a red fluorescence colour when increasing the solvent polarity. The fluorescence image and emission spectra of carbon dots under different solvents including hexane, toluene, benzene, *ortho*-dichlorobenzene, dichloromethane, tetrahydrofuran, chloroform, acetone, methanol, ethanol, dimethylformamide, dimethyl sulfoxide, and water showed the shifting of emission to the red region, Fig. 4(a) and (d), as the polarity gradually increased. It was observed that the red shifted fluorescence was attributed to the polar nonprotic solvents dimethylformamide and dimethyl sulfoxide. The blue-shifted fluorescence was attributed to the aprotic solvent due to hydrogen bonding in-between carbon dots and hydrogen accepting solvents *via* hydrogen bond donating polar functional groups like –COOH, –OH, R–NH_2, and R–CO–NH–R of carbon dots. The dipole interaction between the carbon dots and solvents is also a reason for the blue shift. The team further looked into the fluorescence changes in more detail as a solvochromatic nanoprobe for the sensing of water molecule in tetrahydrofuran. It was noticed that the emission wavelength shifted to the red region as the percentage of water increased in tetrahydrofuran mixed carbon dot solution, Fig. 4(b) and (c).[300] Sato *et al.* reported solvent-dependent emission colours ranging from green to red using three different isomers of phenylenediamine, caused by the different polarities.[301] Wu *et al.* described blue and red dual colour fluorescent carbon dots depending on the changing polarity of the solvent. The hydrogen bonding interchange between the carbon dots and solvents was the main origin for the dual fluorescence.[302] Fan *et al.* synthesized red carbon dots which exhibited multicolour emission peaks from blue to red caused by the solvent polarity.[303]

4.1.4. Heteroatom doping. Heteroatom doping is the most useful technique for controlling the chemical formation and optical characteristics of FCNMs, since the creation of n-type or p-type carriers into the carbon core. The introduction of n-type or p-type carriers changes the electronic structure of FCNMs.[279,304] When the nonmetal atoms N, O, P, B, S, *etc.* are doped, the electron-rich atoms like N, O, P, S *etc.* raise the energy level of the HOMO while the electron-deficient atoms like B decrease the energy level of the LUMO. Doping of graphitic, pyridinic, hydrazine and amino N is a commonly used method to produce the redshifted fluorescence of CNMs

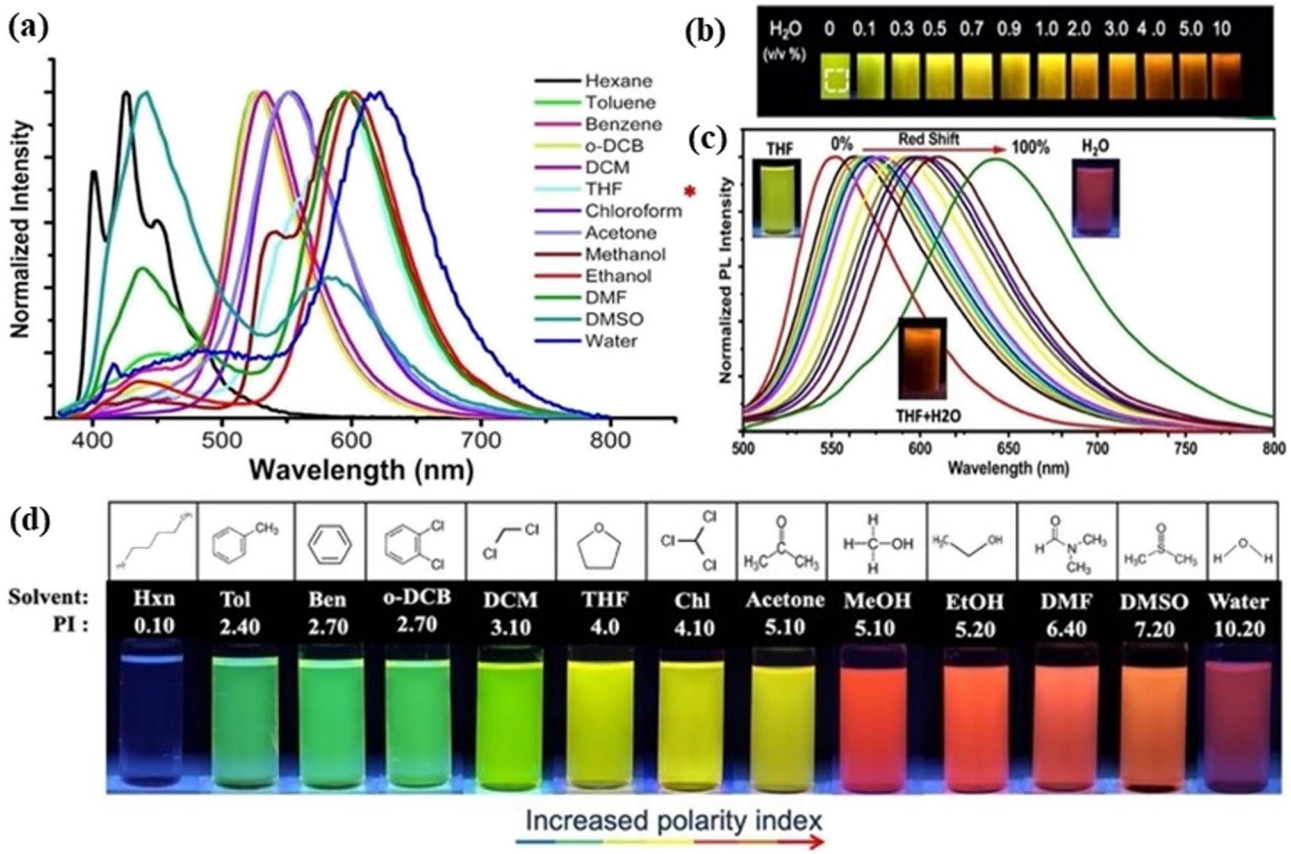

Fig. 4 Representation of the solvatochromism effect on red fluorescent carbon dots: (a) emission of the spectra of red carbon dots under different solvents including hexane, toluene, benzene, *ortho*-dichlorobenzene, di-chloromethane, tetrahydrofuran, chloroform, acetone, methanol, ethanol, dimethylformamide, dimethyl sulfoxide, and water. The asterisk sign reveals the highest intensity peak in chloroform; (b) image of carbon dot solution with the rising amount of water (0–10% vol) under UV light; (c) emission spectra showing the red shift of red carbon dot solution with tetrahydrofuran, tetrahydrofuran & water and only water; (d) fluorescence images of red carbon dots dissolved in different solvents under 365 nm UV light excitation. Reprinted with permission from ref. 300, Copyright 2021, American Chemical Society.

due to the process of doping and identical atomic size of carbon and nitrogen atoms. Other atoms including sulphur, selenium, boron, and fluorine are also used to get red shifting of the emission wavelength. The shifting of emission to the red region or near infrared region may have been caused by the addition of atomic contaminants like N, S, Se, B, F and La.[305–307] When heteroatoms are doped, the lattice of the FCNMs is disturbed, resulting in the appearance of new energy levels, which causes the shifting of the wavelength to the red or near infrared region. The doping of other heteroatoms will add chemical groups to the interface of the FCNMs, enlarging the conjugation domain and leading to red or near infrared emission.[308,309] Du *et al.* synthesized nitrogen-doped carbon dots *via* a microwave-assisted simple solvothermal method using *p*-phenylenediamine. The carbon dots showed red fluorescence over the excitation of ultraviolet light.[310] Li *et al.* showed an aggregation-induced red-shifted emission of phosphorous-doped carbon dots as a result of enhancing the electron density caused by the electron donation properties of a phosphorus atom and the π–π conjugation caused by the aggregation induced size enrichment.[311] Jiao *et al.* reported gadolinium-doped carbon dots with red emission under excitation.[312] Liu *et al.* demonstrated full wide half maximum narrow fluorescence and excitation dependent red emissive nitrogen-doped conjugated carbonized polymer dots for *in vitro* and *in vivo* biomedical applications.[313] Arul *et al.* studied the difference in fluorescence, catalytic activity, and various color *in vivo* and *in vitro* applications between heteroatom-doped and undoped carbon dots. The team used nitrogen, boron and sulphur as a doping atom for carbon dots.[314] Azami *et al.* showed the fluorescence behaviors of two different heteroatom doping carbon dots. They chose boron and phosphorus as a heteroatom in the structure of the carbon dots and investigated the consequences of the two heteroatoms on optical behavior. The phosphorous-doped carbon dots exhibited blue-shifted emission, caused by the effect of the carbon core followed by the increase of the energy gap between the HOMO and LUMO. The boron-doped carbon dots exhibited red-shifted emission caused by the surface functionalities like NO_3 and O–C=O bonds and fewer C–C bonds, Fig. 5(c).[315] It is generally observed that the increase in the nitrogen-containing graphitic carbon core caused a red shift in the emission of CNMs. Holá *et al.* reported that the increase of electron-donating nitrogen containing graphitic carbon cores produced a midgap state between the HOMO and LUMO,

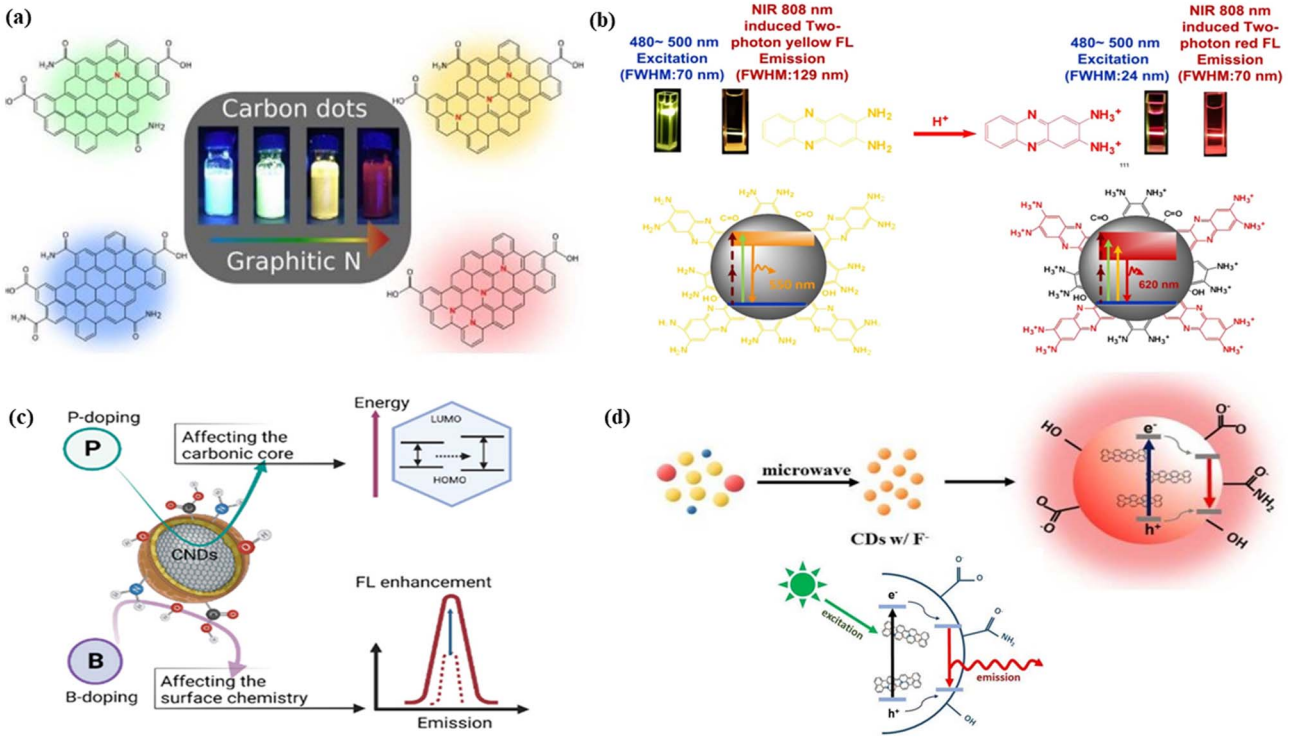

Fig. 5 The effect of heteroatoms on FCNMs for red fluorescence: (a) schematic illustration of red colour emission caused by graphitic nitrogen. Reprinted with permission from ref. 11, Copyright 2017, American Chemical Society; (b) the fluorescence mechanism of carbon dots (protonation of 2,3-diaminophe-nazine caused the red emission). Reprinted with permission from ref. 316, Copyright 2021, Springer Nature; (c) the effect of phosphorus and boron doping on the emission of carbon nanodots. Reprinted with permission from ref. 315, Copyright 2023, American Chemical Society; (d) red shifted fluorescence caused by the fluorine doping on carbon dots with the narrowing energy gap mechanism. Reprinted with permission from ref. 317, Copyright 2018, Elsevier.

leading to red-shifted emission, Fig. 5(a).[11] Zhang *et al.* described the amino protonation treatment of carbon dots with 2,3-diaminophe-nazine, minimizing the energy bandgap. As a result, the yellow color fluorescence solution of the carbon dots turned into red colour emissive carbon dots with narrow peak widths, Fig. 5(b).[316] Yang *et al.* showed red-shifted emission upon doping of electron-withdrawing fluorine atoms into carbon dots. The authors explained that the extension of the π-electron system due to the addition of the fluorine atom reduces the energy gap, which results in the red shifting, Fig. 5(d).[317]

4.1.5. Crosslink-enhanced emission effect. The crosslink-enhanced emission (CEE) effect is a brand-new discovered fluorescence phenomenon that is utilized to understand the intense emission trend at non-traditional emission centers. It is a crosslinking-induced effect to increase fluorescence.[318] Crosslinking can be achieved chemically or physically and can be introduced by covalent or non-covalent bonding. It affects the emission wavelength by controlling energy levels.[319] Inducing crosslinking shortened the distance between the functional groups resulting in the overlapping and coupling of electron clouds. Such interactions create sub-levels by splitting inherent energy levels.[320] Also introducing covalent bonds by crosslinking leads to the creation of new energy states. It helps to broaden the way of radiative and non-radiative transition by narrowing the energy distance of singlet and triplet states, thus increasing the red emission.[321,322] Chen *et al.* reported red carbon dots *via* a mechanism of chemical bonding that removes the defects, followed by the conservation of the efficient radiative process through surface states. It is acknowledged that the establishment of a stable chemical bonding not only closes the efficient radiative process through surface states but also prevents the nonradiative recombination of localized electron–hole pairs. Hence, the probability of long-wavelength red emission increased.[323] Wang *et al.* demonstrated crosslinking induced long wavelength red emissive carbon dots for multi-colour latent finger print scanning on complex background surfaces under UV-light irradiation.[324] Li *et al.* reported crosslinking-based increased photoluminescence behavior of carbonized polymer dots. The crosslinking causes a narrowing of the energy gap followed by red-shifted emission. The fluorescence mechanism followed that the crosslinking effect introduced the auxochrome or sub-fluorophores (electron-rich heteroatom groups), which are boosting the radiative transition and lowering the non-radiative transition. Hence, the quantum yield was increased and the fluorescence of the auxochrome of the carbon polymer dot was enhanced, Fig. 6(a). The negative impact caused by the crosslinking on the energy level and electron transition, together with the steady and compact environment of carbon polymer dots, significantly increased the electron cloud coupling and overlapping. It also causes the

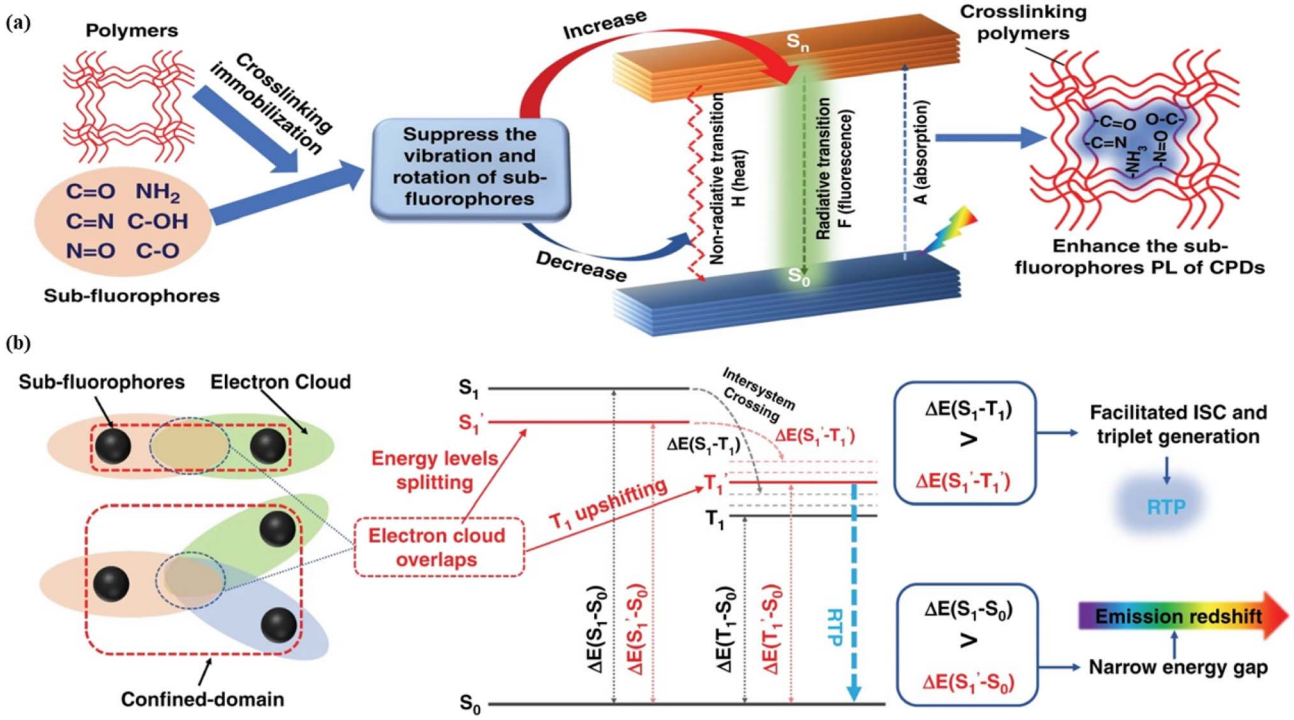

Fig. 6 Schematic representation of the crosslinking effect for the red emission: (a) the vibrational and rotational changes of the single bond and sub-fluorophores due to the crosslinking restriction, following the rising of radiative transition and minimizing the non-radiative transition; (b) the splitting of the confined domain into intrinsic energy levels to sublevels and raising the energy level of the triplet state lead to the overlapping and coupling of electron clouds followed by red shift of the emission [sub fluorophores-heteroatom holding double bonds like C=O, C=N, and N=O; single bonds-amino based groups, C–O; S_0 – ground singlet state; S_1 – excited singlet state; T_1 – triplet excited state; S_1 – first singlet excited state; T_1 – first triplet excited state; $\Delta E(S_1–S_0)$ – the energy gap between S_1 and S_0; $\Delta E(S'_1 - S_0)$ – the energy gap after the crosslinking between S_0 and S'_1; $\Delta E(S_1–T_1)$ – the energy gap between S_1 and T_1; $\Delta E(S'_1 - T'_1)$ – the energy gap after crosslinking between S'_1 and T'_1]. Reprinted with permission from ref. 325, Copyright 2022, Springer Nature.

splitting of energy levels and shifting of the emission wavelength to the red region, Fig. 6(b).[325]

4.1.6. Core–shell synergistic effect. The core–shell synergistic effect of CNMs is a combined effect due to the formation of a coordination bond of core–shell with an external additive. This effect is caused by the generation of a metal-carbonyl π-bond *via* the donation of a pair of electrons from a filled d-orbital of a metal ion into the vacant antibonding π-orbital of carbonyl groups present on the surface of the core–shell of CNMs.[326–328] The core–shell type carbon nanomaterials are a class of biphasic materials that have an inner core compact formation along with an outer shell made of different materials. When an additive molecule is added to FCNMs, a core–shell structure is achieved, which enhances optical properties synergistically. The addition of a new molecule to the surface of FCNMs introduces new energy levels, which activate the electronic transitions accordingly. The radiative and non-radiative transitions occur by narrowing the energy distance between the HOMU and LUMO, which enables the red shift of the emission.[329–331] Wu *et al.* reported the enhancement of the chemodynamic and photoluminescence behaviour of FeO_4 coordinated red carbon dots through the core–shell synergistic effect. The team showed that the embedding of an Fe-catalytic shell increases the emission wavelength by synergistic shielding and rigidifying effects. They explored carbon dots as a smart nanocatalytic medicine and efficient chemodynamic therapeutic agent.[332] Li *et al.* proposed that an enhancement in the fluorescent intensity of carbon dots was observed when silver doped silica nanomaterials interacted with the carbon dots by electrostatic interaction.[333] Lin *et al.* demonstrated a synergistic effect for increasing the fluorescence sensing effect of silica coated carbon dots. They applied the carbon dots for the detection of extracellular Cu^{2+} ions in the trat brain.[334]

5. Multifunctional applications

Because of the very high wavelength, penetration depth, biodegradability, absorption and photobleaching resistance properties of red emissive CNMs, they are used in biomedical applications, energy-related applications and many other valuable applications. The features and properties of carbon nanomaterials have been modified using a variety of surface and conjugation approaches.

5.1. Theranostics

It is a biomedical application process. The word "Theranostics" represents diagnosis and therapy at the nanoscale level or molecular level. This process involves simultaneously one

radiological medicine to detect and another radiological medicine to provide therapy treatment to both the primary and spreading tumours diagnostically.[335] Theranostic techniques connect specialized therapeutic material delivery with imaging using one of the non-invasive imaging tools based on various biophysical and biological principles.[336] Nanomaterials as a nanomedicine are used as theranostic agents to target the diseased affected area for diagnosis and then emerged for the delivery of therapy as needed. Therapy is none other than the delivery of nanomedicine for treatment to relieve or heal a disease or disorder. So, theranostic agents are used for the primary check-up of the problems and controlled release of nanomedicine with efficiency.[337,338] FCNMs emerged as theranostic agents due to their easy synthesis method, low cytotoxicity, easy surface functionalization, low photobleaching, and high penetration.[339]

5.1.1. Bioimaging. Bio-imaging using fluorescence probes ought to be low toxic and low photodamaging, and have high quantum yield and IR-region absorption and emission. Red emitting CNMs have been booming continuously in recent times as a contrast agent for bioimaging applications of living organisms due to their low cytotoxicity, minimal photodamage and deep tissue penetration depth.[340,341]

5.1.1.1. One photon fluorescence bioimaging. One-photon fluorescence bioimaging is a very crucial method in the field of bioimaging. When a laser beam of a particular wavelength is incident on a fluorophore, it excites the electrons present in the valence band, which go to a higher energy level. These excited electrons become unstable and stay for a certain time in the excited state. Later they return to the ground state by radiating some amount of energy in the form of photons following the emission of light. The whole process of excitation utilizes only one photon of light. Generally, one-photon fluorescence bioimaging uses near infrared or infrared light due to its longer penetration power.[342,343] Red emitting CNMs are very suitable for one photon fluorescence bioimaging as they have the absorption and emission wavelength in the red region.[344,345] Karakoçak *et al.* reported deep red fluorescent nitrogen-doped carbon dots *via* a microwave pyrolysis method. These red carbon dots are applied in the bioimaging of whole mouse and porcine ocular globes. Two different types of imaging including post-mortem and *ex vivo* imaging were performed after being embedded with the red carbon dots. The fluorescence image of red carbon dot injected porcine ocular globes was captured at 650 nm excitation wavelength and 700 nm emission wavelength at several time intervals, Fig. 7(c). The post-mortem of red carbon dot injected mice was performed under 550 nm and 660 nm excitation wavelengths, Fig. 7(b).[309] Su *et al.* developed antibacterial fluorescent curcumin carbon quantum dots that exhibit orange-red to infrared fluorescence. The curcumin

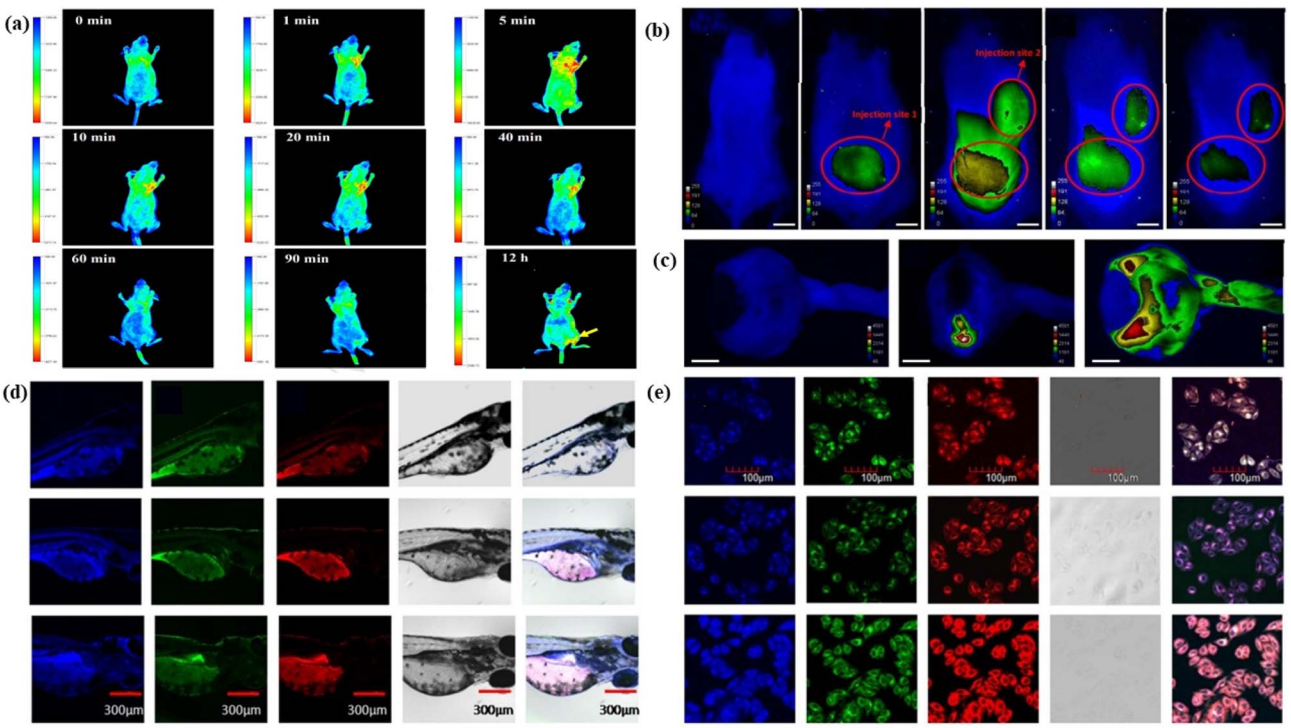

Fig. 7 Representation of red carbon dot assisted single photon fluorescence bioimaging: (a) *in vivo* fluorescence images of tumor-bearing mice after being injected with red carbon dots at different time intervals. Reprinted with permission from ref. 317, Copyright 2017, Elsevier; (b) post-mortem photograph of red carbon dot embedded mice with various concentrations of red carbon dots and a control one, under 550 nm excitation; (c) the red carbon dot injected porcine ocular globes under various conditions. Reprinted with permission from ref. 309, Copyright 2018, American Chemical Society; (d) confocal fluorescence images of three different types of red carbon dot embedded zebrafish larvae under various excitation; (e) confocal fluorescence images of three different types of red carbon dot embedded living HeLa cells under various excitation. Reprinted with permission from ref. 347, Copyright 2019, Springer.

carbon quantum dots were used in the bioimaging of bacteria cells.[346] Yang *et al.* synthesized fluorine-embedded red fluorescent carbon dots from urea and sodium fluoride mixed citric acid *via* a microwave synthesis method for both *vitro* and *in vivo* bioimaging. The developed red carbon dots were injected into a tumor-bearing mouse for *in vivo* bioimaging. An intense fluorescence image of the tumour-bearing mouse was observed at different time intervals, Fig. 7(a).[317] Huo *et al.* generated three red fluorescent carbon dots through a hydrothermal method using two isomers 1,5-diaminonaphthalene and 1,8-diaminonaphthalene with ethanol acetone and water. The generated carbon dots have strong red fluorescence and exhibited up conversion fluorescence nature. The red carbon dots are employed in multiple applications including *in vivo* and *in vitro* bioimaging, light activation and microarray detection. Confocal fluorescence images of three different types of red carbon dot embedded zebrafish larvae and HeLa cells under various excitation were captured for further diagnosis, Fig. 7(d) and (e).[347] Liu *et al.* demonstrated a red fluorescent carbon dot superoxide dismutase nano-enzyme for *in vivo* bioimaging of lung injury.[348] Wang *et al.* produced photostable red emissive carbon dots through a microwave heating and polyetherimide-assisted surface-modification method for cell fluorescence imaging.[88] Ge *et al.* synthesized bright red fluorescence carbon dots from polythiophene benzoic acid for both therapeutic and imaging applications.[349] Jiang *et al.* reported water soluble red emitting carbon dots using neutral red and levofloxacin as precursors *via* the *de novo* design and microwave assisted synthesis method for the visualization of RNA dynamics and exploring phase-separation behaviour in living cells.[350] Liu *et al.* developed a red carbon dot superoxide dismutase nanoenzyme, which was effectively used as a protector of living cells from oxidative damage *via* gathering the reactive oxygen species and reducing the levels of pro-inflammatory factors. The carbon dots were also explored for the bioimaging of tissues for the tracking of the heart, liver, spleen, lung, and kidney.[351]

5.1.1.2. Two-photon fluorescence bioimaging. Two-photon fluorescence bioimaging is one of the most emergent discoveries in modern technologies. This technology involves a non-invasive investigation of a biological object with three-dimensional, bright contrasted and sub-micrometer depth resolution images of the object. In this technique, fluorophores are excited by two photons following the simultaneous absorption of the two photons by the fluorophores. When the photon energy is at least half the band gap energy, the two-photon absorption occurs normally. The two-photon fluorescence bioimaging has higher resolution and specificity than one-photon fluorescence bioimaging because the laser beam does not excite the sample area outside the focus center as a result of the quadratic dependence of two-photon absorption on laser power, thereby protecting the nearby health tissue.[352] The visualization of the living tissue at a very long depth with a long observation time is possible by two-photon fluorescence bioimaging. Red emissive FCNMs can be developed by exciting fluorophores in red to near-infrared regions. Red-emissive two-photon CNMs are a great choice for utilization in theragnostics *i.e.*, therapeutic and diagnostic applications due to their biocompatible, less overlapping with biological autofluorescence, extremely low photobleaching, prolonged photostability, low photodamage to tissues, and depth penetration.[353] Pan *et al.* synthesized hydrophilic biocompatible near-infrared carbon dots, which showed two-photon fluorescence properties. These properties of red carbon dots are used for the deep-tissue two-photon bioimaging of living cells.[189] Zhang *et al.* produced pure red fluorescent carbon dots from formic acid mixed urea and citric acid blending. The as-developed carbon dots were applied in the *in vivo* tumour imaging and two-photon fluorescence imaging of the blood vessels in mouse ears. Green colour and red colour signals were detected from the mouse ear. Clear detection of the mouse ear vessel after the injection of the red carbon dots was observed in the two photon fluorescence images, Fig. 8(f).[354] Feng *et al.* created near-infrared graphene quantum dots that have two-photon fluorescence properties with an emission wavelength of 660 nm upon the excitation of 810 nm femtosecond pulses. The carbon dots were applied in two-photon nanoprobe identification and fluorescence imaging of ascorbic acid.[355] Kuo *et al.* generated nitrogen-embedded graphene quantum dots which possess excitation independent two-photon fluorescence emission varying from ultraviolet (UV) to infrared (IR). The materials were employed as a two-photon contrast agent in cellular imaging.[356] Liu *et al.* fabricated highly biocompatible and quantum-yielded carbon quantum dot materials by choosing a conjugated amine precursor. The materials were used in both one-photon and two-photon bio-imaging. The as-synthesized carbon dots showed a highly intense fluorescence colour with a sharp absorbance peak at 592 nm. The fluorescence emission peak was seen at 615 nm wavelength with a quantum yield of 80.77%, Fig. 8(a). The multiphoton fluorescence characteristics of the red carbon dots were examined with various tests. The excitation peaks of the carbon dots was apperaed at 1060 nm and 1100 nm respectively, after the laser irradiation. Both peaks confirmed that the red carbon dots could be used for near-infrared light-assisted multiphoton bioimaging, Fig. 8(b). The intensity of multiphoton emission spectra enhanced with gradually rising laser power, Fig. 8(e). The plotted graph of fluorescence intensity as a function of laser power was found to be linear, Fig. 8(d). A HeLa cell embedded with red carbon dots was examined under 1100 nm near-infrared laser excitation and the images of both confocal and two-photon imaging were captured, Fig. 8(c). It was observed that the two-photon excitation exhibited higher depth penetration as compared to the single photon. A zebrafish larva was coated with red carbon dots and the images under two-photon excitation were captured. A penetration depth of nearly about five hundred micrometres was attained. The whole outline of the larva was imagined in three-dimensional mode. In contrast only the near side larva was captured, in confocal single photon excitation images. So, it was easily concluded that the two photon imaging showed the clear, depth and three dimensional images of the object, Fig. 8(g).[357]

5.1.1.3. Photoacoustic bioimaging. Photoacoustic imaging is a hybrid imaging technique developed based on the principle of the photoacoustic effect . It is a non-invasive imaging technique

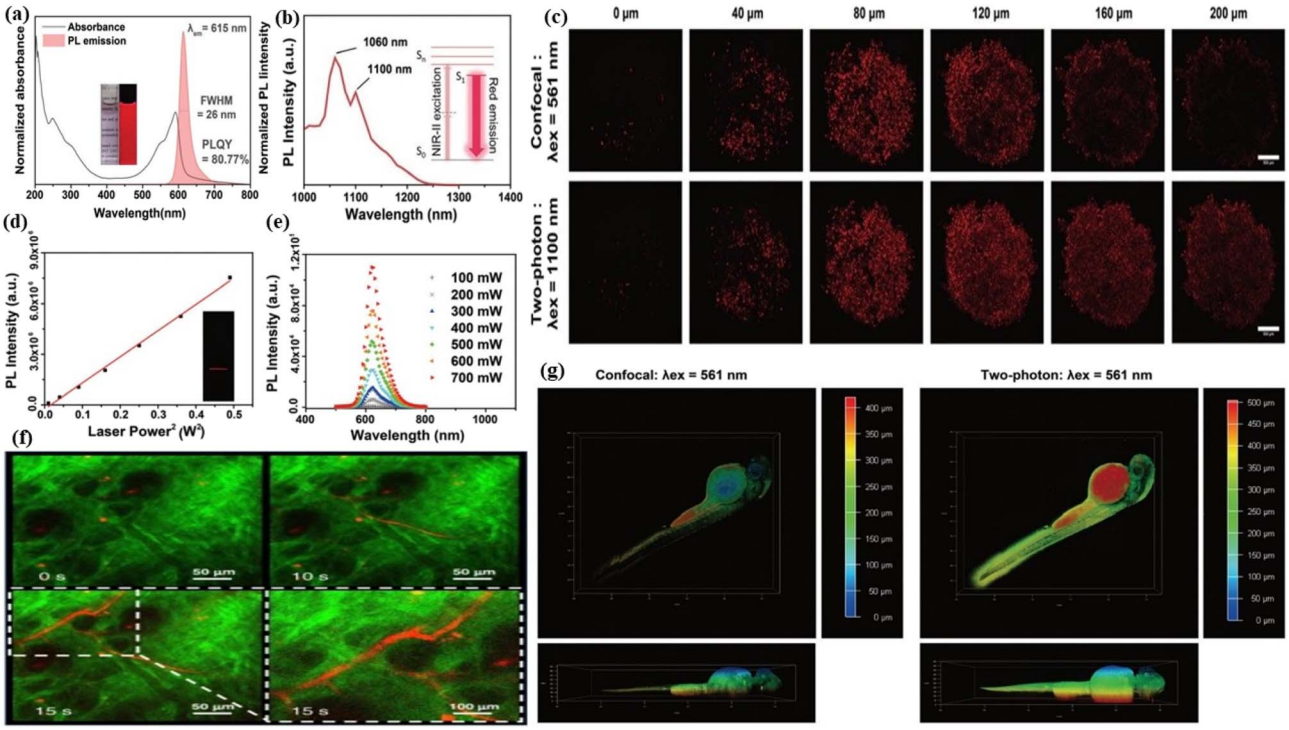

Fig. 8 Schematic representation of red carbon dot assisted two-photon bioimaging: (a) the fluorescence spectra and the UV-visible absorbance spectra of red carbon dots; (b) multiphoton excitation spectrum of the red carbon dots; (c) the two-photon and confocal imaging of HeLa cell tumour embedded with red carbon dots under different magnification; (d) the quadratic relationship between the multi-photon fluorescence intensity and excitation intensity after laser irradiation; (e) the multiphoton emission spectrum of red carbon dots under various excitation power. Reprinted with permission from ref. 357, Copyright 2019, Royal Society of Chemistry; (f) two photon fluorescence images of the blood vessel of a mouse ear before and after injection of the red carbon dots. The dashed line shows the partial enlargement. Reprinted with permission from ref. 354, Copyright 2022, Springer Nature; (g) the analysis of confocal and two-photon imaging of red carbon dot embedded zebrafish larvae. Reprinted with permission from ref. 357, Copyright 2019, Royal Society of Chemistry.

consisting of both optical and ultrasound imaging techniques called photoacoustic imaging.[358–360] The photoacoustic effect is a phenomenon whereby light energy absorbers in tissues are treated with a non-ionizing pulsed laser beam in the near-infrared range for a nanosecond time-range. Some of the light energy of the laser beam is transformed to heat that prompts a quick expansion of thermoelastic materials followed by the generation of an ultrasonic wave. The produced waves are detected by an ultrasonic sensor presented on the surface of the object being imaged. It is time-saving, non-intrusive and safe. Hence it is suitable for kids. Like fluorescence imaging, photoacoustic imaging also has sensitive light absorption and can produce high-contrast images (with a few centimeters of depth) in the areas of biological tissues.[361–364] Ge *et al.* produced broad absorption red fluorescent carbon dots from polythiophene phenyl propionic acid. The red carbon dots showed photoacoustic phenomena and high photothermal conversion efficiency characteristics when treated with a laser. The characteristics of red carbon dots were utilized in photoacoustic imaging and cancer therapy.[365] Parvin *et al.* reported phosphorus and nitrogen co-doped red emissive higher quantum yielded carbon dots from citric acid *via* a simple hydrothermal treatment for utilization in the photoacoustic imaging of living tissue. The excitation-dependent fluorescent emission of the as-synthesized red carbon dots was observed in this case. Fluorescence images were captured under various excitation wavelengths of 455 nm, 523 nm, 595 nm and 605 nm, Fig. 9(a). The response photoacoustic intensity spectrum of the red carbon dots was recorded under various concentrations of carbon quantum dots and it was seen that the photoacoustic signal increased with concentration, Fig. 9(b). Real-time photoacoustic imaging was performed after injecting the red carbon dots into cancer-affected mice. A controlled experiment was also performed along with the first one. The red carbon dots were spread all over the body of mice as well as the affected tumour area. Their photoacoustic images were captured. After six hours the red carbon dots were concentrated in the tumour-affected area, Fig. 9(c). After one day other organs including the liver, heart, lung, kidneys, spleen and tumour were also recorded. The liver and tumour of the mice exhibited maximum fluorescence whereas the others showed very low fluorescence, Fig. 9(d). The fluorescence of the tumour area increased very fast after the injection due to the fast settling down in the area. For better diagnosis various deposition stages were recorded at various time intervals, Fig. 9(e).[366] Jia *et al.* developed gold nanorod and silica-coated carbon dots with excitation wavelengths ranging from 680–980, which were utilized in both photoacoustic imaging and photothermal therapy.[367] Bao *et al.* developed

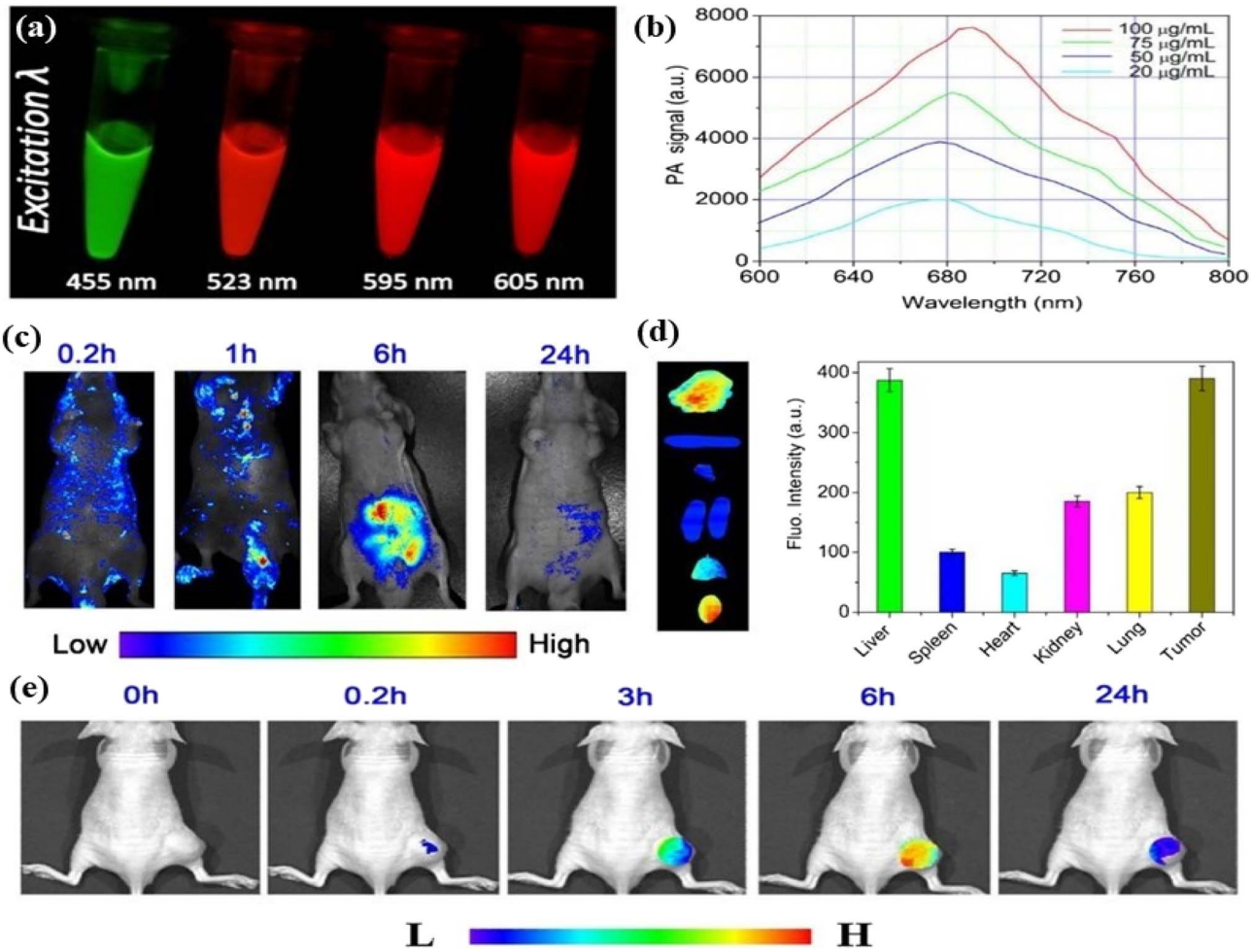

Fig. 9 Photoacoustic imaging of red carbon dots: (a) excitation dependent fluorescence of carbon dots solution; (b) photoacoustic response of red carbon dots with various concentrations; (c) photoacoustic photograph of the red carbon dots injected mice at various time intervals; (d) experimental *in vivo* photographs of the red carbon dots injected liver, spleen, heart, kidney, lung, and tumour of cancer affected mice; (e) photoacoustic photographs of tumour in mice after being injected with red carbon dots under excitation wavelength at various time intervals. Reprinted with permission from ref. 366, Copyright 2017, Springer.

photostable near-infrared emissive sulphur and nitrogen-embedded carbon dots that showed good theranostic potential for use in photoacoustic imaging.[368] Xu *et al.* demonstrated cobalt oxyhydroxide-coated red fluorescent carbon dots for the photoacoustic and fluorescence probe for the sensitive and selective identification of ascorbic acid. This result influenced researchers to develop oxyhydroxide-based photoacoustic probes.[369]

5.1.2. Therapy. Therapy is intended to both treat and prevent a particular disease. This process helps to heal or restore the health of a living being. Medicines are used to specifically target the proteins and genes that support the growth and survival of cancer cells to control and prevent growth.

5.1.2.1. Photothermal therapy. As the name suggests "Photothermal Therapy" involves "photo" which means light and "thermal" which means heat. This process is one of the types of therapeutic models for cancer treatment through a photothermal agent that transformed the nonradiative absorbed light to heat energy in the location area. It has reduced side effects unlike traditional chemotherapy.[370,371] Permatasari *et al.* reported red-shifted pyrrolic nitrogen-rich carbon dots *via* microwave-assisted hydrothermal synthesis. The red carbon dots showed photothermal effects with high near-infrared photothermal efficiency and high fluorescence characteristics. These characteristics are used in photothermal cancer therapy.[372] Scialabba *et al.* prepared red fluorescent biotin-coated carbon dots as nano-heaters to convert near-infrared light into heat for the photothermal therapy of the cancer cell.[373] Lan *et al.* developed sulphur and selenium-embedded carbon dots with excitation independent near-infrared emission. The as-developed carbon dots possess high photothermal conversion efficiency that is employed in the photothermal therapy of cancer cells with the assistance of fluorescence imaging. The team injected the red carbon dots into cancer-affected mice to investigate the photothermal effect of the red carbon dots. The tumour of the mice illuminated strong fluorescence under 560 nm laser excitation, Fig. 10(a) right. A

controlled experiment was also performed to observe the difference after being injected with the red carbon dots and excited under normal light, Fig. 10(a) left. A full-body inferred thermal image was captured after being injected with red carbon dots and saline in the cancer-affected mice. The red carbon dot injected mice showed a large temperature increase under laser illumination in comparison with saline, which caused a low-temperature increase, Fig. 10(b). The irradiated area temperature as a function of irradiation time was noted. The surface temperature of the tumour of red carbon dots injected mice increased very fast to 52 °C while the surface temperature of the saline-injected mice increased by only 5–6 °C, six minutes after the laser irradiation, Fig. 10(c). The maturation of tumour volume as a function of post-day treatment was recorded for the red carbon dots with light, only red carbon dots, only light and only saline, Fig. 10(d). It was observed that the cancer-affected HeLa cells glowed under the excitation of 488 nm and 880 nm wavelengths, Fig. 10(e) and (f). Cell death was seen after producing various blebs, caused by the photothermal effect of the red carbon dots after excitation, Fig. 10(g) and (h).[374] Weng *et al.* produced a nano-vehicle with a red emissive carbon dot induced indocyanine green and ultrathin layered double hydroxide mixture. The mixed materials exhibit great fluorescence, photoacoustic, two-photon bioimaging and effective photothermal properties. These properties are employed in multifunctional applications including photothermal therapy.[375] Hou *et al.* proposed gold-doped carbon dot nanoflowers with strong red emission under 750 nm laser irritation for novel photothermal cancer therapy.[376]

5.1.2.2. Photodynamic therapy. Photodynamic therapy, a two-stage procedure, uses a photosensitizer medicine to kill malignant and precancerous cells after light activation of the medicine. Until light activation, the photosensitizer medicine is non-toxic. The photosensitizer turns poisonous to the malignant and the precancerous cell after being activated by light energy. A certain wavelength of light radiation, typically from a laser source, activates the photosensitizer medicine.[377–379] Photodynamic therapy has the potential to activate the immune system, offering the human body an additional tool to assist the elimination of malignant and precancerous cells. Several diseases, including skin malignancies, brain malignancies, lung malignancies, bile duct malignancies, bladder malignancies, pancreatic malignancies, oesophagus malignancies, head-neck malignancies, and macular degeneration are caused by aging, skin acne, and skin disease psoriasis. These diseases are treated with photodynamic therapy using various types of photosensitizer. The bacterial and fungal infectional disorders are also treated with photodynamic therapy using photosensitizer.[380–383] Zhao *et al.* proposed biocompatible nitrogen and phosphorus co-embedded red fluorescent carbon dots that empower the ability of $^1O_2$ production and utilized

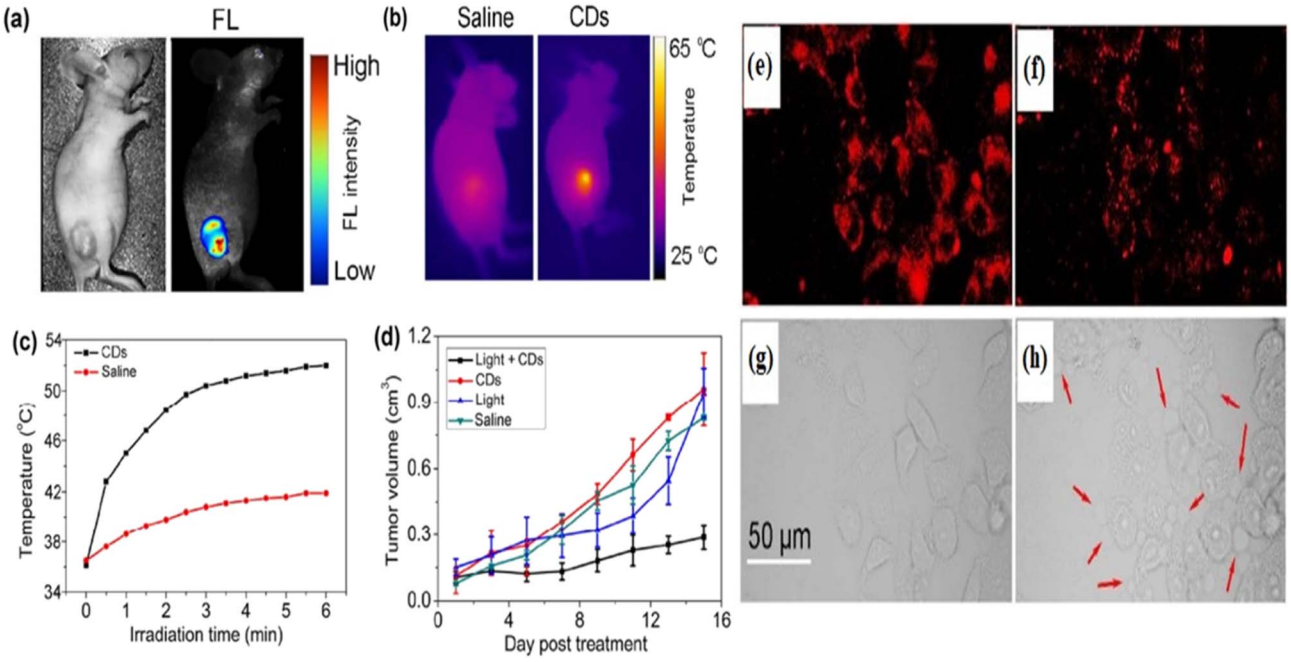

Fig. 10 Representation of the red carbon dot assisted photothermal therapy: (a) white light image (left) and fluorescence image (right) of red carbon dot injected mice; (b) infrared thermal images of tumour bearing mice after injection of saline and red carbon dots, respectively; (c) temperature changes as a function of time of the tumour bearing mice under 880 nm laser irradiation; (d) changes in the tumour volumes as a function of post-day treatment with the red carbon dots; (e) confocal fluorescent microscopy images of a cancer affected cell after the injection of red carbon dots under 488 nm excitation; (f) confocal fluorescence microscopy images of the cancer affected cell after the injection of red carbon dots under 880 nm excitation; (g) transmission images of the cancer affected cell after the injection of red carbon dots before laser illumination; (h) transmission images of the cancer affected cell after the injection of red carbon dots three minutes after the laser illumination. Reprinted with permission from ref. 374, Copyright 2017, Springer.

them as a photosensitizer in the photodynamic therapy of lung cancer cells.[384] Yi *et al.* developed nitrogen embedded two photon carbon dots with red emission that offers the generation of reactive singlet oxygen (ROS). The produce ROS helps in the photodynamic treatment of the nucleus to identify dynamic changes.[385] Xu *et al.* fabricated photostable, biocompatible and singlet oxygen yielded red fluorescent carbon dots as a photodynamic therapeutic agent for lung cancer cells and apoptotic cells.[386] Liu *et al.* reported photostable antibacterial red emissive carbon dots for photodynamic therapy of Gram-negative *Acinetobacter baumannii*. The as-synthesized red carbon dots enter into the bacteria cell very rapidly and kill it successfully. The red carbon dots produced reactive oxygen species under the light illumination of 590 nm. The reactive oxygen quickens the killing of multi-drug resistance *Acinetobacter baumannii* bacteria, Fig. 11(a).[387] Ge *et al.* demonstrated the photodynamic therapy of red fluorescent graphene quantum dots in a breast cancer cell transplanted female mice model *via* a multistep photosensitization process followed by the generation of singlet oxygen. They synthesized the graphene quantum dots through a single step hydrothermal method of polythiophene derivatives. As a photodynamic agent, other sensitizers took part in the production of $^1O_2$ *via* electronic transition from excited triplet state (T_1) to ground state (G), Fig. 11(b) left. The energy gap between the first singlet excited state (S_1) and the first triplet excited state (T_1) of graphene quantum dots is larger than the formation energy of $^1O_2$. The energy gap between the first triplet excited state (T_1) and the ground state (G) of the graphene quantum dots is also larger than the formation energy of $^1O_2$. As a result, the production of $^1O_2$ followed two paths. First, the electronic transition from the first triplet excited state (T_1) and second, the electronic transition from first singlet excited state (S_1) to ground state (G) *via* a intersytem crossing. Consequently, it was possible to attain a total $^1O_2$ quantum yield greater than 1, Fig. 11(b) right. For photodynamic therapy, a breast cancer affected mice model was examined under different treatments on the first, ninth, seventeenth and twenty fifth days. In the case of photothermal therapy, the tumour initially turned black and decomposed, which reduced the size of the tumour. After nine days, it started to decompose and then uprooted after seventeen days. One week later, it left dark marks, where they originally were before peeling off. After fifty days of the photodynamic therapy, no sign of tumour progression was seen. Tumor progression was compared using different types of photodyanamic therapy (PDT: GQDs+light irradiation; C1: GQDs only; C2: light irradiation only), Fig. 11(d).[388] Zhao *et al.* developed nitrogen and sulfur-embedded red emissive carbon dots to penetrate tumor cells as an effective photosensitizer for image-guided photodynamic therapy.[389] Zheng *et al.* synthesized red carbon dot doped carbon nitride for increasing the water-splitting ability to produce reactive oxygen. Water splitting by the carbon nitride helps in the photodynamic therapy of tumor cells. When the carbon dot doped carbon nitride nanoparticles were applied, they entered the cancer tissues and had an impact

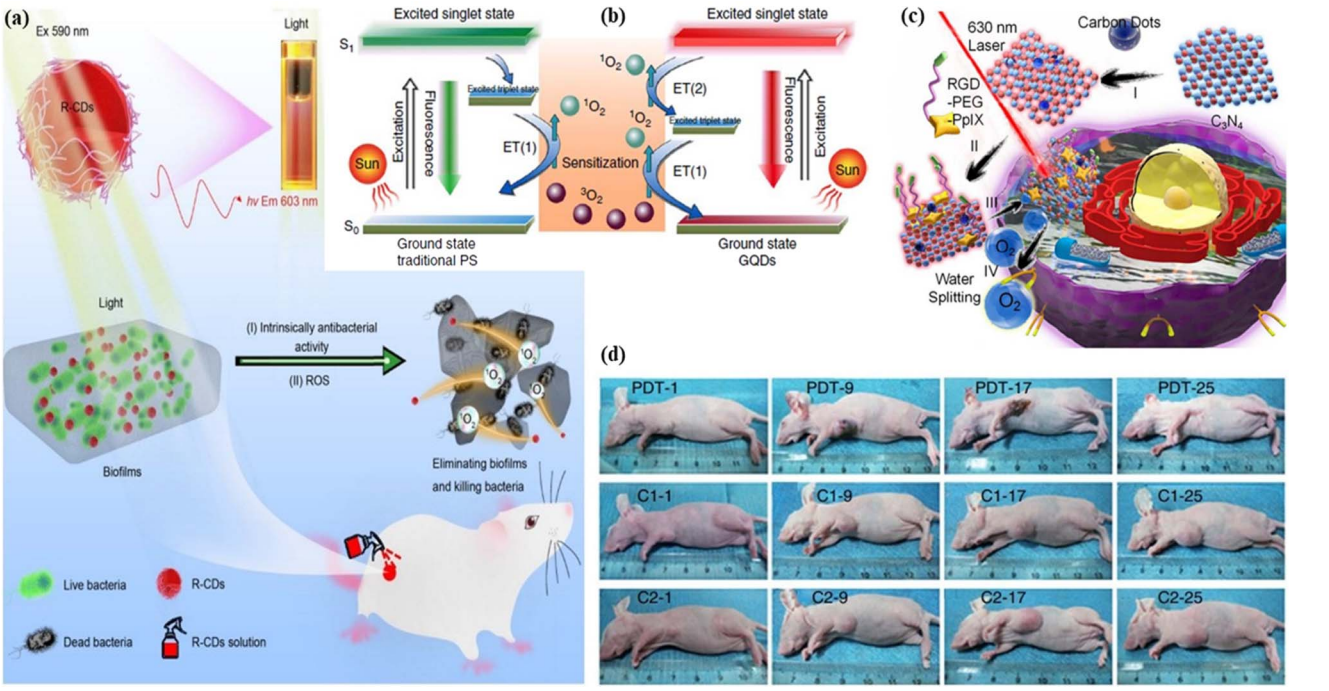

Fig. 11 Representation of red carbon dot assisted photodynamic therapy: (a) red carbon dots for the diagnosis of multi-drug resistance *Acinetobacter baumannii* bacteria using photoexcitation. Reprinted with permission from ref. 387, Copyright 2022, Springer; (b) mechanism of the photodynamic treatment agent red graphene quantum dots under light sensitization. Reprinted with permission from ref. 388, Copyright 2014, Springer Nature; (c) graphical representation of the light-assisted water splitting photodynamic therapy with several mechanisms. Reprinted with permission from ref. 390, Copyright 2016, American Chemical Society; (d) *in vivo* imaging of the mice under different treatments on the first, ninth, seventeenth and twenty-fifth days. Reprinted with permission from ref. 388, Copyright 2014, Springer Nature.

on the permeability and retention of those tissues. A laser with a 630 nm wavelength was used in the hybrid carbon nanosystem to split water and produce oxygen. Singlet oxygen was produced from this oxygen for cancer diagnosis under laser irradiation and this produced reactive oxygen species helps to treat the cancer cells, Fig. 11(c).[390] Yang *et al.* fabricated red fluorescent carbon dots using citric acid and tea polyphenol as precursors *via* a formamide assisted solvothermal method. The team explored the excellent antitumour properties of the carbon dots as a photosensitizer *via* the photodynamic therapy of a breast cancer cell affected mouse model.[391] Cai *et al.* reported red carbon dots from metformin and methylene blue for the development of light controlled nitric oxide generation and the liposome targeted photodynamic therapy of cancer cells efficiently.[392]

5.1.2.3. Synergistic therapy. Synergistic therapy, an efficient new way of anticancer therapy, involves a higher collective effect of two or more medications which is larger than the total effect of the individual medicine. Basically, the new synergistic therapy is developed by combining the beneficial properties of photothermal and photodynamic therapy.[393,394] Red FCNMs can be successfully employed to produce synergetic therapy treatment that contains both the photothermal and photodynamic effects.[25] Bai *et al.* fabricated sulphur and nitrogen co-doped two-photon emissive red carbon dots for fluorescence imaging-assisted synergistic photodynamic therapy and photothermal therapy of tumour cells. The as-synthesized carbon dots have a 27% efficiency rate of singlet oxygen production and 34.4% photothermal conversion efficiency. The doping of sulphur and nitrogen helped to increase the synergistic therapy in this model, Fig. 12(c).[395] Shinde *et al.* reported biocompatible and stable lipid-coated red fluorescent carbon dots derived from *Clitoria ternatea* leaves for red fluorescence imaging of zebrafish embryos and synergistic therapy of breast cancer cells.[396] Jia *et al.* synthesized hydrophilic red fluorescent carbon dots as a photo-synergistic agent from *Hypocrella bambusae* for bimodal fluorescence imaging-guided synergistic photodynamic and photothermal therapy in cancer cells. It was observed that these as-synthesized carbon dots could effectively produce $^1O_2$ species and hyperthermia for bimodal synergistic photothermal and photodynamic therapy of cancer, in contrast to single photodynamic therapy, Fig. 12(b).[397] Sun *et al.* demonstrated photosensitizer chlorin e6 doped amino-rich red fluorescent carbon dots for photoacoustic image guided and near infrared laser excited synergistic therapy of cancer cells.[398] Song *et al.* developed red light-emitting carbon dots and latterly

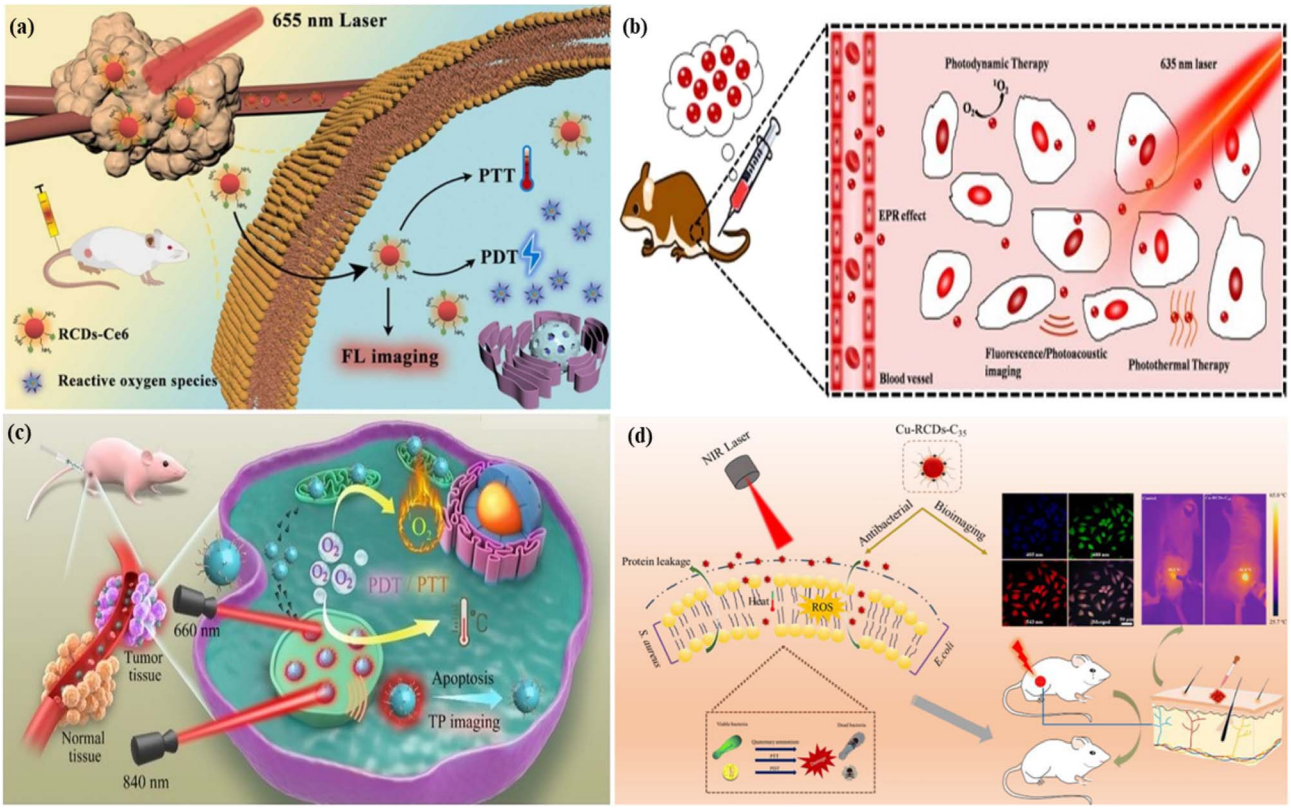

Fig. 12 Representation of the synergistic therapy: (a) chlorin-e6 doped red fluorescent carbon dot-based hybrid nanoplatform for synergistic photodynamic and photothermal therapy. Reprinted with permission from ref. 399, Copyright 2023, Elsevier; (b) red carbon dots for the synergistic bimodal photodynamic and photothermal therapy of cancer. Reprinted with permission from ref. 397, Copyright 2018, Elsevier; (c) sulphur and nitrogen co-doped two-photon emissive red carbon dots for the synergistic therapy of the tumour cell. Reprinted with permission from ref. 395, Copyright 2021, American Chemical Society; (d) copper doped and cocamidopropyl betaine conjugated red carbon dots for the bioimaging assisted synergistic therapy of cancer affected cells. Reprinted with permission from ref. 400, Copyright 2021, Elsevier.

photosensitizer chlorin-e6 embedded with the red carbon dots through an amide reaction. As a result, they reduced phototoxicity and photodynamic and photothermal therapy could be achieved under a single laser excitation. These chlorin-e6 embedded carbon dots are utilized in fluorescence image-guided tumour treatment and synergistic therapy for tumour cells, Fig. 12(a).[399] Chu *et al.* produced copper-doped antibacterial red carbon dots for a fluorescence imaging-assisted triple synergistic disinfection effect induced by a near-infrared light source. The carbon dots were embedded with cocamidopropyl betaine, a quaternary ammonium complex for the synergistic antibacterial effect with the help of reactive oxygen species at a low concentration and temperature under 808 nm laser irradiation, Fig. 12(d).[400]

5.1.2.4. Sonodynamic therapy. The name suggests that it involves sound. Sonodynamic therapy is an ultrasound-assisted therapeutic approach. The activation process using non-toxic sonosensitizers in the presence of molecular oxygen produced an excessive amount of reactive oxygen to destroy cancer-affected cells.[401,402] It is similar to photodynamic therapy but employs ultrasound stimulation as the stimulus rather than light. This therapy penetrates affected tissues more deeply, in contrast to photodynamic therapy.[403,404] The combination of photodynamic therapy and sonodynamic therapy is known as sono-photodynamic therapy and often involves both illuminated photon and ultrasound wave sensitizers. As a result, these types of therapy exhibit deeper penetrating power.[405,406] Ju *et al.* reported deep red emissive hydrophilic graphene quantum dots as a sensitizer for generating reactive oxygen molecules by ultrasound activation. The ultrasonic-assisted reactive oxygen stimulation potential of red graphene quantum dots was examined by using 2,7-dichlorodihydrofluorescein diacetate. It was observed that compared to other sensitizers, the red graphene quantum dots help in the high-level generation of reactive oxygen species which helps in cancer therapy, Fig. 13(d). After six hours, superior production of reactive oxygen species was observed with ultrasonic assistance (green colour), Fig. 13(b). In contrast, the production of reactive oxygen species was not seen in the case of ultrasonic assistance, Fig. 13(b). The damage of lysosomes and their removal through the production of reactive oxygen species were seen with ultrasonic treatment. The lysosome removal was compared with and without ultrasonic assistance, Fig. 13(c).[407] Geng *et al.* demonstrated near infrared phosphorescent carbon dots as a sonosensitizer with a narrow band gap and long-life triplet excited state. These properties help in sonodynamic tumour therapy under low-intensity ultrasound sound activation. The carbon dots produced ingenious p-type and n-type junctions and a narrow band to increase the charge separation dynamics with near-infrared absorption and emission. This specific electron withdrawing and electron donating electronic state enriches the low energy carrier excitation and highly efficient charge separation of the carbon dots. The p-type and n-type junctions enable effective high $^1O_2$ generation under ultrasonic irradiation *via* a three-step mechanism. In the first step, highly efficient p–n junction-mediated inhibition of e^-–h^+ pair recombination took place, followed by sustained triplet state-mediated $^1O_2$ generation in the second step. The third step involved employing

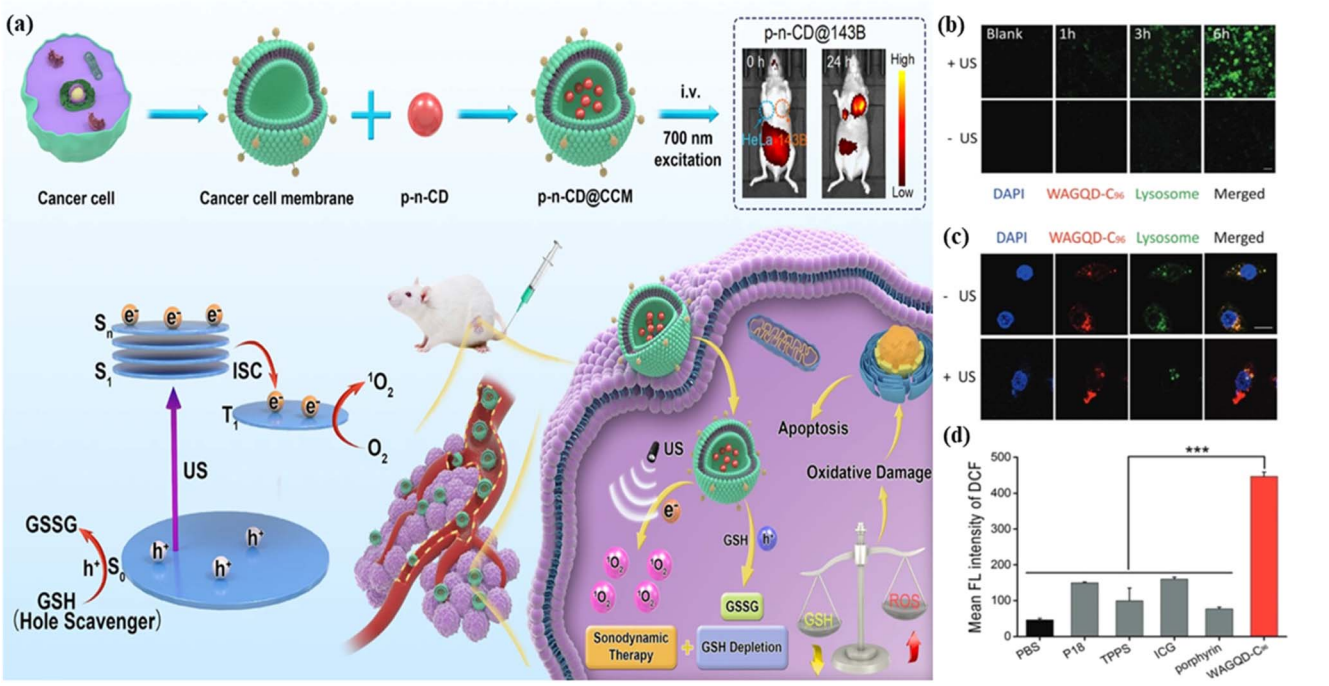

Fig. 13 (a) The representation of mechanism and design of sonodynamic therapy for cancer cells using the infrared-excited red carbon dots; (b) the comparison of reactive oxygen species generation using red graphene quantum dots with (top) and without (bottom) ultrasonic assistance; (c) the comparison of lysosome removal with (top) and without (bottom) ultrasonic assistance (d) the comparison bar digram of reactive oxygen species generation using red graphene quantum dots sensitizer vs other sensitizers.

overemphasized glutathione as a hole sacrificial agent to reduce glutathione levels which was oxidized to glutathione disulfide. The developed carbon dot-based near-infrared bioimaging assisted sonodynamic therapy targeted cancer-affected cells, Fig. 13(a).[408] Wei *et al.* proposed titanium dioxide and silica-assisted carbon dots exhibited outstanding photothermal effects and photodynamic properties for sonodynamic therapy. These carbon dots played a key role in the diagnosis of carcinogenic tumor effectively.[409]

5.1.3. Drug delivery. Drug delivery is an important technique or approach to accomplish a medicine's therapeutic impact on a human or animal. The effectiveness of a medicine is significantly impacted by the choice of the drug delivery technique.[410,411] Nanomaterial-based drug delivery systems show the most potential since they can get around issues including instability, tailored delivery, biotransformation, and poor bioavailability.[412] The drug delivery model also improved therapeutic efficiency and the solubility of medicines, prolonged the tumor retention time and minimized the side effects.[413] Su *et al.* developed a red fluorescent carbon dot-modified anticancer medicine delivery system for the removal of cancer effectively. These as-synthesized red carbon dots can penetrate cancer stem cells as well as nuclei of cancer cells.[414] Ren *et al.* synthesized red emissive carbon dots as a nanocarrier from thiophene phenyl propionic acid polymers for the delivery of coptisine in the cancer cell. The *in vitro* drug delivery of coptisine after being loaded into the red carbon dots was examined in a phosphate-buffered saline solution at pH 7.4 and 37 °C temperature. A control solution was prepared after dissolving coptisine in methanol at the same concentration as carbon dot-loaded coptisine. The graph of accumulated drug release as a function of time in hours clearly showed that the control solution released the drug fast in comparison to the coptisine loaded carbon dots after four hours, indicating sustained drug release. The cytotoxicity of both the control and the coptisine loaded carbon dots was also investigated. Coptisine exhibits increased antitumor efficacy in contrast to the control solution with different concentrations. Several organs of mice were also investigated using fluorescence images after one day of injection of the control solution and the coptisine loaded carbon dots, Fig. 14(d).[415] Chen *et al.* produced near-infrared emitting carbon dots and embedded them with hollow mesoporous silica nanoparticles through disulphide bonds that are reduced by intracellular glutathione and lead to the delivery of doxorubicin hydrochloride as a nanocarrier into cells. When the hollow silica nanoparticle doped disulphide linked and doxorubicin hydrochloride loaded carbon dots were injected in the tumour region, the citraconic anhydride-modified polylysine molecule present on the surface of the nanocarrier helped in the physical adsorption by the cancer cell because of the mildly acidic nature of the tumour environment. After this procedure, the disulphide bond was broken down, following the quick delivery of doxorubicin hydrochloride into the cancer cell. As a result, the fluorescence of the carbon dots that was lost due to conjugation, is restored. The carbon dots acted both as a nanocarrier of the drug for the therapeutic treatment and as

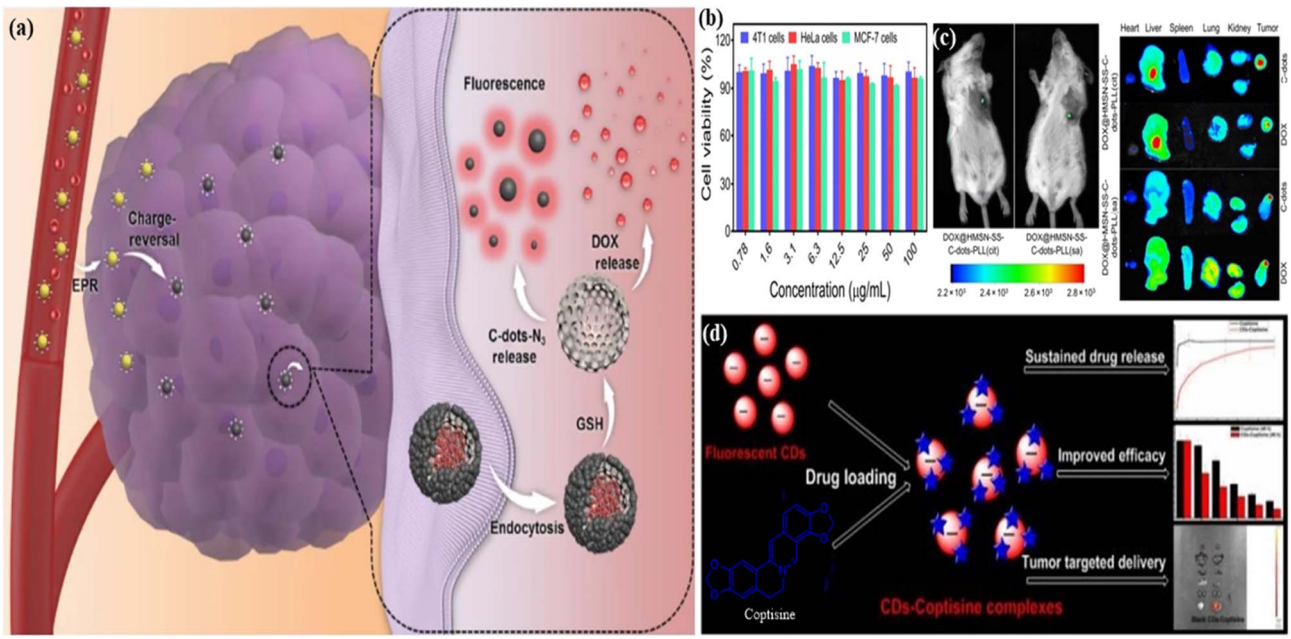

Fig. 14 (a) Graphical representation of red FCNMs as a nanocarrier for drug delivery in the tumour cell with the anticancer mechanism; (b) the cell viability of different types of cells including 4T1 (blue), MCF-7 (green), and HeLa (red) cells; (c) the fluorescence images of breast-cancer infected mice after being injected with the red emissive hollow silica nanoparticle doped disulphide linked and doxorubicin hydrochloride (DOX) loaded carbon dots and biodistribution of the red carbon dots and doxorubicin hydrochloride in the mice, as shown on the side. Reprinted with permission from ref. 416, Copyright 2021, Springer; (d) the illustration of the red carbon dots as a nanocarrier of coptisine for effective therapy of cancer with several advantages including sustained drug release, improved efficiency and tumour targeted delivery. Reprinted with permission from ref. 415, Copyright 2021, Wiley-VCH GmbH.

a fluorescence imaging agent for the fluorescence imaging of the drug metabolism. The carbon dots showed excellent cell viability, Fig. 14(b). A cancer-affected cell model of mice was demonstrated in this report. The fluorescence image of the breast-cancer infected mice after injecting the red emissive hollow silica nanoparticle doped disulphide linked and doxorubicin hydrochloride loaded carbon dots was captured and investigated, in Fig. 14(c). The fluorescence images of the biodistribution of the red carbon dots and doxorubicin hydrochloride in the mice were also captured to check the drug metabolism and for fluorescence bioimaging, Fig. 14(a).[416] Cong *et al.* fabricated red fluorescent carbon dots *via* a hydrothermal method. These red carbon dots are modified with polyethylene glycol polymer to deliver doxorubicin hydrochloride through control release.[417]

5.2. *In vivo* and *vitro* sensing

Fluorogenic sensing is widely utilized for the identification of biomolecules or metal ions or the pH of the solution because of its high sensitivity, high selectivity, high specificity, high resistance for light scattering and ease of use. The difference between the fluorescence intensities of the reference and sample is utilized to determine the sensing target both qualitatively and quantitatively when excitation by light energy occurs.[418,419] The main requirements for a good sensor are target selectivity, strong response, great stability, very low limit of detection, and very high sensitivity. Various types of fluorogenic sensors have been reported till now.[420,421] Among them, red FCNMs attract a lot of attention as a sensor *in vivo* and *in vitro* because of their small size, low toxicity, easy-to-surface modification, excellent stability, tunable behavior, high signal-to-noise ratio and large penetration depth.[422] Mainly are there three types of sensing including metal ion sensing, organic molecule sensing and pH sensing.

5.2.1. Metal ion sensing. Although metallic ions are essential for many chemical and biological processes, their widespread use is hazardous to the environment and human health. So, it is essential to identify metal ion contaminants in water solution.[423,424] Gao *et al.* reported stable low cytotoxic red carbon dots in both solid and aqueous phases. These red emissive carbon dots are used for the fluorogenic detection of di-valent platinum, tri-valent gold, and di-valent palladium in PC12 cells and zebrafish.[425] Wang *et al.* synthesized red fluorescent carbon dots by the solvothermal treatment of binaphthyl diamine and citric acid. The red fluorescence properties of the as-synthesized carbon dots are used for the identification of ferric ions and fluoride ions with a good limit of detection value.[197] Li *et al.* demonstrated the selective and sensitive detection of aqueous contaminant tri-valent gold ions using their developed red emissive carbon dots, within two minutes by both colorimetric and fluorometric ways. The red carbon dots had an emission wavelength of 637 nm at an excitation wavelength of 520 nm. The detected gold ions can be recovered *via* a redox reaction, Fig. 15(b).[199] Tan *et al.* prepared red fluorescent carbon dots *via* an acid-supported hydrothermal treatment and used these as-developed red carbon dots for the selective and sensitive sensing of ferric ions.[426] Zeng *et al.* fabricated red fluorescent sulphur doped carbon dots by thiourea-based hydrothermal treatment for the identification of toxic di-valent mercury ions and glutathione *via* a fluorometric titration process.[427] Pawar *et al.* developed nitrogen-doped red fluorescent carbon dots from a mixture of nitric acid and amino benzoic acid for the selective dual detection of tri-valent indium ions and di-valent palladium ions in water with the help of fluorescence quenching. The selectivity of the red carbon dots towards indium and palladium ions among sixteen other ions is represented *via* a bar diagram plot of the fluorescence intensity as a function of various metal ions, Fig. 15(c). The fluorescence quenching effect was also shown in a graphical plot of fluorescence intensity as a function of emission wavelength, Fig. 15(d). It was seen that the red colour fluorescence intensity decreased with the addition of di-valent palladium ions and the intensity shifted to red when the solution of tri-valent indium ions was added to the red carbon dot solution, Fig. 15(e). The presence of the lone pair of electrons of the oxygen atoms at the surface causes surface oxidation followed by a reduction in the energy gap. As a result, there was a red shift in the emission. When di-valent palladium ions were added to the red carbon dots and excited with UV light, the electrons present in the LUMO jumped to the vacant d-orbital of the palladium ions and split the d-orbitals. The binding of oxygen with palladium ion reduces the lone pair of electrons in the oxygen atom. In conclusion, the band gap has increased and restricted the radiative recombination process, followed by the blueshift of wavelengths or quenching in the intensity. In contrast, when tri-valent indium ions were added to red carbon dots, complexes were formed with the oxygen atom. The sharing of lone pair electrons was stopped due to the filled d-orbital of the tri-valent indium ions. As a result, the concentration of the lone pair will increase and create a new energy level, causing reduction of the band gap followed by red shift and an increase in the intensity of fluorescence, Fig. 15(f).[428] Bhati *et al.* synthesized biocompatible red-emitting magnesium and nitrogen co-doped carbon dots for the selective detection of divalent copper metal ions in a water medium. The red fluorescence is caused by several factors, including the size, presence of conjugations, and functional groups containing magnesium, nitrogen, and oxygen atom. The copper ions formed a complex with oxygen functional groups when di-valent copper was treated with the red carbon dots, leading to the quenching of fluorescence, Fig. 15(a).[429]

5.2.2. Organic molecule sensing. Organic molecules are so harmful and cause several problems including headaches, irritation of the eyes, nose and throat, nausea and loss of coordination. They also lead to fatal damage to the human kidney, liver and nervous system. Human and animal cancers are also caused by organic dyes. Therefore, it is essential to sense these hazardous organic molecules in aqueous medium.[430–432] Hu *et al.* fabricated excitation-dependent dual emissive red fluorescent carbon dots by acid-assisted hydrothermal treatment for rapid selective and sensitive identification of methyl blue, an organic pollutant.[433] Chen *et al.* conjugated red emissive carbon dots with diethyl

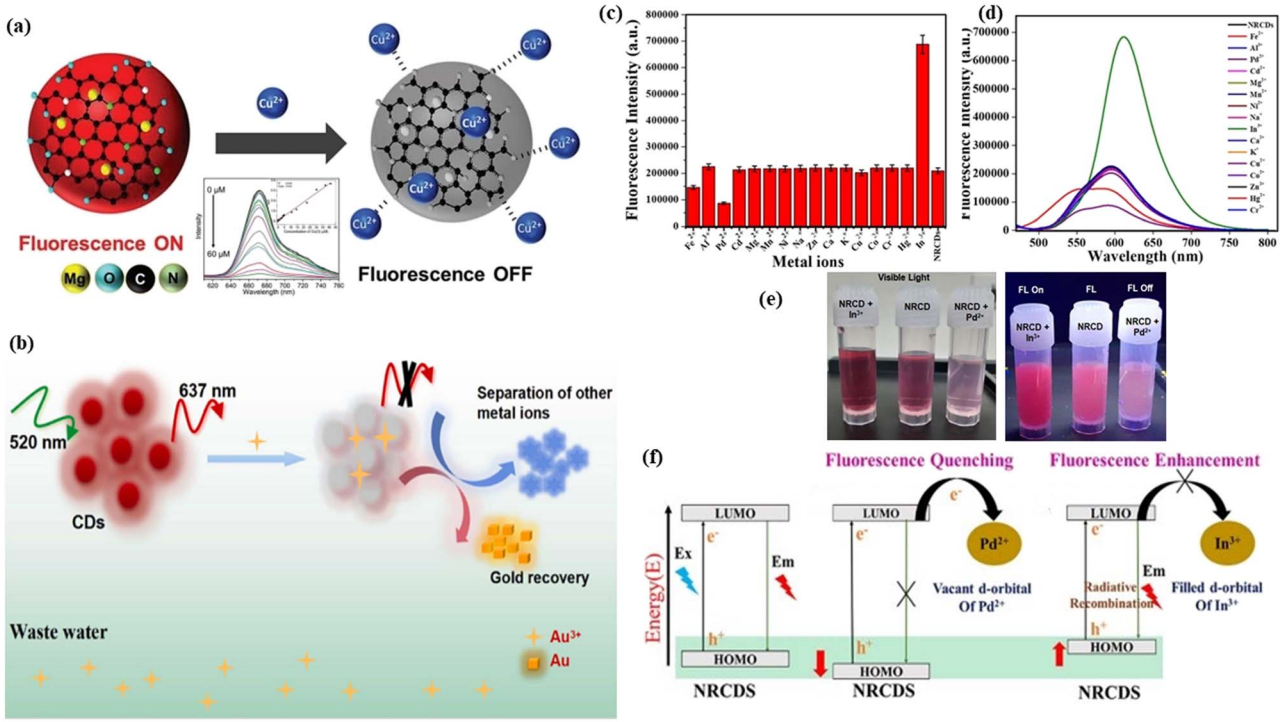

Fig. 15 Schematic illustration of metal ion sensing: (a) representation of the fluorescence quenching noted as fluorescence "ON–OFF" as a result of di-valent copper interactions with red carbon dots, and the fluorescence intensity decreases with increasing concentration of copper ions as shown in the inset. Reprinted with permission from ref. 429, Copyright 2018, Royal Society of Chemistry; (b) the red fluorescent carbon dots with an emission wavelength of 637 nm at the excitation of the 520 nm wavelength for the detection of gold in wastewater as a quenching effect in fluorescence and gold can be recovered *via* a redox reaction. Reprinted with permission from ref. 199, Copyright 2022, Elsevier; (c) the bar plot of the emission intensity changes with various metal ion concentrations at the 460 nm excitation wavelength; (d) the selectivity study of the emission spectra of red carbon dots; (e) the fluorescence "ON–OFF" images of the trivalent indium mixed carbon dots, red carbon dots and di-valent palladium mixed carbon dots at the 365 nm excitation wavelength of UV light with visible light images of the trivalent indium mixed carbon dots, red carbon dots and di-valent palladium mixed carbon dots respectively; (f) the fluorescence and quenching mechanism of red carbon dots, di-valent palladium mixed red carbon dots and trivalent indium mixed carbon dots, respectively. Reprinted with permission from ref. 428, Copyright 2020, American Chemical Society.

phthalate to develop an immunoprobe for the selective and sensitive detection of diethyl phthalate, which is an environmental endocrine.[434] Easy and accurate sequence-specific DNA sensing is essential not only for biomedical research and clinical molecular illness diagnosis, but also for microbiology, food safety, and environmental surveillance. Martínez-Periñán *et al.* developed neutral red carbon nanodots *via* an easy microwave-assisted method within three minutes for the selective and sensitive fluorogenic sensing of specific DNA sequences of *Escherichia coli* bacteria. They observed that the increasing concentration of single-stranded *Escherichia coli* bacteria in the red carbon dots solution increased the intensity of fluorescence emission, Fig. 16(a).[435] Dai *et al.* developed green-red emissive carbon dots through a simple hydrothermal method for selective and sensitive fluorogenic sensing of hazardous synthetic colour acid red 18 in drinks and candy.[436] Zhu *et al.* fabricated uniform spherical red fluorescent carbon dots obtained from an inverse microemulsion surface imprinting process for fluorogenic opto-sensing of Lambda-cyhalothrin, a pyrethroid pesticide. They used red carbon dots and a smartphone to build a hybrid system. The usage of a smartphone as a signal output terminal helps in the identification process. First, the as-synthesized carbon dots were modified with silica nanomaterials using a reverse microemulsion process to enhance the specificity for Lambda-cyhalothrin (LC) pesticides with more recognition sites. The attachment of LC on the surface of red carbon dots occurred *via* an extract-rebind mechanism. With more LC attached to the surface, the concentration of LC gradually rose. As a result, the fluorescence intensity of the red carbon dots significantly quenched. A sensitivity study was performed by using different concentrations of LC shown in the fluorescence plot. An ultraviolet light irradiated light box was made with a software integrated smart phone and polymer plastic to identify the quenching effect by capturing and comparing the brightness images on the side quickly, Fig. 16(b).[437]

5.2.3. pH sensing. Considering the chemical conditions of a solution, pH is a significant parameter. The basicity and acidity of a solution are determined using the pH scale. The pH can affect how readily available nutrients are, how biological processes work, how bacteria behave, and how chemicals behave. Bai *et al.* developed red fluorescent carbon dots *via* a solvent-controlled and dependent approach for sensitive identification of changes in pH followed by color changes. The

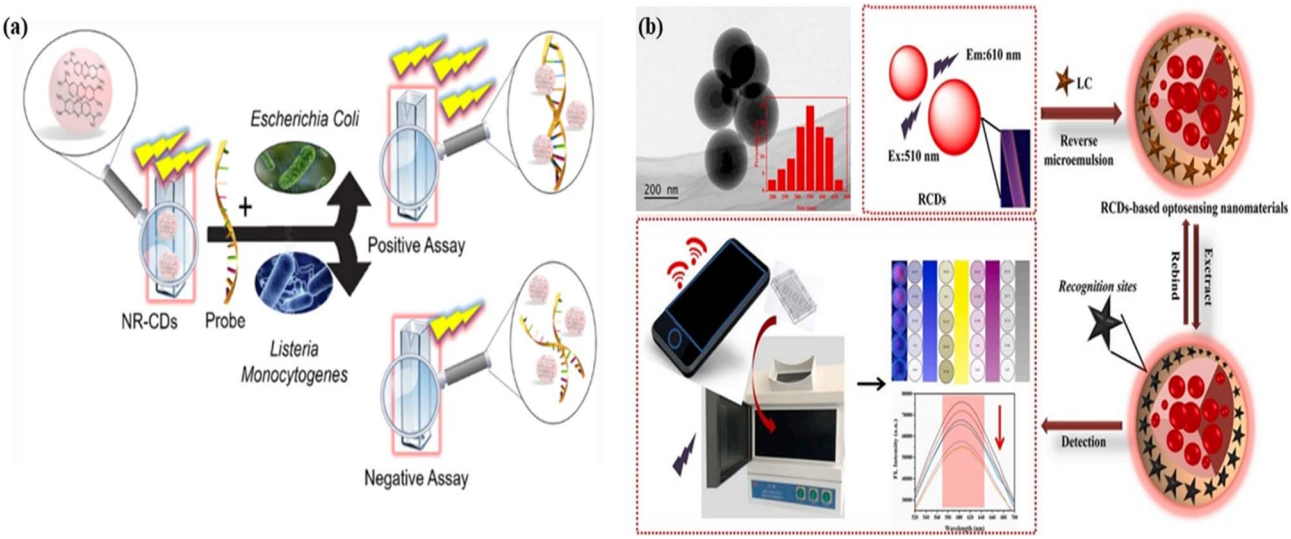

Fig. 16 Graphical representation of carbon dots for sensing of organic molecules: (a) the red carbon dots as a fluorescent probe for the identification of the specific DNA sequence of *Escherichia coli* bacteria. Reprinted with permission from ref. 435, Copyright 2022, Springer; (b) red fluorescent carbon dots with a smartphone-based signal output terminal for the identification of Lambda-Cyhalothrin (LC) pesticides in tea. Reprinted with permission from ref. 437, Copyright 2021, Elsevier.

red carbon dot solution showed a red colour when the pH was maintained between 3 and 10 and showed a green colour when pH was fixed at 1–3, Fig. 17(d).[438] Zhang *et al.* reported photostable red-orange fluorescent nitrogen and sulphur co-doped carbon dots with high quantum yield *via* a solvothermal route for a sensitive fluorogenic response to pH changes in an environmental sample and living cells.[439] Chen *et al.* demonstrated the high photobleaching resistance and biocompatibility of red fluorescent carbon dots for both colorimetric and fluorometric sensitive responses to pH from 4.0 to 8.0 through changing the colour from red to yellow, mainly originated from the reversible transformation between the azo and quinone structures of red carbon dots. The colour change caused by the pH change was seen in the images. The red carbon dot solutions at pH 4 to 8 under daylight (bottom) and under UV light (top) are shown. The possible structural model in an acidic and an alkaline environment is also illustrated in Fig. 17(c).[440] Guo *et al.* synthesized red carbon dots that have high photostability, outstanding biocompatibility, and desirable biological penetration. These as-synthesized red carbon dots are applied to the sensing of pH in living cells by both colorimetric and fluorogenic methods.[441] Ye *et al.* prepared biocompatible carbon dots with red emissive two-photon fluorescence through a hydrothermal treatment for control sensing of the pH of intercellular living cells. The red emissive carbon dots alternate between the ON and OFF modes of fluorescence due to the disaggregation and aggregation of their physical state. The fluorescence intensity of pH-assisted carbon dots reduced linearly as the pH value increased resulting from aggregation caused by the π–π stacking interaction. The rising concentration of H^+ causes the acidic nature and leads to increase in multiphoton absorption, followed by two-photon fluorescence emission. As a result, two photon fluorescence emission peaks were generated at the 690 nm emission wavelength along with the one photon fluorescence emission peak at about 640 nm emission wavelength, when excited by the 573 nm radiation wavelength, Fig. 17(a).[442] Huang *et al.* developed excitation independent red fluorescent carbon dots *via* a solvothermal method using 2-aminophenol for a fluorogenic sensing response to pH 4 to 13. They showed that the emission intensity of the red carbon dot can be further modified by adjusting the concentration of H^+ and OH^-. Conclusively, they used the red carbon dots as a "on–off–on" sensor for the identification of pH, Fig. 17(b).[443] Li *et al.* fabricated biocompatible photostable red emissive carbon dots using hydrothermal treatment of neutral red and thiourea as precursors for the sensitive determination of pH.[444]

5.2.4. Other fields of sensing. There are many other fields where red emissive FCNMs can act as selective and sensitive fluorogenic sensors. Yu *et al.* reported red fluorescent carbon dots for the fluorometric and colorimetric identification of nitrite ions in ham and bacon meat products. They first functionalized the carbon dots with amino groups and then they used then for selective and sensitive detection of nitrite ions *via* the formation of a purple color diazotized salt when NO_2^- reacts with the amino group.[445] Wang *et al.* fabricated solvent-dependent red-shifted carbon dots by enhancing the polarity of the solvent, for the detection of water in an organic solvent *via* an aggregation-induced quenching and solvatochromism effect.[446] Fu *et al.* developed nitrogen and zinc co-doped red fluorescent carbon dots for selective and reversible identification of peroxy nitrite ions, an endogenous toxicant in living cells *via* a redox reversible process.[196] Liu *et al.* demonstrated water-soluble red fluorescent carbon dots through an oxidative polymerization process for the fluorogenic detection of different sulfur-containing molecules.[447] Chen *et al.* developed biocompatible red emissive carbon dots *via* solvothermal pyrolysis for

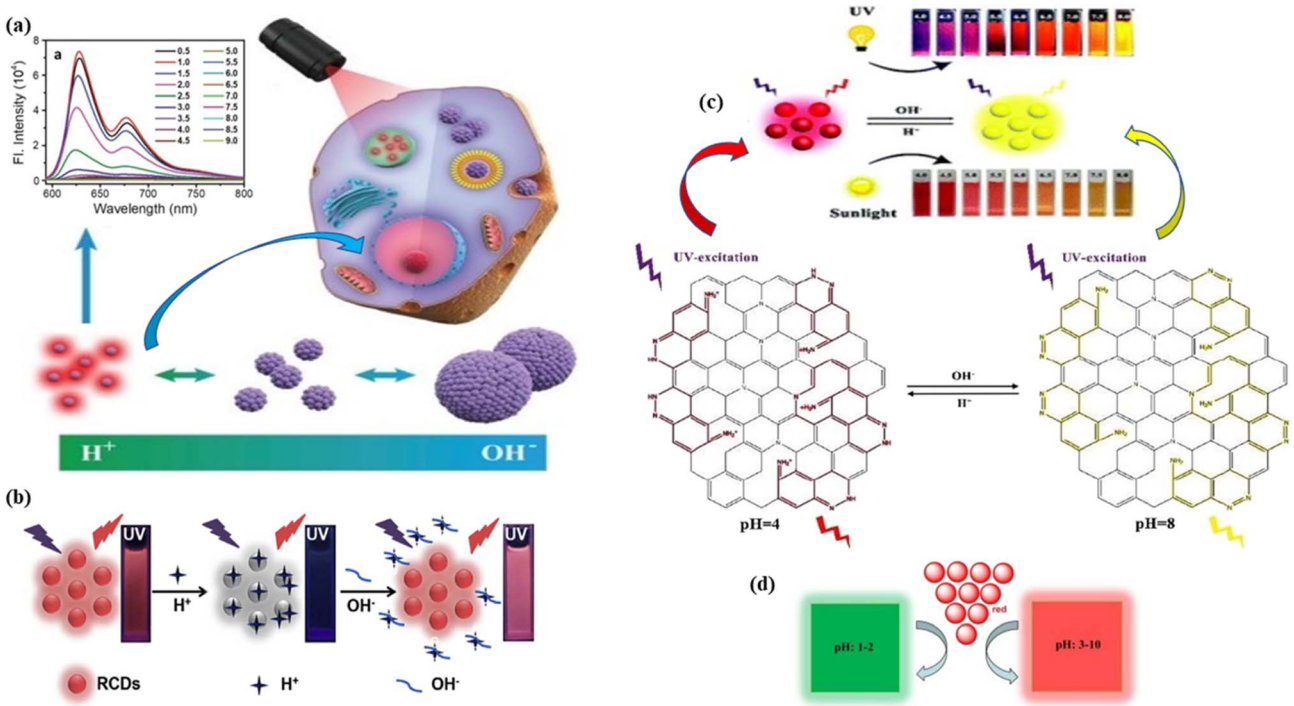

Fig. 17 Schematic representation of pH sensing of red carbon dots: (a) red carbon dots for two-photon pH imaging with pH-dependent fluorescence emission spectra at 573 nm excitation in the inset. Reprinted with permission from ref. 442, Copyright 2019, WILEY-VCH Verlag GmbH & Co. KGaA, Weinheim; (b) the red carbon dot based "on–off–on" sensing of pH with increasing concentration of H^+ (acidic) and OH^- (basic). Reprinted with permission from ref. 443, Copyright 2019, Elsevier; (c) red carbon dots for colorimetric and fluorogenic sensing of pH with structural colour change from red to yellow, when changing the pH from 4 to 8. Reprinted with permission from ref. 440, Copyright 2020, Royal Society of Chemistry; (d) the pH colour change of red carbon dots to green at pH 1–2 and red at pH 3–10. Reprinted with permission from ref. 438, Copyright 2019, Royal Society of Chemistry.

selective sensing of ziram, a fungicide and di-valent mercury ion *via* a buffer solution.[448] Li *et al.* developed hydrothermal treatment-derived red emitting carbon dots as dual-mode carbon dots for the colorimetric and fluorometric on–off–on sensing of hypochlorite and glutathione, which causes oxidative stress and its related diseases. A buffer solution of carbon dots was prepared by adding the carbon dot solution with buffer solution to get dual mode carbon dots. The identification of hypochlorite using both colorimetric and fluorometric was carried out after adding various concentrations of the hypochlorite solution to the dual mode red-emitting carbon dots. Then the addition fluorescence emission spectra were recorded. The same procedure was followed for the detection of glutathione. After preparation the carbon dots emitted red colour emission, when they were excited. But after the addition of hypochlorite, the colour was quenched and recovered again after the addition of glutathione as a reducing substance. So, it can be called an "on–off–on" switchable sensor. Furthermore, the exogenous and endogenous detection of hypochlorite and glutathione in living cells was carried out by incorporating the red carbon dots with various cells and capturing the fluorescence images, Fig. 18(a).[195] Zhao *et al.* synthesized pH-dependent red fluorescent nitrogen phosphorus co-doped carbon dots by hydrothermal treatment of *o*-phenylenediamine and phosphoric acid, for the selective and sensitive detection of malachite green, a toxic chemical found in the fish and water environment. Selectivity measurement of malachite green was performed by examining the red carbon dots with different interfering chemicals including dyes, anions, and metal ions. It was observed that malachite green was selectively sensed by the carbon dots. Later for a sensitivity study, different concentrations of malachite green solutions were first mixed with red carbon dots. Then fluorescence emission spectra were recorded at the 611 nm excitation wavelength. It was seen that the fluorescence carbon dots mixed with malachite green solution were quenched, Fig. 18(b).[449]

5.3. Energy

5.3.1. Light emitting diodes. Light-emitting diodes (LEDs) are solid-state lighting sources consisting of a semiconductor chip or a device that is placed on a reflecting surface. They generate light when electricity passes through them. LEDs are used in diverse fields including display backlighting, communication, medical services, signage, and general illumination. With low voltage and low current functioning, they provide high energy efficiency that leads to a decrease in energy usage.[450,451] As LEDs offer greater temperature control than traditional illuminating sources including CFLs, fluorescent lamps and incandescent lamps, they can last up to 50 000 hours longer. The high performance of LEDs includes microsecond level ultrafast response, a large range of programmable color

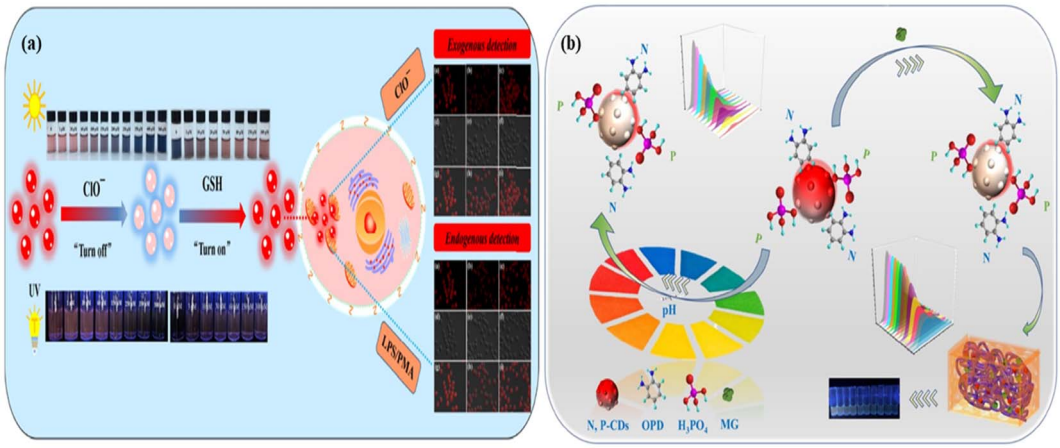

Fig. 18 (a) Schematic representation of red-emitting carbon dots as an "on–off–on" switchable sensor for the detection of ClO^- and GSH and the exogenous and endogenous identification of hypochlorite and glutathione in red carbon dot embedded living cells using fluorescence images. Reprinted with permission from ref. 195, Copyright 2022, Elsevier; (b) schematic representation of red-emitting nitrogen and phosphorus co-doped carbon dots for the detection of toxic dye malachite green and pH. Reprinted with permission from ref. 449, Copyright 2023, Elsevier.

temperatures including 4500 K to 12 000 K, and a larger operating temperature range including −20 °C to 85 °C. Because of their low UV radiation and lack of mercury, LEDs are also sustainable and environment-friendly products.[452,453] LEDs can illuminate light in a wide range of spectral bands including red, yellow, green, and blue from small bands to a larger white light band with a variable distribution of illuminating strength. LEDs generate light due to the electroluminescence phenomenon that occurs at the p–n junction. When a p–n junction is driven in the upward orientation, holes are pumped from the p-junction across the active layer into the n-junction, and electrons in the n-junction have enough energy to flow across the boundary layer into the p-junction.[454,455] FCNMs attracted attention as light emitting diodes for having superior optical properties, high photostability, low cost, and ease of synthesis. Solid-state FCNMs showed a notable fluorescence redshift in contrast to their aqueous solution due to supramolecular crossing-linking between neighboring carbon nanomaterials, indicating the possibility for solid-state light emitting diode (LED) applications.[456–458] Zhang *et al.* reported high thermal and photostable red fluorescent carbon dots with self-quenching resistant properties. The red carbon dots were integrated with Ce^{3+}:$Y_3Al_5O_{12}$ to develop high-quality warm white light-emitting diodes.[459] Cai *et al.* prepared red, blue and green fluorescence carbon dots with solubility in both aqueous solutions *via* a solvothermal treatment. The individual polymer coated red, green and blue composites glow with bright red, green and blue colours respectively, when under 360 nm wavelength excitation, Fig. 19(i). The as-prepared blue, green and red carbon dots were mixed with polyvinylpyrrolidone polymer to build ultraviolet-assisted white light-emitting diodes, which cover the entire range of visible light. The fluorescence spectra of the mixed carbon dot coated polymer composite are illustrated at excitation 360 nm and 340 nm wavelengths in Fig. 19(k). The CIE colour coordinate of the developed white light-emitting diodes was calculated to be (0.33, 0.33), similar to sunlight, Fig. 19(j). The fluorescence spectrum of white light emitting diodes maintained good luminescence with very low photobleaching, following a 15 day exposure to ultraviolet light, Fig. 19(l).[460] Zhu *et al.* developed red fluorescent carbon dots by the surface modification of nitrogen *via* treatment with hexadecyl trimethyl ammonium bromide. They dissolved the red carbon dots with blue and green carbon dots to develop UV-excited white light-emitting diodes with a high colour rendering index.[461] Zhai *et al.* fabricated red-emitting carbon dots and green-emitting carbon dots. The green-emitting carbon dots are mixed with starch to get luminescence solid-state phosphor materials. Similarly, red carbon dots are mixed with polyvinyl pyrrolidone polymer to get solid-state phosphor materials. The green and red phosphors were mixed with epoxy-silicone to get differently shaped luminescent materials without changing the initial fluorescence wavelength. Under blue light excitation, the green phosphor glows with bright green light and the red phosphor glow with bright red light under green light excitation, Fig. 19(g). When both blue and red phosphors were installed in commercially available blue-emitting InGaN LED chips (with an emission peak at 450 nm) and after solidification for one hour at 80 °C, a cool WLEDs with CIE color coordinates of (0.27, 0.28) and CCT of 12 942 K were derived, Fig. 19(a). The emission spectra of the cool white light emitting diodes were also recorded, inset of Fig. 19(a). A WLED prototype was achieved by first exciting the green phosphors, and then red phosphors, Fig. 19(h). A yellow-green light was emitted when the green phosphor was taken under the blue-emitting InGaN LED chips, Fig. 19(b). The CIE colour coordinate chromaticity plot of both WLEDs and yellow LEDs was obtained, Fig. 19(c). Various colour pen caps were taken under produced WLEDs to confirm the e-colour rendering properties, Fig. 19(d). The same experiment was done under sunlight, Fig. 19(e). No such difference was found. The emission spectra of the working WLED are

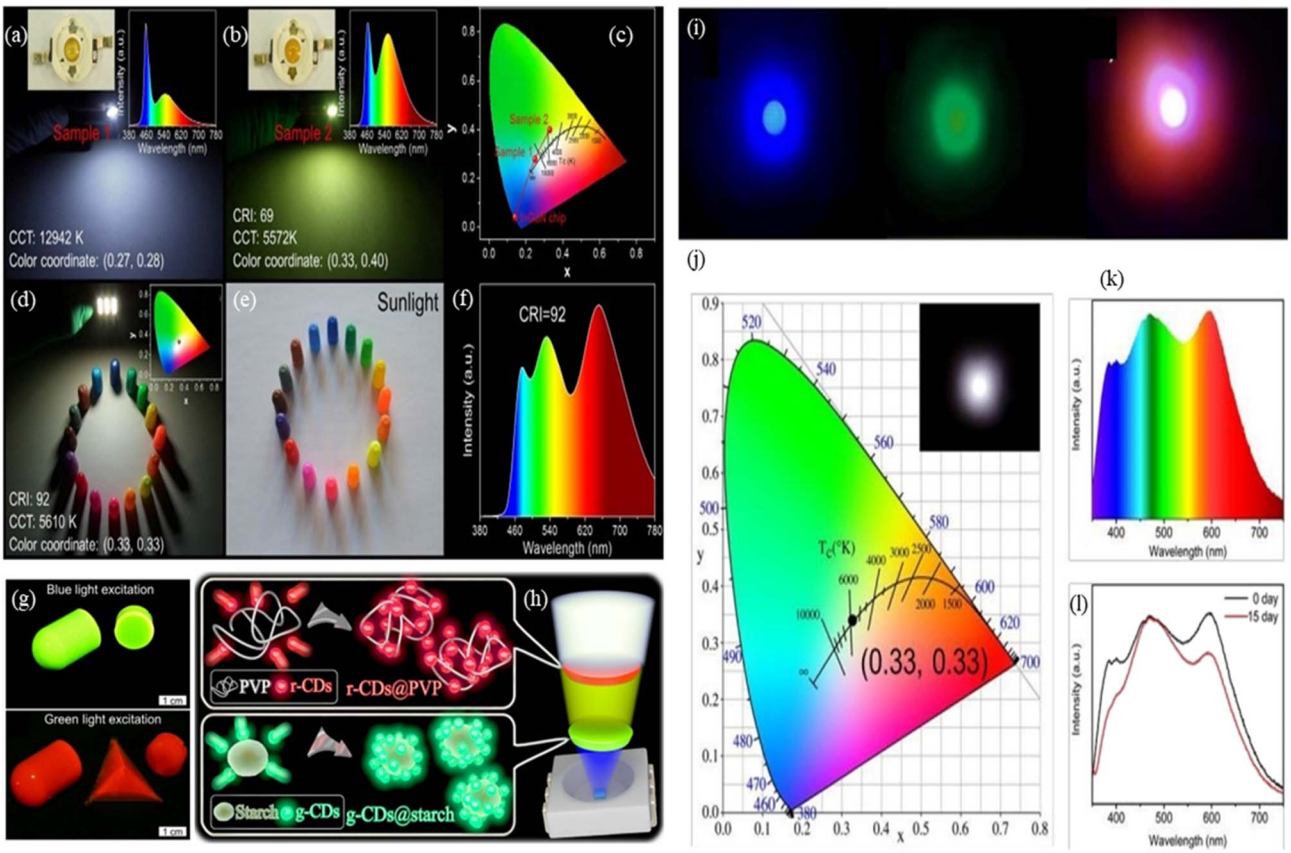

Fig. 19 Schematic representation of the FCNM based LEDs: (a) optical image of the cool WLED with a CIE colour coordinate of (0.27, 0.28) and a CCT of 12 942 K and the emission spectrum of the cool WLED is shown in the inset; (b) optical image of a yellow green LED with a CIE colour coordinate of (0.33, 0.40), a CCT of 5572 K, and a CRI of 69 and the emission spectrum of the yellow green LED is shown in the inset; (c) diagram of the CIE chromaticity colour coordinates of the cool WLED and yellow green LED; (d) image of various colour pen caps under working WLEDs with a CIE colour coordinate of (0.33, 0.33), CCT of 5610 K and CRI of 92 and the high CRI diagram of the CIE chromaticity colour coordinate of WLEDs in the inset at the right top corner; (e) image of various colour pen caps under daylight; (f) the emission spectrum of WLEDs as shown in (d); (g) carbon dot based green phosphors & epoxy-silicone resin under a long pass 495 nm blue light filter (top) and carbon dot based red phosphors & epoxy-silicone resin under a long pass 550 nm green light filter; (h) testing of the WLED prototype with the first excitation of the green phosphors, and then red phosphors, thereby achieving white light. Reprinted with permission from ref. 462, Copyright 2018, Elsevier; (i) the images of the monochromatic blue, green and red LED devices derived from polyvinylpyrrolidone-coated carbon dots, under same excitation; (j) the CIE colour coordinates of the white LEDs, the photo of the WLEDs upon excitation is shown in the inset; (k) the emitting light spectrum of WLEDs; (l) the emitting spectrum of WLEDs before and after 15 days, respectively. Reprinted with permission from ref. 460, Copyright 2019, Royal Society of Chemistry.

illustrated, in Fig. 19(f). The produced white light emitting phosphor illuminated very brightly under UV light excitation with a high colour rendering index and colour coordinate.[462] An *et al.* reported red carbon dots using solvothermal treatment of 1,4-diaminonaphthalene. The red carbon dots possess a tunable emission wavelength when treated with various organic solvents. The red carbon dots are utilized as red light-emitting diodes.[463] Kumari *et al.* produced red, orange and green colour emitting carbon dots for colour emitting diodes. The multicolour carbon dots are mixed with polyvinyl alcohol to get red, orange and green phosphors individually. A fluorescent solid polymeric film is prepared by combining the three phosphors for the application of monochromatic and white light-emitting diodes.[464]

5.3.2. Photocatalysis. In the photocatalytic process, pairs of chemical reactions are stimulated by the energy of light.[465] When light is absorbed by the molecule, it is excited and an activated electron–hole pair is created as a result. The electron present in the valence band is excited by the energetic photons and goes to the conduction band. These result in the formation of vacant space at the position of the excited electron in the valence band. The electron–hole pair mechanism leads to oxidation and reduction processes.[466,467] Typically, photons or light illumination from UV light or visible light energize the catalyst, which drives the electron transfer mechanism into the reactant, resulting in both oxidation and reduction reactions simultaneously. The highest optimum rate of reaction must involve both the oxidation and reduction reactions at the same time.[468,469] FCNMs emerged as a better photocatalyst compared to the conventional photocatalysts including TiO_2, ZnO, WO_3, $BiPO_4$, Bi_2O_3, BiOX (where X = Cl, I, and Br) and $BiVO_4$ due to their low-cost easy synthesis method, non-toxicity, and excellent

photophysical and photochemical properties. FCNMs show great electron acceptor and donor characteristics and they can effectively control the electron–hole recombination process. Specially, red FCNMs exhibit a wide range of absorption wavelengths starting from UV-visible to near infrared (NIR)/infrared (IR) regions under solar light illumination.[470,471] Khare *et al.* reported bright red luminescent excitation independent zinc doped carbon dots with high quantum yield for the photoreduction of aqueous phase hexavalent chromium to trivalent chromium under the illumination of sunlight. They described the photoreduction process by a simple plot of the relative concentration of chromium as a function of time (minutes). They examined the photoreduction process under several conditions. First, they mixed carbon dots with 100 ppm chromium solution with shaking for 30 minutes under dark conditions. The reduction was achieved after 300 minutes in the dark and only 27% of hexavalent chromium was reduced which is shown by a blue line. A maximum of 99% of hexavalent chromium was reduced under sunlight and shown by the red line. A control experiment was also run and shown by the pink line. A separate same experiment with 50 ppm chromium solution was also run, and the result was shown by a black line, Fig. 20(c). They illustrated a possible mechanism, consisting of three parts. The reduction of water caused by the photogenerated holes in the valence band resulted in the production of O_2 and H^+, which occurs in the first step. The electrons generated by photoexcitation and the H^+ ions target the hexavalent chromium to reduce it to trivalent chromium, as illustrated in the second step. In the last step, defects in carbon dots play a crucial role in the photoreduction approach by bringing hexavalent chromium close to the active region of the carbon dot surface for the redox reaction, Fig. 20(d).[472] Bhati *et al.* proposed a simple microwave synthesis method for red emissive magnesium nitrogen-doped carbon dots from *Bougainvillea* plants. This as-synthesized optical material is used as a photocatalyst under sunlight illumination for the deterioration of methylene blue, a pollutant dye. The team explained a higher rate of photodegradation under sunlight, in contrast to artificial tungsten light *via* a photodegradation plot of methylene blue, Fig. 20(a). They examined the excitation-dependent emission of

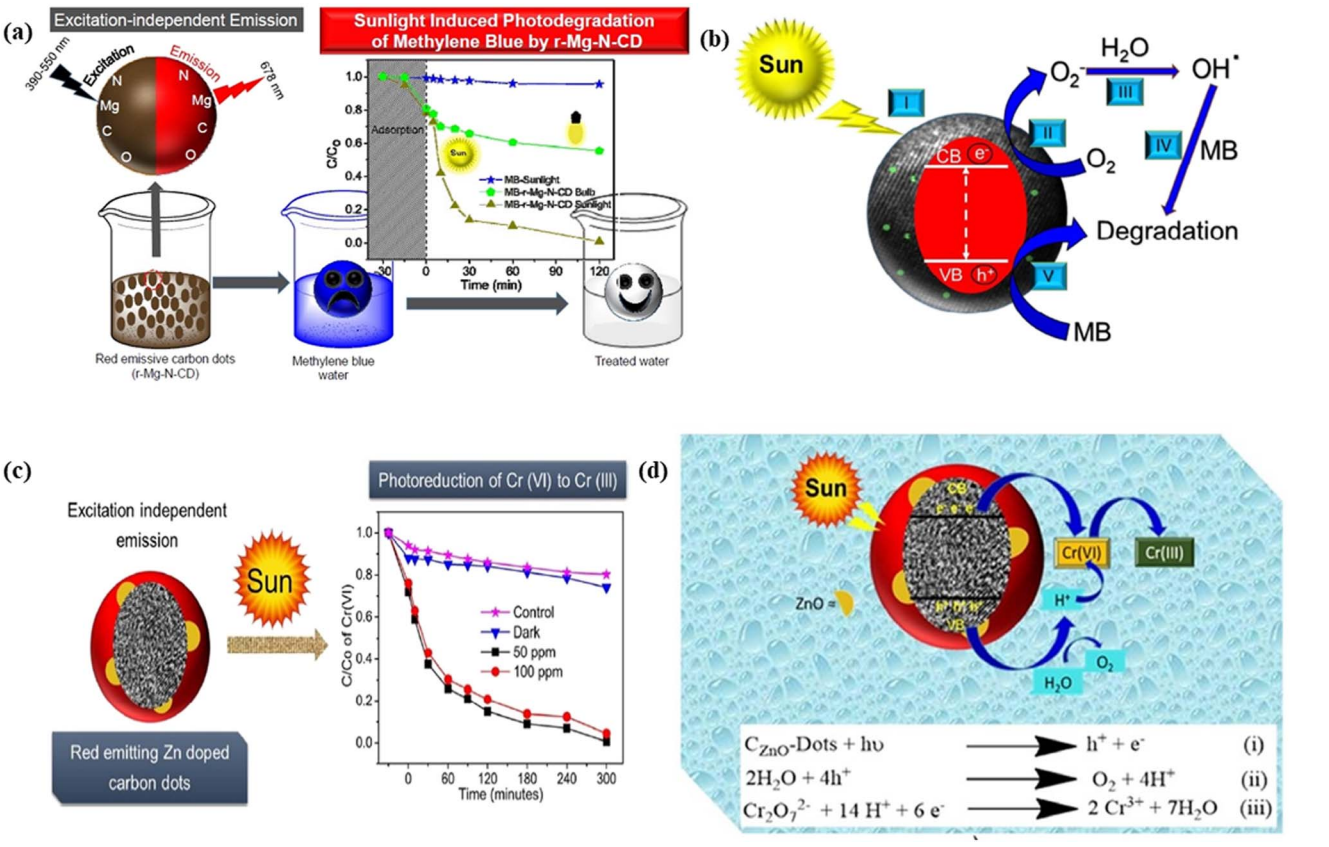

Fig. 20 Schematic representation of several photocatalysis processes of red fluorescent carbon dots: (a) excitation dependent emission of magnesium and nitrogen doped red carbon dots utilized in the sunlight induced photodegradation of methylene blue, the photodegradation plot of methylene blue and methylene blue mixed graphene quantum dots under 120 minutes of sunlight illumination, tungsten bulb light and in the dark with the colour change effect of methylene blue solution as an effect of photodegradation is shown in the inset; (b) mechanism of red carbon dot assisted photodegradation of methylene blue (MB) with various pathways including I, II, III, IV and V. Reprinted with permission from ref. 186, Copyright 2018, American Chemical Society; (c) the utilization of the excitation dependent red emitting zinc doped carbon dots in the aqueous-phase photoreduction of hexa-valent chromium to tri-valent chromium, under sunlight illumination with the photoreduction graph of the relative chromium concentration as a function of time under different conditions; (d) possible photoreduction mechanism of hexavalent chromium to trivalent chromium under light. Reprinted with permission from ref. 472, Copyright 2018, American Chemical Society.

magnesium and nitrogen-doped red carbon dots in the sunlight-induced photodegradation of methylene blue. Various procedures were carried out, including the use of methylene blue and methylene blue mixed carbon dots in the dark, under a tungsten bulb light, and for 120 minutes of solar illumination respectively, Fig. 20(a). The colour change of methylene blue solution occurred after the photodegradation process, Fig. 20(a). Additionally, they provided a five-step hypothetical mechanism. The photoinduced electron from the sun is captured by the functional group present on the surface of the red carbon dots, leading to the surface defect state, marked as path I. Path II indicates that the electrons present in the graphitic layer of the carbon dots are excited by light, which leads to a delay in the recombination of electron–hole pairs and produces reactive oxygen species as an intermediate on the surface of the carbon dots. Paths III–IV illustrated that the methylene blue reacts with the reactive oxygen and breaks down into small hydrocarbons, confirmed by NMR examination, Fig. 20(b).[186] Li *et al.* developed a near IR light-regulated metal-free photocatalytic system of carbon dots for the conversion of benzaldehyde from benzyl alcohol *via* a selective oxidation approach.[473] Yang *et al.* prepared TiO_2-sensitized red fluorescent carbon dots for the photocatalytic production of hydrogen from methanol.[474]

5.3.3. Solar energy. The energy demand of today's world is growing day by day with the increase of the global population. Most of the nations depend on fossil fuels for energy resources including electricity. Using fossil fuels produces higher carbon emissions as this process emits CO_2 as a by-product. This results in global warming, followed by climate change. Solar energy is one of the most commonly used renewable sources all over the globe. The sun deposits approximately 86 PW of energy onto the surface of the Earth annually. Solar energy is the sunlight that has been transformed into thermal or electrical energy.[475–477] FCNMs are quickly gaining attention in solar technology due to their low cost, non-toxic nature and exceptional optical characteristics compared to costly perovskite or heavy metal-based fluorophores.[478,479] The term "LSC" stands for "large-area sunlight collector". The luminescent solar concentrator is a translucent rectangular piece of glass or polymer material as a light guide plate that has been coated with fluorescent materials. The fluorescent materials absorb light from the sun. As a result, the fluorescent materials are illuminated immediately and the downshifted photons propagate through an internal reflection process to the edges of the rectangle light guide, where the photons are absorbed by the thin photovoltaic cell, Fig. 21(a). It is a promising straightforward technology to harvest solar energy. Various optical phenomena also occur during the whole process including the absorption of sunlight, transport of the downshifted photons and their absorption by the photovoltaic cells, Fig. 21(b).[480]

Liu *et al.* developed a red fluorescent carbon quantum dot-based large-area sunlight collector named a luminescent solar concentrator (LSC) for the conversion of solar to electricity so effectively. The as-synthesized carbon dots have a broad absorption region, large Stokes shift value, and high quantum yield, which are advantageous for developing red fluorescent embedded LSCs, Fig. 22(e). They find the interspace distance-dependent efficiency of LSCs by examining the changes in fluorescence intensity with changing the distance. It is shown from a graph, Fig. 22(a), that the intensity enhanced with a lower distance of illumination from the edge, and this is the indication of very weak reabsorption loss. It is also clear from the graph of normalized fluorescence as a function of the distance, Fig. 22(b). The fluorescence emission intensity of red-emitting carbon dots decreased with increased interspace distance between the spot of the beam and the edge of the LSC because of reabsorption followed by reabsorption loss, as shown in the inset of Fig. 22(b). Generally, reabsorption loss is caused by the re-absorption and re-emission, non-absorption of

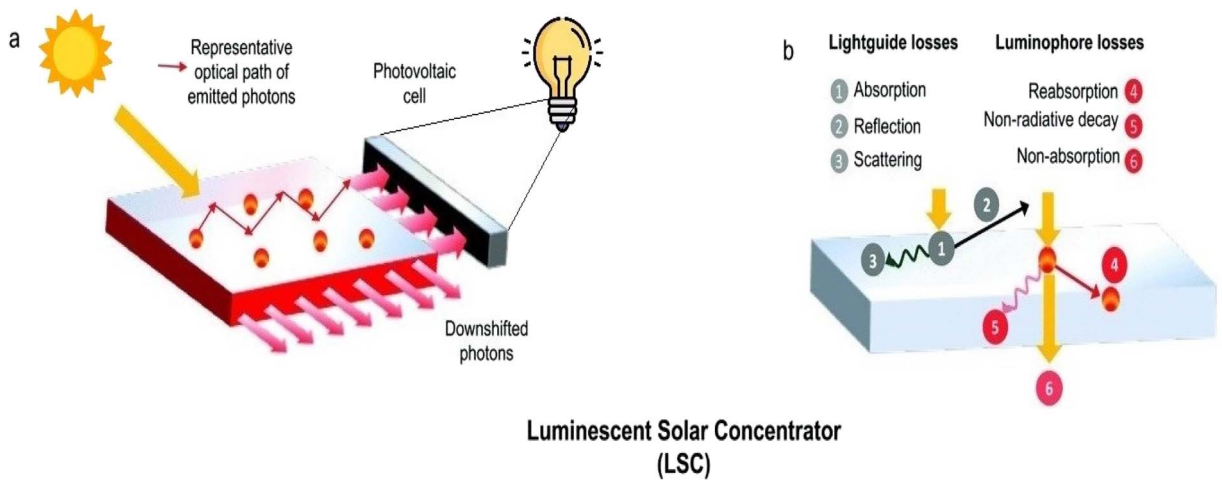

Fig. 21 Graphical representation of luminescent solar concentrator: (a) A fluorophore-coated light-guided plate absorbs the emitted photons of the sun. Then the downshifted photons are transported through total internal reflection to the edges of the light guide. A small photovoltaic cell is placed at one of the edges of the plate to capture the optically concentrated sunlight. A small bulb is illuminated when connected to the photovoltaic cell. (b) Various optical phenomena happen with the absorption of sunlight, transport of the downshifted photons and their absorption by the small photovoltaic cell. Reprinted with permission from ref. 480, Copyright 2021, Royal Society of Chemistry.

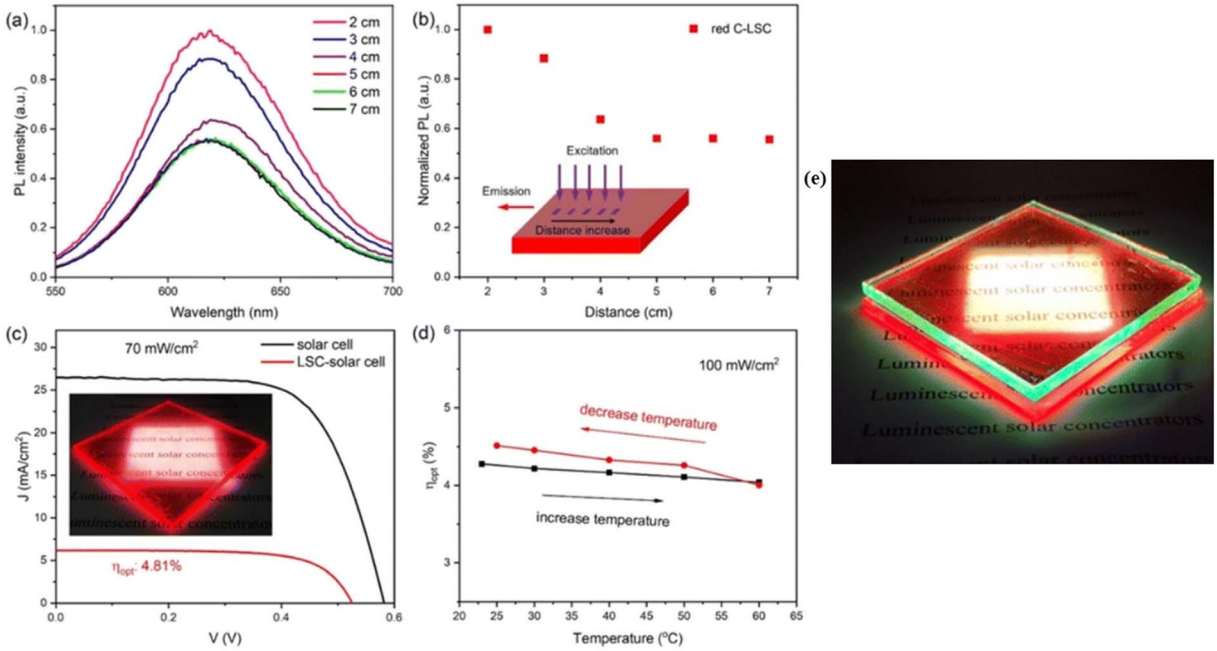

Fig. 22 (a) Fluorescence intensity spectra from various interspaces of illumination from the edge of the light guide; (b) total fluorescence intensity as a function of the interspace distance of the illumination from edges; a schematic for the measurement is shown in the inset; (c) the power conversion efficiency (η_{opt}) is evaluated from the current density (J) as a function of voltage (V) of the luminescence solar concentrator system under daylight, and the photograph of a red emissive solar concentrator under solar illumination is shown in the inset; (d) the relationship between temperature changes and variations in the power conversion efficiency of the luminescence solar concentrators; (e) real life luminescence solar concentrators glowing under the illumination of light in the laboratory. Reprinted with permission from ref. 481, Copyright 2023, Royal Society of Chemistry.

the incident light, partial photon loss, surface reflection, and the escape of light below the critical angle. The power conversion efficiency (η_{opt}) was calculated from the relationship between the current density (J) and voltage (V) of the luminescence solar concentrator system under daylight and it was close to 4.81%, Fig. 22(c). The temperature dependence of the efficiency was also evaluated. As can be observed, the power conversion efficiency steadily dropped as the temperature rose from room temperature to 60 °C. The power conversion efficiency rose as the temperature dropped until it reached the adjacent room temperature, Fig. 22(d).[481] Han *et al.* reported biocompatible red and green carbon quantum dots, having a 300–650 nm broad absorption range. Furthermore, they combined red and green carbon dots *via* a vacuum heating approach to obtain two slab-incorporated tandem structured LSCs with greater efficiency.[482] Cai *et al.* fabricated boric acid functionalized red emissive broadband absorption graphene quantum dots with a high quantum yield to develop high power conversion efficient LSCs. The developed graphene quantum dots showed vibronic-coupled excitonic emission due to the crystalline graphitic structure and hydrogen bonding functionalities. These capabilities of graphene quantum dots help to build highly effective LSCs.[483] Li *et al.* developed a novel and highly effective tandem LSC by mixing red luminescent carbon dots with yellow emissive carbon dots. The as-developed LSC showed big advantages for building integrated photovoltaics.[484] Ali *et al.* proposed surface modification-dependent carbon quantum dots (CQDs) with multicolor emission. Among them, the red emissive CQDs showed the largest Stokes shift and better electrocatalytic activity, causing an increase in surface reactivity and charge transfer. The red CQDs are embedded with carbon nanotubes (CNTs) to remove the aggregation-induced quenching of electrocatalytic activity and increase the conductivity. The red CQD-doped CNTs are used as a counter electrode in solar cells.[485] Dey *et al.* reported red emissive graphene quantum dots (GQDs) synthesized using a polar aprotic solvent with increasing nitrogen units in the GQDs. The red GQDs showed superior photovoltaic performance due to the charge transport properties and higher absorptivity and carrier density.[486]

5.4. Others

5.4.1. Anticounterfeiting. A critical, global issue that has persisted for a long time is the rapid rise of the counterfeiting market for practically all goods, including currency, fuel, medications, coatings, and labels. Even important information is imitated to steal money from bank accounts. This issue has a significantly negative impact on the global economy, human health, and scientific advancement.[487–489] Therefore, it is imperative to create advanced anti-counterfeiting technology to deal with the effects of counterfeiting on diverse fields and protect the welfare of consumers. Numerous anti-counterfeiting techniques, such as barcoding, watermarking, the digital

signature standard (DSS), radio frequency identification tags (RFIDs), holograms, and fluorescent tags or levels, have been employed so far.[490–492] Fluorescent tags or levels stand out among the competition due to their low cost, straightforward approaches, appealing multicolor coding, and stimulus-responsive encryption decryption techniques. Fluorescent materials are used to make fluorescent tags or levels. The most preferable high-security level anticounterfeiting technology is obtained by embedding fluorescence materials with tunable and controlled emissions under various stimuli into a security system.[493–496] FCNMs are booming these days as an anticounterfeiting material because of their great fluorescence properties, tunable emission, easy of functionalization, high stability, biocompatibility, eco-friendliness and cost-effective synthesis methods. The FCNMs have great advantages compared to semiconductor metal nanomaterials, rare-earth doped nanomaterials, inorganic perovskite nanomaterials and polymer nanomaterials due to their inherent characteristics.[497–499]

Dong *et al.* reported red fluorescent carbon dots with starch to form a hybrid phosphor for the detection of latent fingerprints more accurately on glass, paper and plastic by the powder dusting method *via* high contrast red fluorescent signals. The team detected latent fingerprint images on glass, paper and plastic. The arches, loops and whorls of the fingerprint are identified by highly contrasted red bright fluorescent signals, resulting in great identification information in the analysis of fingerprint, Fig. 23(A), (B) and (C). The characteristic marked points of bifurcation, island, termination, eye, core, ridge divergence, and crossover are also recognized so nicely for further analysis, Fig. 23(D). The fluorescent fingerprint images stand by for several weeks without any loss, Fig. 23(E).[500] Yuan *et al.* demonstrated a dual-mode anti-counterfeiting technology with the help of red emissive boron-doped carbon dots, which shows a reversible switching emission after doping with boron. The acid-induced discoloration technique is mainly used in this anticounterfeiting application.[501] Yang *et al.* showed aggregation-induced on–off emission phenomena of red emissive hydrophobic carbon dots, caused by the limitation of intermolecular rotation of the surfaces around the –SS– bond. The turning on–off red fluorescence properties of the hydrophobic carbon dots were used in anticounterfeiting and dual encryption applications.[502] Liao *et al.* developed a photoswitchable carbon nanomaterial embedded with the copolymers of styrene and spiropyran. The team showed that the fluorescence colour switches between red, green and blue when excited by UV radiation and could be used in anticounterfeiting

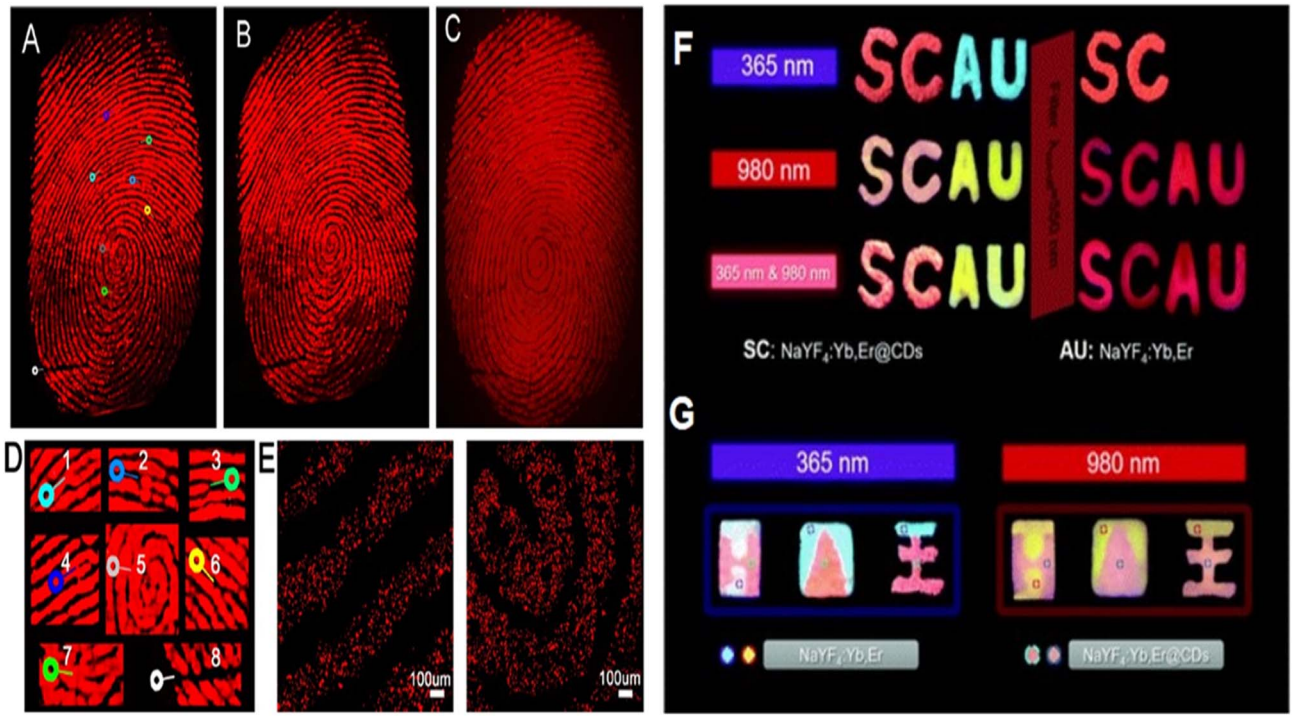

Fig. 23 Red fluorescent starch embedded carbon dot dipped fingerprint images on (A) on glass; (B) on paper; (C) on plastic, under green light excitation, respectively; (D) magnified fingerprint images of (1) bifurcation, (2) island, (3) termination, (4) eye, (5) core, (6) ridge divergence, (7) crossover and (8) scar; (E) first one is the confocal red fluorescence image of starch embedded carbon dot dipped fingerprints on a glass sheet and second one is the same image after several weeks, reprinted with permission from ref. 500, Copyright 2020, American Chemical Society; (F) first, the "SC" & "AU" pattern photograph made with the ink of NaYF4:Yb,Er embedded carbon dots and only NaYF4:Yb,Er under the 365 nm UV excitation wavelength with a 550 nm cut-off filter; second one is the same logo under the 980 nm laser excitation wavelength with a 550 nm cut-off filter; third one is the same logo under 360 nm UV & 980 laser nm excitation with a 550 nm cut-off filter for dual mode anticounterfeiting; (G) first, the graphic security pattern photographs made with NaYF4:Yb,Er ink and NaYF4:Yb,Er embedded carbon dot ink under 365 nm UV and 980 nm laser excitation respectively, for dual mode anticounterfeiting, reprinted with permission from ref. 504, Copyright 2022, Royal Society of Chemistry.

applications.[503] Wei *et al.* achieved a red emissive hybrid nanocomposite by mixing NaYF4:Yb,Er with carbon dots *via* an electrostatic reaction for 30 s. This hybrid nanocomposite is used in advanced dual-mode anticounterfeiting applications. For the anticounterfeiting experiment, first, they prepared two types of ink made of NaYF4:Yb,Er (ink-1) and NaYF4:Yb,Er embedded carbon dots (ink-2), respectively. After that, they wrote two symbols "SC" with ink-2 and "AU" with ink-1, on a paper, respectively. When these written symbols are excited with 365 nm UV, a 980 nm laser and 365 nm UV with a 980 nm laser simultaneously, they show dual mode excitation characteristics. The images obtained through a 550 nm cut-off filter is highly applicable for anticounterfeiting application, Fig. 23(F). With addition, some symbols for graphitic security made of ink-1 and ink-2 showed dual mode anticounterfeiting, Fig. 23(G).[504]

5.4.2. Artificial photosynthesis. Artificial photosynthesis is a chemical reaction process that replicates the biological process of photosynthesis to produce adenosine triphosphate (ATP) and biomass. This is an economical and sustainable technology for producing, conserving, and transporting energy.[505–507] This technology can produce green hydrogen, oxygen and hydrocarbons. This process reduces carbon dioxide by absorbing and utilizing it in the reaction process.[508,509] It is discovered that artificial photosynthesis systems can be more efficient than natural photosynthesis.[510] Photosynthesis is the most essential metabolic process of living beings and must take place for the development of plants in this universe. This process including the absorption of energy of light, transfer of electrons, photophosphorylation and the digestion of carbon takes place in the chloroplast.[511] One of the most effective ways to boost plant development is increasing the efficiency of photosynthesis and the electron transfer mechanism. Environmental modeling, gene regulation, genetic improvement, decreasing photorespiration, optimization of Calvin Benson cycle/Rubisco and transforming C3 crops to the C4 pathway are the different mechanism strategies adopted to enhance the photosynthesis process in plants. Photosynthesis mainly takes place at the thylakoid or bacterial membranes of chloroplasts. It acts as a reaction centre and antenna complex. Depending on their absorption wavelengths, the photosystems are divided into two categories. Photosystem I (PS I) adsorbs far-red light photons at a longer wavelength of 700 nm and photosystem II (PS II) absorbs red light photons at a shorter wavelength of 680 nm. The splitting of water and the production of oxygen occur at PS II. So, it is called the oxygen-evolving photosystem and the reaction is called the Hill reaction. When chloroplast is exposed to both far-red (>690 nm) and red (<690 nm) light, the efficiency of photosynthesis increases. It is called the Emerson effect. The energy stimulates the synthesis of adenosine triphosphate (ATP) and nicotinamide adenine dinucleotide phosphate (NADPH) *via* a variety of energy conversions and electron conduction processes. ATP and NADPH change carbon dioxide to sugar molecules *via* a chain of enzymatic reactions in the Calvin cycle. The chloroplast contains a green pigment called chlorophyll. The chlorophyll has a reduced porphyrin ring system (chlorin system) that absorbs energy from the sun and transfers its energy via an electronic transition to the chemical reactions that occur in chloroplasts. This results in the generation of ATP that is transformed into chemically active energy to regulate carbon dioxide and water for producing nutrient biomass carbohydrates. The absorption regions are divided into two parts. The red region is associated with a wavelength of 640–660 nm and the blue region is associated with a wavelength of 430–450 nm. Chlorophyll only absorbs the visible wavelength range (400–700 nm) of the sun. Only 45% of the whole spectrum is visible in the sunlight, due to the light reflection, respiration, light inhibition and light saturation processes. Hence the efficiency of photosynthesis is 11% approximately. Green plants are the foundation of the food cycle because they produce their own food using the photosynthesis process. Therefore, creating artificial photosynthesis technology is a very encouraging way to boost photosynthesis, which satisfies the global need for food.[510,512–515]

FCNMs have caught the attention for improving solar energy harvesting and boosting the efficient operation of photosynthesis due to their biocompatibility, photobleaching, easy synthesis method and low cytotoxic nature. Engineering FCNMs with plants will follow the light conversion to energy and supply this energy to the chloroplast for accelerating the electron conduction mechanism followed by boosting the photosynthesis in the plant.[516–519]

Li *et al.* proposed a technology for utilizing sunlight by plants by developing a hybrid photosynthetic system. They used hydrophilic, biocompatible and high quantum yield-based far-red carbon dots as a light-harvesting agent and converter. When the carbon dots are excited by ultraviolet rays, they emit 625–800 nm far-red radiation which is utilized and absorbed by the chloroplasts and as a result Emerson effect starts to occur. The team showed that their demonstrated hybrid system leads to enhancing the electron transfer mechanism, production of ATP and gathering of biomass followed by an increase in the efficiency of photosynthesis. The proposed mechanism of this experiment is illustrated below, in Fig. 24. The fluorescence images of chloroplasts, far-red CD and far-red CD assisted chloroplast complexes were taken respectively under UV light excitation, Fig. 25(e). When the illuminated UV light from the sun or an artificial source is absorbed by the red carbon dot accumulated chloroplast hybrid system, the carbon dots convert the UV light to far-red radiation. It increases the electron transfer mechanism, and consequently, the photosynthesis efficiency of plants gradually increased. The electron transfer chain consists of four stages including photosystems I & II (PS I & II), the cytochrome b_6f complex (Cyt b_6f), and ATP synthase. The two pigments of thylakoid membranes are the reaction center pigments that are responsible for converting harvesting light into electricity and the second one is antenna pigments (AP1 and AP2) that are transferring light energy. The primary electron donor (P_{680}) of the reaction center pigment in PS II absorbs the emitted fluorescent radiation. The antenna pigments transfer the radiation to excite the P_{680} donor and produce electrons. The hole containing P_{680} leads to splitting of water into protons and oxygen. The black arrow shows the transfer of electrons from PS II to the Cyt b_6f complex followed by the route of pheophytin (Pheo) and plastoquinone (PQ). The

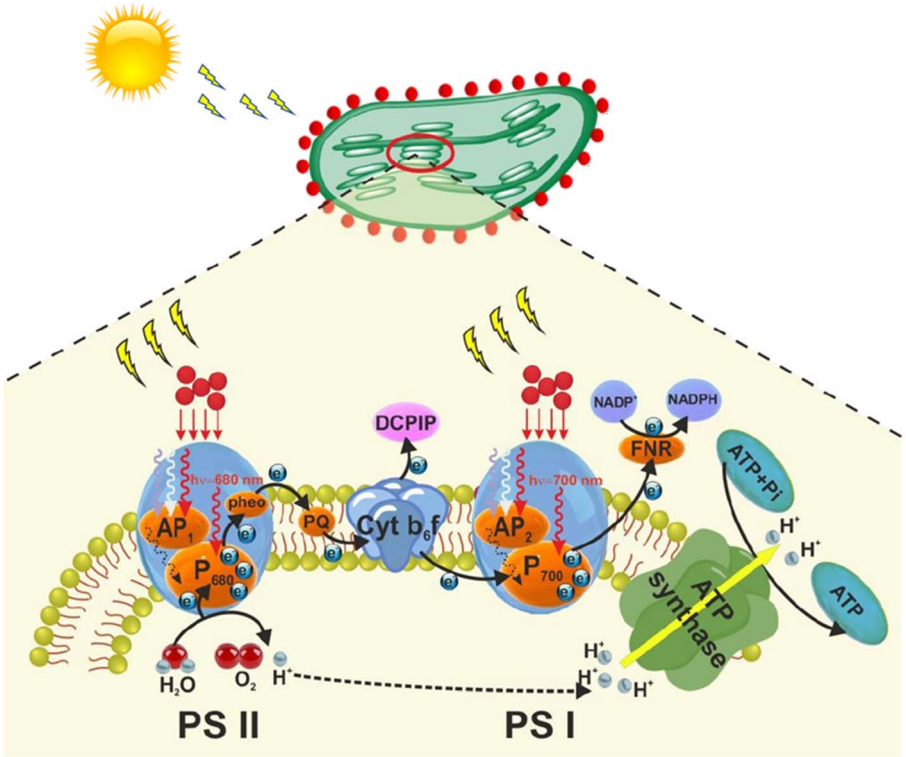

Fig. 24 Mechanism representation of the photosynthesis activity of the far-red carbon dots based chloroplast hybrid system: PS II & I are the photosystems I and II; AP1 and AP2 are the antenna pigments; P_{680} & P_{700} are the primary electron donor of PS II and PS I respectively; "Pheo" is pheophytin; PQ is plastoquinone; Cyt b_6f is the cytochrome b_6f complex; DCPIP is 2,6-dichlorophenolindophenol; FNR is ferredoxin reductase; $NADP^+$ and NADPH are nicotinamide adenine dinucleotide phosphate and its reduced form respectively; ATP synthase is adenosine triphosphate synthase; ATP + Pi is adenosine triphosphate with inorganic phosphate. Reprinted with permission from ref. 520, Copyright 2020, American Chemical Society.

primary electron donor (P_{700}) of the reaction center pigments in PS I excited and lost electrons. They extend to a steady state by gaining electrons from PQ. The ultimate acceptor nicotinamide adenine dinucleotide phosphate ($NADP^+$) is changed to reduced nicotinamide adenine dinucleotide phosphate (NADPH) by accepting electrons. Due to high electron affinity for electrons 2,6-dichlorophenolindophenol (DCPIP) captures the transported electrons from PS II to PS I, following the Hill reaction causing the splitting of water. The splitting of water generates protons and oxygen. The protons can produce energy for ATP formation by transportation *via* ATP synthase due to the concentration gradient. The growth of Rome lettuce was affected by far-red CDs at various concentrations (0, 1, 3, 5, and 7 g mL^{-1}), Fig. 25(d). The far-red CD treated confocal images of the root, stem and leaf of lettuce at a concentration of 10 μg per mL were also collected under excitation of 405 nm and the emission range of 630–700 nm, on a 200 μm scale bar, Fig. 25(c).[520]

Xu *et al.* reported red emissive NaYF4:Yb,Er doped carbon dots which are used to increase the water absorption capacity and promote the growth of hydroponic mung beans. The ability of these as-synthesized carbon dots to convert near-infrared radiation into red light helps in the boosting of photosynthesis by more than two times to promote the mung bean plant growth, Fig. 25(b).[521] Wang *et al.* demonstrated NIR emissive carbon dots for improving the absorption and the electron transfer mechanism to increase the photosynthesis efficiency of *N. benthamiana* plants. The team identified that the PsbP and PsiK genes were the controllers of photosynthesis in *N. benthamiana* plant.[522] Xiao *et al.* first developed aggregation-induced emission carbon dots derived from natural quercetin and coated with a chloroplast to develop a new type of biobased optical hybrid material for artificial photosynthesis. This hybrid material can increase the photosynthesis rate by regulating the harvesting of light over a wide spectral range, Fig. 25(a).[523]

5.4.3. Fluorescent silk. A focus of cutting-edge material research is fluorescent silk materials due to their potential for use in brilliant fabrics for wonderful dresses, tissue scaffolding, luminescent marks, surgical suturing, bioassay systems and drug delivery devices.[524,525] Red FCNMs have superior mechanical qualities, light durability, higher luminosity and low cytotoxicity than fluorescent organic dyes, rare earth nanoparticles, and semiconductor QDs, making them the best choice for feeding silkworms to produce fluorescent silk. The illuminating fluorescent silks have been used in regular clothing like suits and ties for making them gorgeous under light illumination. *Bombyx mori* silk is among the most prevalent examples of luminous silk. It is derived from the *Bombyx mori* silk fibroin which is a biopolymer that can be used to make materials with appealing characteristics of biocompatibility and

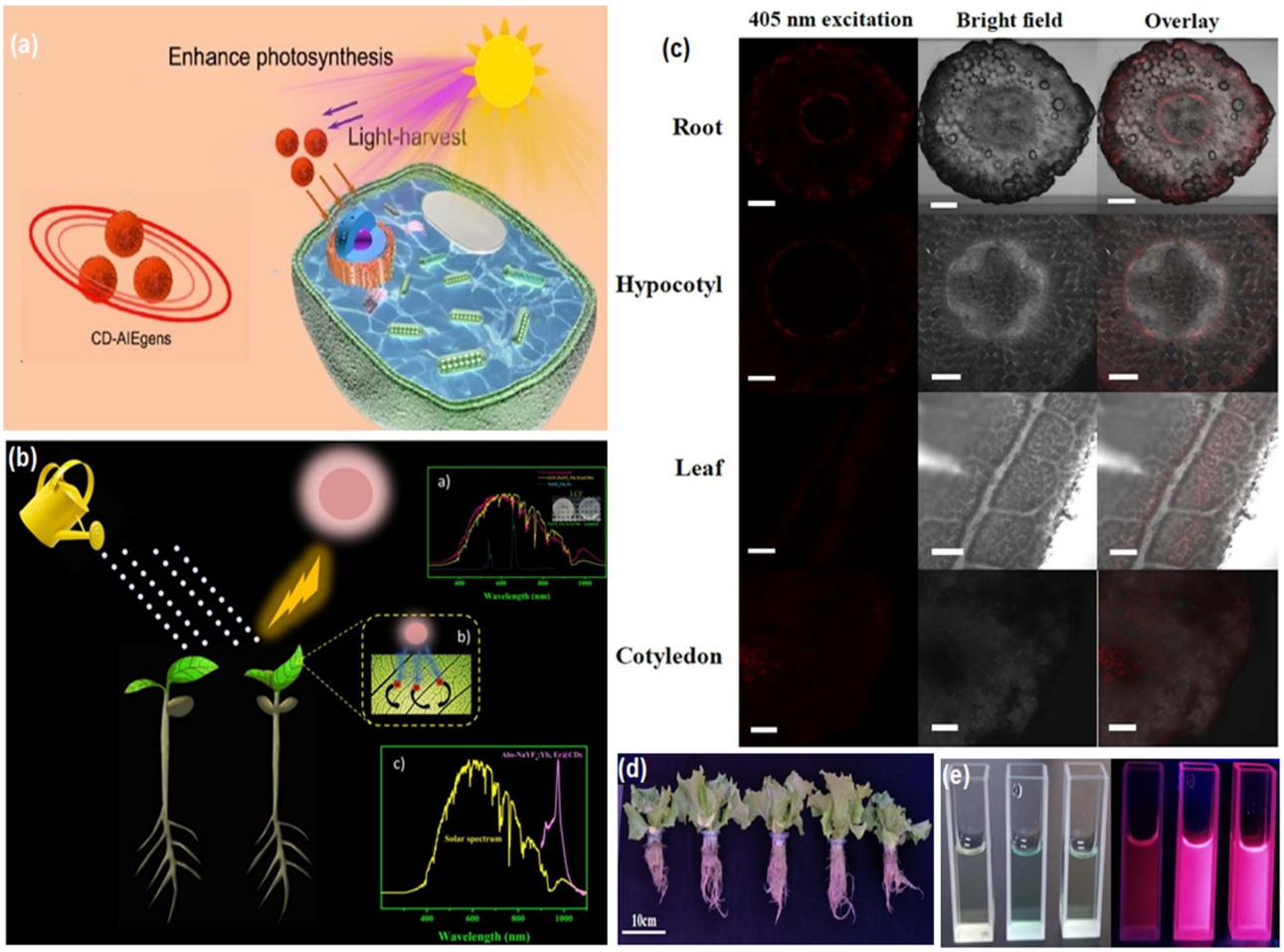

Fig. 25 (a) Representation of the aggregation-induced emission carbon dot assisted photosynthesis enhancement; reprinted with permission from ref. 523, Copyright 2021, American Chemical Society (b) schematic representation diagram of the red CD assisted light conversion effect under sunlight on mung bean seedlings; reprinted with permission from ref. 521, Copyright 2020, American Chemical Society; (c) far-red CD treated confocal images of the root, stem and leaf of lettuce at a concentration of 10 μg per mL, collected under excitation of 405 nm and the emission range of 630–700 nm, on a 200 μm scale bar; reprinted with permission from ref. 520, Copyright 2020, American Chemical Society (d) far-red CD effect at different concentrations (0, 1, 3, 5, and 7 μg mL^{-1}) on the growth of Rome lettuce; reprinted with permission from ref. 520, Copyright 2020, American Chemical Society; (e) the fluorescence images of chloroplasts, far-red CD and far-red CD assisted chloroplast complexes, respectively, reprinted with permission from ref. 520, Copyright 2020, American Chemical Society.

biodegradability. The creation of fluorescent silk using fluorescent carbon nanoparticles is extremely challenging, and a plausible mechanism is illustrated below. At first, the chains to break upon stretching are easily moveable chains in random coil/-helix shapes. The FCNMs moved with protein chains due to their spherical form, nanoscale size scale, and robust hydrogen bond couplings which in turn created more place for chains to migrate. This cooperative movement granted more elongation to the modified silk fibers. When the deformity was enhanced, comparatively the poor hydrogen bonding connections between FCNMs and silk fibroin were split first, releasing energy. Additionally, owing to the nanofiller influence, the FCNMs themselves produced hardness and caused a transfer of tension from the silk to the FCNMs.[526–532]

Liu *et al.* synthesized biocompatible and hydrophobic bright red fluorescent carbon dots (CDs) from mulberry leaves *via* a simple solvothermal route. The as-synthesized carbon dots showed a full width at half maximum emission curve peak at the 676 nm wavelength with a high quantum yield of 73%. The team fed the red carbon dots to silkworms and when the silkworms consumed enough red CDs, they grew up gradually. They took various photographs of an adult silkworm under UV light, Fig. 26(f) and under green light. The fluorescence microscopy images of the head and chest of the silkworm were taken under green excitation light, Fig. 26(e). The source of the luminescence was determined by the ethanolic extraction technique. The cocoon coatings and shells were dissolved in ethanol and then filtered to develop the ethanoic solution. The ethanoic solution was taken to get the fluorescent emission spectra under different excitation wavelengths, are shown Fig. 26(j). The anatomy of the control silkworm showed that the alimentary tract appears green in natural light and faintly fluoresces yellow-green when exposed to UV light, Fig. 26(c) and (g), top. In comparison, the alimentary tract of the examined group (red

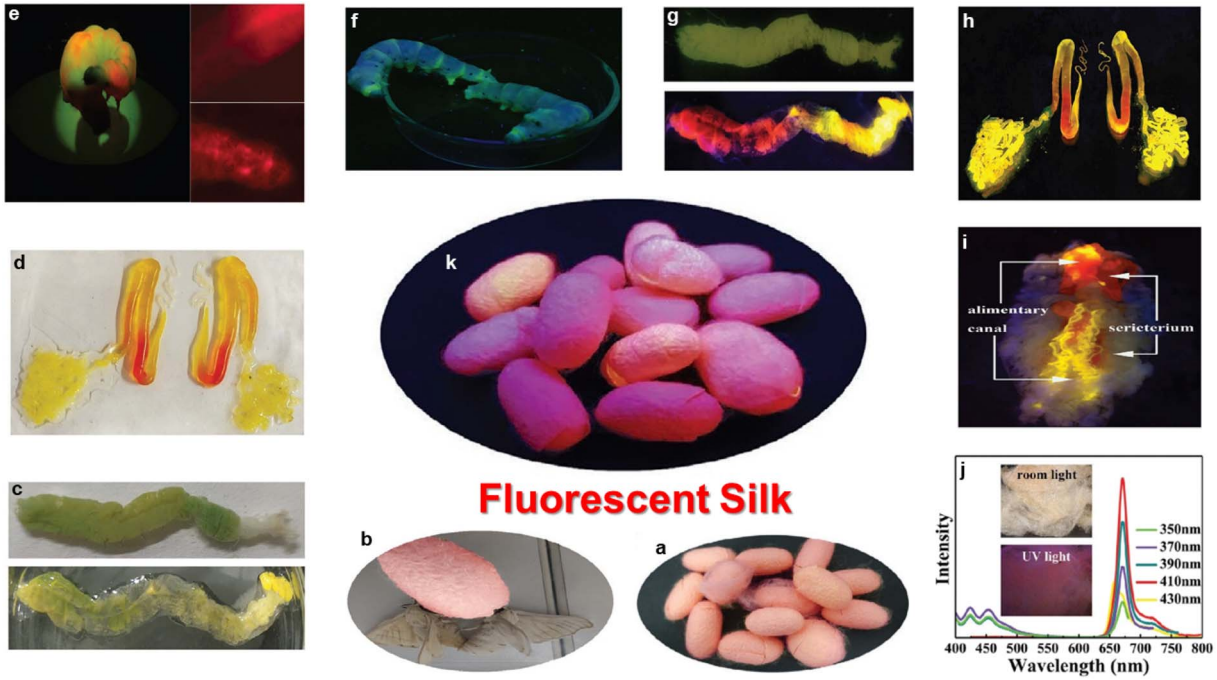

Fig. 26 Schematic representation of fluorescent silk – (a) & (k) fluorescent cocoon under daylight & UV light, respectively; (b) adult silkworm moth emerging from the bottom of the cocoon; (c) the alimentary canal of the control and test groups from up to down, respectively; (d) the photograph of silk glands under daylight; (e) photograph of an adult silkworm and the fluorescent microscopy images of the head and chest of the silkworm, under green excitation light; (f) the photograph of adult silkworms under UV light; (g) the alimentary canal of the control and test groups from up to down under UV light, respectively; (h) the photograph of silk glands under UV light; (i) the full anatomical photograph of the silkworm under UV light; (j) the fluorescent emission spectra of ethanoic solution taken out from the cocoon coats and shells, under different excitation wavelengths. Reprinted with permission from ref. 533, Copyright 2022, Wiley-VCH GmbH.

CDs) appears greyish-yellow in natural light and fluoresces reddish-yellow, when exposed to UV light, Fig. 26(c) and (g), bottom. The photograph of silk glands was also taken under daylight and UV light to confirm the diffusion of red CDs, Fig. 26(d) and (h). After a certain time, the silkworm constructed a cocoon made of fluorescent silk fibers and inside the cocoon, it changed into a pupa. After many days, the pupa changed into an adult silkworm moth and came out through a saliva-soaked aperture at the bottom of the cocoon. The day light & fluorescence images of the cocoon and adult silkworm moth were taken, respectively, Fig. 26(a), (b) and (k). These researchers showed that these cocoons showed vivid pink-red fluorescence under UV light, Fig. 26(k), and used for the production of fluorescent silk.[533]

Maltseva *et al.* developed a fluorescent silk fiber material from the *in situ* modification of spider silk and fluorescent carbon dots. The resulting hybrid materials showed intense red fluorescence with an emission wavelength of 590 nm when excited with a 480 nm wavelength. They utilized the developed materials for the closure of wounds and the detection of pathogens.[534]

5.4.4. Fluorescent nano-thermometers. The measurement of temperature at the nanoscale level requires a sophisticated research plan and study. Temperature sensing at the intracellular level is crucial for the explanation of several biological mechanisms.[535,536] Nanothermometers are next-generation sensing probes for intracellular thermal sensing and imaging with temperature-dependent fluorescent properties in the future. Thermal monitoring on the nanoscale demands fluorescent nanothermometers with strong biocompatibility and great thermal sensitivity to get sub-micrometric and sub-degree spatial and thermal characteristic results respectively. This sophisticated device determines temperature by taking advantage of the temperature-sensitive properties of fluorescence of nanomaterials including fluorescence lifetime, intensity and the highest emission peak.[537–541] Red emitting CNMs are emerging as nanothermometers due to their biocompatibility, low cost, broad absorption–emission region and high penetration characteristics.[542,543] Xu *et al.* reported a fluorescent-based nanothermometer for intercellular temperature identification derived from red-emitting carbon nanomaterials. Stable, hydrophilic, uniform-sized carbon dots are prepared from thionine and citric acid *via* a solvothermal approach. They explored the relative fluorescent intensities of red carbon dot solution as a function of increasing temperature ranging from 4–80 °C to confirm the change of the subcellular temperature sensing at a 500 nm excitation wavelength, Fig. 27(a). They also illustrated a hypothetical red carbon dot integrated thermometer representation with relative intensity as a function of temperature, Fig. 27(f). They confirmed that the red-emitting carbon dots possess superior temperature-responsive fluorescence properties for six cycles of the heating and cooling process with a temperature range

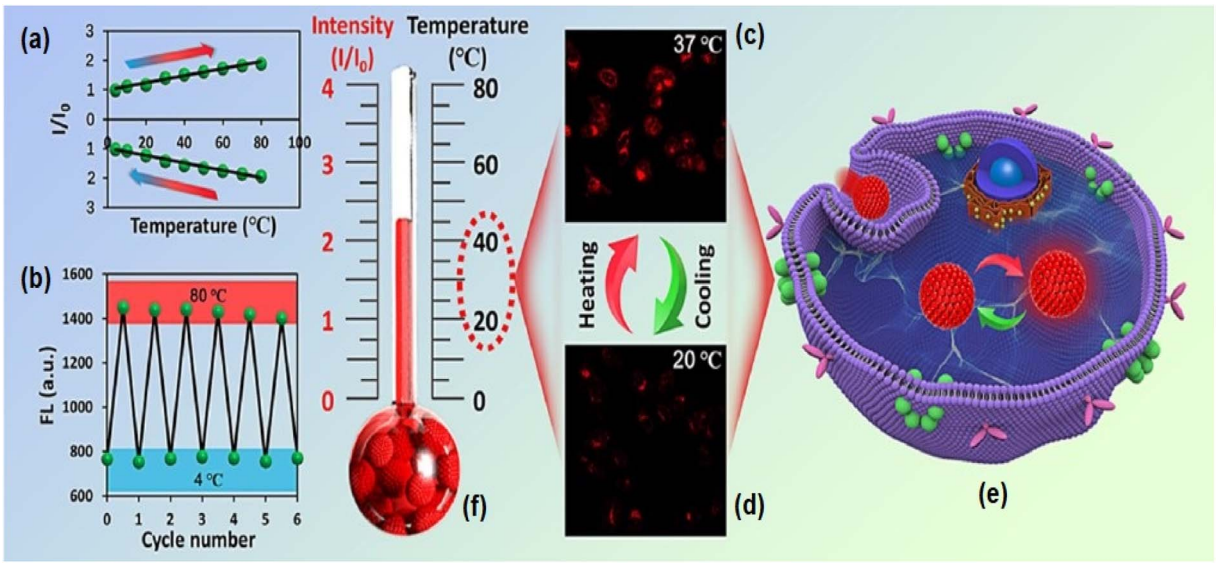

Fig. 27 Schematic representation of a fluorescent nanothermometer: (a) graph of the relative fluorescence intensity of the red fluorescent carbon dot solution *vs.* varying temperatures during the heating and cooling processes; (b) graph of the fluorescence intensity of red carbon dots in six cycles of heating and cooling at temperatures ranging from 4–80 °C using a 500 nm excitation wavelength; (c) & (d) the confocal fluorescence images of cells after being embedded with red carbon dots at the temperatures of 20 °C and 37 °C, respectively on a 100 μm scale bar; (e) microscopic intercellular representation of the cell with the red carbon dot injection and heating-cooling effect; (f) red carbon dot integrated thermometer representation with relative intensity and temperature (°C) scaling, reprinted with permission from ref. 544, Copyright 2020, American Chemical Society.

of 4–80 °C, Fig. 27(b). They also verified the temperature-responsive fluorescence properties of red carbon dots after embedding them with different kinds of cells and capturing the images of the cells with heating and cooling at the temperatures of 20 °C and 37 °C with heating and cooling, Fig. 27(c) and (d). A microscopic intercellular representation of red carbon dot injected cells with the heating-cooling effect was also illustrated, Fig. 27(e).[544]

Wang *et al.* developed red fluorescent carbon dots, derived from *o*-phenylenediamine, employed as a nanothermometer for controlling very accurately and sensitively the intracellular temperature value. The team examined the fluorescent emission spectra of red carbon dots in an aqueous solution as a function of varying temperatures of 15–60 °C. The red carbon dots were used as a probe for the indication of temperature. A gradual increase in the fluorescence intensity of the red carbon dots was noticed with rising the temperature from 15 °C to 60 °C. A sharp increase in the fluorescence intensity was observed at 60 °C.[545] Lee *et al.* prepared graphene quantum dots with emission in both visible and infrared regions for microscopic intercellular temperature identification as a function of fluorescence intensity.[546] Wang *et al.* produced microwave-assisted red-emitting carbon dots for measuring the temperature inside a living cell.[547]

6. Conclusion

Red emissive CNMs are the most predominant nanomaterials compared to others due to their several advantages such as a high penetration depth, wide absorption, biodegradability, and the photobleaching resistance effect. Hence, these red emissive CNMs are mostly useful in the fields of biomedical, anticounterfeiting and energy-related applications. Based on the above advantage and wide range of applications, we have outlined the fascinating aspects and ongoing research on red emissive CNMs. It should be noted that the scientific community has made significant efforts to date for the advancement of red-emissive CNM technologies. In this review, we have discussed the synthesis of FCNMs, the origin of fluorescence mechanisms, factors affecting the synthetic procedure for achieving tuneable emission properties, and applications in various current fields. This review summarized each aspect of red emissive CNMs to promote future research in the context of their synthesis, innovation, and exploring their additional applications.

7. Future prospects

In addition to synthetic strategies for developing a variety of red-emissive CNM samples, several factors for red-shifting fluorescence and the applications of FCNMs have also been demonstrated in this journey. However, further research and advancements are still needed to broaden the uses of red emission fluorescence. The followings are the present issues and prospective directions:

(1) The preparation of red emissive CNMs ought to be economical, scalable, reproducible, and environmentally friendly. However, in the majority of recent reports the preparation of red-emitting CNMs is costly, requires harmful chemical reagents, is time taking, and involves ineffective purification techniques, which limit their practical applicability. Hence, cost-effective carbon precursors and quick

purification techniques are the way for the development of large-scale and environmentally friendly red FCNMs in the coming years.

(2) The majority of red-emissive CNMs have low quantum yield, and therefore it is essential to develop a new method that increases the quantum yield of red-emissive CNMs in an aqueous medium.

(3) The origin of red fluorescence in carbon nanomaterials can be understood or explored in detail by sophisticated techniques such as lifetime microscopy, scanning tunneling microscopy, single-particle imaging, and related super-resolution techniques. Efficient machine learning techniques and computational modeling are also extremely desirable to reveal the red emission in FCNMs.

(4) The synthesis of far infrared emissive FCNMs with high quantum yield has been high in demand in recent times due to their excellent applications in the biomedical field. The researchers may select the best precursors, synthesis techniques and functionalization of ligands to prepare highly intense infrared emissive CNMs.

(5) The biodistribution, pharmacokinetics, and clearance studies of red emissive CNMs are required for further research to improve their clinical usage.

With the aforementioned initiatives, it is anticipated that the production of red emissive CNMs would increase their biomedical as well as energy-related applications. These low cytotoxic red FCNMs will also open up new avenues to meet the demands of clinical applications.

Author contributions

Conceptualization, methodology, and writing original draft: Tuhin Mandal; writing-review and editing: Shiv Rag Mishra; conceptualization, methodology, supervision, writing original draft and funding acquisition: Vikram Singh.

Conflicts of interest

The authors declare that they have no conflicts of interest.

Acknowledgements

This work is financially supported by the CSIR-Central Institute of Mining and Fuel Research Dhanbad (Project No. MLP-155/2021-2022).

References

1 B. Wang and S. Lu, *Matter*, 2022, **5**, 110–149.
2 Y. Wang, Y. Zhu, S. Yu and C. Jiang, *RSC Adv.*, 2017, **7**, 40973–40989.
3 Y.-P. Sun, B. Zhou, Y. Lin, W. Wang, K. A. S. Fernando, P. Pathak, M. J. Meziani, B. A. Harruff, X. Wang, H. Wang, P. G. Luo, H. Yang, M. E. Kose, B. Chen, L. M. Veca and S.-Y. Xie, *J. Am. Chem. Soc.*, 2006, **128**, 7756–7757.
4 T. Mandal, S. R. Mishra, K. Singh, H. Agarwalla, R. E. Masto, M. Kumar and V. Singh, *J. Nanopart. Res.*, 2023, **25**, 125.
5 K. S. Rawat, V. Singh, C. P. Sharma, A. Vyas, P. Pandey, J. Singh, N. M. Gupta, M. Sachdev and A. Goel, *J. Imaging*, 2023, **9**, 19.
6 V. Singh, B. Gorbel, S. Chatterjee, P. Sen and V. Verma, *Mater. Lett.*, 2022, **309**, 131446.
7 D. Bharathi, R. H. Krishna, V. Singh, N. Kottam and B. Siddlingeshwar, *J. Lumin.*, 2017, **190**, 328–334.
8 T. Mandal, A. K. Ghosh, S. R. Mishra, S. K. Pandey and V. Singh, *Nanoscale Adv.*, 2023, **5**, 4269–4285.
9 H. Ding, J.-S. Wei, N. Zhong, Q.-Y. Gao and H.-M. Xiong, *Langmuir*, 2017, **33**, 12635–12642.
10 Y. Gao, Y. Jiao, W. Lu, Y. Liu, H. Han, X. Gong, M. Xian, S. Shuang and C. Dong, *J. Mater. Chem. B*, 2018, **6**, 6099–6107.
11 K. Holá, M. Sudolská, S. Kalytchuk, D. Nachtigallová, A. L. Rogach, M. Otyepka and R. Zbořil, *ACS Nano*, 2017, **11**, 12402–12410.
12 Q. Wu, S. Zhang, S. Li, Y. Yan, S. Yu, R. Zhao and L. Huang, *Nano Res.*, 2023, **16**, 1835–1845.
13 S. Zhu, Y. Song, X. Zhao, J. Shao, J. Zhang and B. Yang, *Nano Res.*, 2015, **8**, 355–381.
14 V. Georgakilas, J. A. Perman, J. Tucek and R. Zboril, *Chem. Rev.*, 2015, **115**, 4744–4822.
15 C. Lin, Y. Zhuang, W. Li, T.-L. Zhou and R.-J. Xie, *Nanoscale*, 2019, **11**, 6584–6590.
16 X. Xu, L. Mo, W. Li, Y. Li, B. Lei, X. Zhang, J. Zhuang, C. Hu and Y. Liu, *Chin. Chem. Lett.*, 2021, **32**, 3927–3930.
17 H. Ding, Y. Ji, J.-S. Wei, Q.-Y. Gao, Z.-Y. Zhou and H.-M. Xiong, *J. Mater. Chem. B*, 2017, **5**, 5272–5277.
18 M. K. Kumawat, M. Thakur, R. B. Gurung and R. Srivastava, *ACS Sustain. Chem. Eng.*, 2017, **5**, 1382–1391.
19 S. Sun, L. Zhang, K. Jiang, A. Wu and H. Lin, *Chem. Mater.*, 2016, **28**, 8659–8668.
20 Q. Han, W. Xu, C. Ji, G. Xiong, C. Shi, D. Zhang, W. Shi, Y. Jiang and Z. Peng, *ACS Appl. Nano Mater.*, 2022, **5**, 15914–15924.
21 Y. Shi, W. Su, F. Yuan, T. Yuan, X. Song, Y. Han, S. Wei, Y. Zhang, Y. Li, X. Li and L. Fan, *Adv. Mater.*, 2023, 2210699.
22 Y. Wang, J. Zheng, J. Wang, Y. Yang and X. Liu, *Opt. Mater.*, 2017, **73**, 319–329.
23 Z. Wang, N. Jiang, M. Liu, R. Zhang, F. Huang and D. Chen, *Small*, 2021, **17**, 2104551.
24 Y. Zhang, J. Xiao, P. Zhuo, H. Yin, Y. Fan, X. Liu and Z. Chen, *ACS Appl. Mater. Interfaces*, 2019, **11**, 46054–46061.
25 X. Shi, H. Meng, Y. Sun, L. Qu, Y. Lin, Z. Li and D. Du, *Small*, 2019, **15**, 1901507.
26 F. Yan, Z. Sun, H. Zhang, X. Sun, Y. Jiang and Z. Bai, *Microchim. Acta*, 2019, **186**, 583.
27 A. Kubacka, U. Caudillo-Flores, I. Barba-Nieto and M. Fernández-García, *Appl. Catal., A*, 2021, **610**, 117966.
28 M. Gaft, R. Reisfeld and G. Panczer, *Modern Luminescence Spectroscopy of Minerals and Materials*, Springer, 2015.
29 K.-W. Chu, S. L. Lee, C.-J. Chang and L. Liu, *Polymers*, 2019, **11**, 689.
30 H. Ding, X.-X. Zhou, J.-S. Wei, X.-B. Li, B.-T. Qin, X.-B. Chen and H.-M. Xiong, *Carbon*, 2020, **167**, 322–344.

31 W. Yang, X. Li, L. Fei, W. Liu, X. Liu, H. Xu and Y. Liu, *Green Chem.*, 2022, **24**, 675–700.
32 S. Dutta Choudhury, in *Handbook on Synthesis Strategies for Advanced Materials: Volume-III: Materials Specific Synthesis Strategies*, ed. A. K. Tyagi and R. S. Ningthoujam, Springer Singapore, Singapore, 2021, pp. 421–460, DOI: 10.1007/978-981-16-1892-5_11.
33 M. Esmaeili, Z. Wu, D. Chen, A. Singh, P. Sonar, D. Thiel and Q. Li, *Adv. Powder Technol.*, 2022, **33**, 103560.
34 S. Tao, S. Zhu, T. Feng, C. Xia, Y. Song and B. Yang, *Mater. Today Chem.*, 2017, **6**, 13–25.
35 P. Yang, Z. Zhu, X. Li, T. Zhang, W. Zhang, M. Chen and X. Zhou, *J. Alloys Compd.*, 2020, **834**, 154399.
36 T. Dey, S. Mukherjee, A. Ghorai, S. Das and S. K. Ray, *Carbon*, 2018, **140**, 394–403.
37 Q. Fang, Y. Dong, Y. Chen, C.-H. Lu, Y. Chi, H.-H. Yang and T. Yu, *Carbon*, 2017, **118**, 319–326.
38 O. Kozák, M. Sudolská, G. Pramanik, P. Cígler, M. Otyepka and R. Zbořil, *Chem. Mater.*, 2016, **28**, 4085–4128.
39 K. Y. Zhang, Q. Yu, H. Wei, S. Liu, Q. Zhao and W. Huang, *Chem. Rev.*, 2018, **118**, 1770–1839.
40 S. Song, Z. Wang, C. Pan, Z. Li, J. Yan, Z. Lei, S. Ren, S. Kang and H. Shui, *J. Mater. Chem. C*, 2022, **10**, 10124–10131.
41 S. Hu, X. Meng, F. Tian, W. Yang, N. Li, C. Xue, J. Yang and Q. Chang, *J. Mater. Chem. C*, 2017, **5**, 9849–9853.
42 K. M. Tripathi, A. K. Sonker, S. K. Sonkar and S. Sarkar, *RSC Adv.*, 2014, **4**, 30100–30107.
43 X. Meng, Q. Chang, C. Xue, J. Yang and S. Hu, *Chem. Commun.*, 2017, **53**, 3074–3077.
44 H. Y. Ko, Y. W. Chang, G. Paramasivam, M. S. Jeong, S. Cho and S. Kim, *Chem. Commun.*, 2013, **49**, 10290–10292.
45 X. Tan, Y. Li, X. Li, S. Zhou, L. Fan and S. Yang, *Chem. Commun.*, 2015, **51**, 2544–2546.
46 L. Bao, C. Liu, Z.-L. Zhang and D.-W. Pang, *Adv. Mater.*, 2015, **27**, 1663–1667.
47 C.-C. Ke, Y.-C. Yang and W.-L. Tseng, *Part. Part. Syst. Charact.*, 2016, **33**, 132–139.
48 A. Sharma and J. Das, *J. Nanobiotechnol.*, 2019, **17**, 1–24.
49 D. Mijatovic, J. C. T. Eijkel and A. van den Berg, *Lab Chip*, 2005, **5**, 492–500.
50 D. Qu and Z. Sun, *Mater. Chem. Front.*, 2020, **4**, 400–420.
51 B. Wang, H. Song, Z. Tang, B. Yang and S. Lu, *Nano Res.*, 2022, **15**, 942–949.
52 M. M. Hussain, W. U. Khan, F. Ahmed, Y. Wei and H. Xiong, *Chem. Eng. J.*, 2023, **465**, 143010.
53 Y. Han, L. Liccardo, E. Moretti, H. Zhao and A. Vomiero, *J. Mater. Chem. C*, 2022, **10**, 11827–11847.
54 R. Vithalani, D. Patel, C. K. Modi and D. H. Suthar, *J. Mater. Sci.*, 2020, **55**, 8769–8792.
55 Y. Zhang, Y. Wang, X. Feng, F. Zhang, Y. Yang and X. Liu, *Appl. Surf. Sci.*, 2016, **387**, 1236–1246.
56 F. Yan, Y. Jiang, X. Sun, Z. Bai, Y. Zhang and X. Zhou, *Microchim. Acta*, 2018, **185**, 424.
57 W. Liu, C. Li, Y. Ren, X. Sun, W. Pan, Y. Li, J. Wang and W. Wang, *J. Mater. Chem. B*, 2016, **4**, 5772–5788.
58 W. Liang, P. Wang, M. J. Meziani, L. Ge, L. Yang, A. K. Patel, S. O. Morgan and Y.-P. Sun, *Nanoscale Adv.*, 2021, **3**, 4186–4195.
59 B. Zhi, X. Yao, M. Wu, A. Mensch, Y. Cui, J. Deng, J. J. Duchimaza-Heredia, K. J. Trerayapiwat, T. Niehaus, Y. Nishimoto, B. P. Frank, Y. Zhang, R. E. Lewis, E. A. Kappel, R. J. Hamers, H. D. Fairbrother, G. Orr, C. J. Murphy, Q. Cui and C. L. Haynes, *Chem. Sci.*, 2021, **12**, 2441–2455.
60 J. Schneider, C. J. Reckmeier, Y. Xiong, M. von Seckendorff, A. S. Susha, P. Kasák and A. L. Rogach, *J. Phys. Chem. C*, 2017, **121**, 2014–2022.
61 W. Ji, J. Yu, J. Cheng, L. Fu, Z. Zhang, B. Li, L. Chen and X. Wang, *ACS Appl. Nano Mater.*, 2022, **5**, 1656–1663.
62 B. Zhao, H. Ma, M. Zheng, K. Xu, C. Zou, S. Qu and Z. a. Tan, *Carbon Energy*, 2022, **4**, 88–114.
63 A. Ghaffarkhah, E. Hosseini, M. Kamkar, A. A. Sehat, S. Dordanihaghighi, A. Allahbakhsh, C. van der Kuur and M. Arjmand, *Small*, 2022, **18**, 2102683.
64 Y. Sun, H. Qin, X. Geng, R. Yang, L. Qu, A. N. Kani and Z. Li, *ACS Appl. Mater. Interfaces*, 2020, **12**, 31738–31744.
65 D. Li, Y. Qu, X. Zhang, W. Zheng, A. L. Rogach and S. Qu, *Chem. Eng. J.*, 2023, **454**, 140069.
66 D. Zhao, X. Liu, C. Wei, Y. Qu, X. Xiao and H. Cheng, *RSC Adv.*, 2019, **9**, 29533–29540.
67 X. Wei, D. Yang, L. Wang, Z. Wen, Z. Cui, L. Wang, H. He, W. Zhang, Z. Han, S. Mei, S. Qu and R. Guo, *Colloids Surf., B*, 2022, **220**, 112869.
68 T. Zhang, J. Zhu, Y. Zhai, H. Wang, X. Bai, B. Dong, H. Wang and H. Song, *Nanoscale*, 2017, **9**, 13042–13051.
69 E. V. Kundelev, N. V. Tepliakov, M. Y. Leonov, V. G. Maslov, A. V. Baranov, A. V. Fedorov, I. D. Rukhlenko and A. L. Rogach, *J. Phys. Chem. Lett.*, 2019, **10**, 5111–5116.
70 E. V. Kundelev, N. V. Tepliakov, M. Y. Leonov, V. G. Maslov, A. V. Baranov, A. V. Fedorov, I. D. Rukhlenko and A. L. Rogach, *J. Phys. Chem. Lett.*, 2020, **11**, 8121–8127.
71 M. Fu, F. Ehrat, Y. Wang, K. Z. Milowska, C. Reckmeier, A. L. Rogach, J. K. Stolarczyk, A. S. Urban and J. Feldmann, *Nano Lett.*, 2015, **15**, 6030–6035.
72 Y. Yan, J. Chen, N. Li, J. Tian, K. Li, J. Jiang, J. Liu, Q. Tian and P. Chen, *ACS Nano*, 2018, **12**, 3523–3532.
73 Z. Liu, X. Lu, M. Liu and W. Wang, *Molecules*, 2023, **28**, 2957.
74 F. Ehrat, S. Bhattacharyya, J. Schneider, A. Löf, R. Wyrwich, A. L. Rogach, J. K. Stolarczyk, A. S. Urban and J. Feldmann, *Nano Lett.*, 2017, **17**, 7710–7716.
75 S. Ghosh, A. Ghosh, G. Ghosh, K. Marjit and A. Patra, *J. Phys. Chem. Lett.*, 2021, **12**, 8080–8087.
76 S. Anwar, H. Ding, M. Xu, X. Hu, Z. Li, J. Wang, L. Liu, L. Jiang, D. Wang, C. Dong, M. Yan, Q. Wang and H. Bi, *ACS Appl. Bio Mater.*, 2019, **2**, 2317–2338.
77 P. Sengar, K. Chauhan and G. A. Hirata, *Transl. Oncol.*, 2022, **24**, 101482.
78 A. L. Abdelhady, M. I. Saidaminov, B. Murali, V. Adinolfi, O. Voznyy, K. Katsiev, E. Alarousu, R. Comin, I. Dursun, L. Sinatra, E. H. Sargent, O. F. Mohammed and O. M. Bakr, *J. Phys. Chem. Lett.*, 2016, **7**, 295–301.

79 P. Rani, R. Dalal, S. Srivastava and K. Tankeshwar, *Phys. Chem. Chem. Phys.*, 2022, **24**, 26232–26240.
80 R. Kumari, A. Kumar, N. K. Mishra and S. K. Sahu, *Langmuir*, 2022, **38**, 9389–9399.
81 L.-p. Li, X.-f. Ren, P.-r. Bai, Y. Liu, W.-y. Xu, J. Xie and R.-p. Zhang, *New Carbon Mater.*, 2021, **36**, 632–638.
82 K. Shao, L. Wang, Y. Wen, T. Wang, Y. Teng, Z. Shen and Z. Pan, *Anal. Chim. Acta*, 2019, **1068**, 52–59.
83 W.-B. Zhao, D.-D. Chen, K.-K. Liu, Y. Wang, R. Zhou, S.-Y. Song, F.-K. Li, L.-Z. Sui, Q. Lou, L. Hou and C.-X. Shan, *Chem. Eng. J.*, 2023, **452**, 139231.
84 C. Ji, Q. Han, Y. Zhou, J. Wu, W. Shi, L. Gao, R. M. Leblanc and Z. Peng, *Carbon*, 2022, **192**, 198–208.
85 X. Geng, Y. Sun, Z. Li, R. Yang, Y. Zhao, Y. Guo, J. Xu, F. Li, Y. Wang, S. Lu and L. Qu, *Small*, 2019, **15**, 1901517.
86 W. Wei, C. Xu, L. Wu, J. Wang, J. Ren and X. Qu, *Sci. Rep.*, 2014, **4**, 1–7.
87 X. Li, X. Yan, C. Wang, Y. Ma, Y. Jiang, R. Wang, D. Shi, Z. Li, G. Zhu and B. Tan, *Microchem. J.*, 2022, **183**, 108123.
88 L. Wang, B. Wang, E. Liu, Y. Zhao, B. He, C. Wang, G. Xing, Z. Tang, Y. Zhou and S. Qu, *Chin. Chem. Lett.*, 2022, **33**, 4111–4115.
89 X. Niu, T. Song and H. Xiong, *Chin. Chem. Lett.*, 2021, **32**, 1953–1956.
90 A. Demirbaş, *Energy Convers. Manage.*, 2001, **42**, 1357–1378.
91 M. Kaltschmitt, in *Energy from Organic Materials (Biomass): A Volume in the Encyclopedia of Sustainability Science and Technology*, ed. M. Kaltschmitt, Springer New York, New York, NY, 2nd edn, 2019, pp. 1–14, DOI: **10.1007/978-1-4939-7813-7_924**.
92 J. C. Serrano-Ruiz, *Molecules*, 2020, **25**, 5217.
93 D. Shen, R. Xiao, S. Gu and K. Luo, *RSC Adv.*, 2011, **1**, 1641–1660.
94 H. Wang, G. Gurau and R. D. Rogers, *Chem. Soc. Rev.*, 2012, **41**, 1519–1537.
95 G. Stork and S. Raucher, *J. Am. Chem. Soc.*, 1976, **98**, 1583–1584.
96 A. Blanco and G. Blanco, in *Medical Biochemistry*, ed. A. Blanco and G. Blanco, Academic Press, 2017, pp. 73–97, DOI: **10.1016/B978-0-12-803550-4.00004-5**.
97 H. Rao, W. Liu, K. He, S. Zhao, Z. Lu, S. Zhang, M. Sun, P. Zou, X. Wang, Q. Zhao, Y. Wang and T. Liu, *ACS Sustain. Chem. Eng.*, 2020, **8**, 8857–8867.
98 J. Wang, J. Wang, W. Xiao, Z. Geng, D. Tan, L. Wei, J. Li, L. Xue, X. Wang and J. Zhu, *Anal. Methods*, 2020, **12**, 3218–3224.
99 T. C. Wareing, P. Gentile and A. N. Phan, *ACS Nano*, 2021, **15**, 15471–15501.
100 S. Perumal, R. Atchudan, T. N. J. I. Edison and Y. R. Lee, *J. Environ. Chem. Eng.*, 2021, **9**, 105802.
101 C. Kang, Y. Huang, H. Yang, X. F. Yan and Z. P. Chen, *Nanomaterials*, 2020, **10**, 2316.
102 H. Liu, J. Ding, K. Zhang and L. Ding, *TrAC, Trends Anal. Chem.*, 2019, **118**, 315–337.
103 V. Singh, S. Chatterjee, M. Palecha, P. Sen, B. Ateeq and V. Verma, *Carbon Lett.*, 2021, **31**, 117–123.
104 V. Singh, K. S. Rawat, S. Mishra, T. Baghel, S. Fatima, A. A. John, N. Kalleti, D. Singh, A. Nazir, S. K. Rath and A. Goel, *J. Mater. Chem. B*, 2018, **6**, 3366–3371.
105 C. Zhang, Y. Xiao, Y. Ma, B. Li, Z. Liu, C. Lu, X. Liu, Y. Wei, Z. Zhu and Y. Zhang, *J. Photochem. Photobiol., B*, 2017, **174**, 315–322.
106 C. Liang, X. Xie, D. Zhang, J. Feng, S. Lu and Q. Shi, *J. Mater. Chem. B*, 2021, **9**, 5670–5681.
107 C. Tang, R. Long, X. Tong, Y. Guo, C. Tong and S. Shi, *Microchem. J.*, 2021, **164**, 106000.
108 D. Zhang, F. Zhang, S. Wang, S. Hu, Y. Liao, F. Wang and H. Liu, *Spectrochim. Acta, Part A*, 2023, **290**, 122285.
109 S. Wang, H. Zhao, J. Yang, Y. Dong, S. Guo, Q. Cheng, Y. Li and S. Liu, *ACS Omega*, 2023, **8**, 6550–6558.
110 M. Tariq, A. Singh, N. Varshney, S. K. Samanta and M. P. Sk, *Mater. Today Commun.*, 2022, **33**, 104347.
111 H. Yang, X. Su, L. Cai, Z. Sun, Y. Lin, J. Yu, L. Hao and C. Liu, *J. Environ. Chem. Eng.*, 2022, **10**, 108718.
112 W. Zhang, L. Li, M. Yan, J. Ma, J. Wang, C. Liu, Y. Bao, H. Jin and Q. Fan, *ACS Sustain. Chem. Eng.*, 2023, **11**, 5082–5092.
113 S. Hu, A. Trinchi, P. Atkin and I. Cole, *Angew. Chem., Int. Ed.*, 2015, **54**, 2970–2974.
114 D. Qu, M. Zheng, J. Li, Z. Xie and Z. Sun, *Light: Sci. Appl.*, 2015, **4**, e364.
115 A. Lv, Q. Chen, C. Zhao, S. Li, S. Sun, J. Dong, Z. Li and H. Lin, *Chin. Chem. Lett.*, 2021, **32**, 3653–3664.
116 Z. Tian, X. Zhang, D. Li, D. Zhou, P. Jing, D. Shen, S. Qu, R. Zboril and A. L. Rogach, *Adv. Opt. Mater.*, 2017, **5**, 1700416.
117 Y. Xian and K. Li, *Adv. Mater.*, 2022, **34**, 2201031.
118 D. Gao, X. Liu, D. Jiang, H. Zhao, Y. Zhu, X. Chen, H. Luo, H. Fan and X. Zhang, *Sens. Actuators, B*, 2018, **277**, 373–380.
119 J. Li and X. Gong, *Small*, 2022, **18**, 2205099.
120 L. Jiang, H. Ding, M. Xu, X. Hu, S. Li, M. Zhang, Q. Zhang, Q. Wang, S. Lu, Y. Tian and H. Bi, *Small*, 2020, **16**, 2000680.
121 Z. Sun, F. Yan, J. Xu, H. Zhang and L. Chen, *Nano Res.*, 2022, **15**, 414–422.
122 C. J. Reckmeier, Y. Wang, R. Zboril and A. L. Rogach, *J. Phys. Chem. C*, 2016, **120**, 10591–10604.
123 Y.-H. Chien, K. K. Chan, S. H. K. Yap and K.-T. Yong, *J. Chem. Technol. Biotechnol.*, 2018, **93**, 1519–1528.
124 M. Behi, L. Gholami, S. Naficy, S. Palomba and F. Dehghani, *Nanoscale Adv.*, 2022, **4**, 353–376.
125 S. Hill and M. C. Galan, *Beilstein J. Org. Chem.*, 2017, **13**, 675–693.
126 X. Li, S. Zhang, S. A. Kulinich, Y. Liu and H. Zeng, *Sci. Rep.*, 2014, **4**, 4976.
127 Q. Wang, H. Zheng, Y. Long, L. Zhang, M. Gao and W. Bai, *Carbon*, 2011, **49**, 3134–3140.
128 J.-I. Yoshida, *Chem. Rec.*, 2010, **10**, 332–341.
129 N. Papaioannou, M.-M. Titirici and A. Sapelkin, *ACS Omega*, 2019, **4**, 21658–21665.
130 S. Sri, R. Kumar, A. K. Panda and P. R. Solanki, *ACS Appl. Mater. Interfaces*, 2018, **10**, 37835–37845.
131 M. Sun, Y. Han, X. Yuan, P. Jing, L. Zhang, J. Zhao and Y. Zheng, *Nanoscale*, 2020, **12**, 15823–15831.

132 R. Dai, X. Chen, N. Ouyang and Y. Hu, *Chem. Eng. J.*, 2022, **431**, 134172.
133 S. Khan, A. Gupta, N. C. Verma and C. K. Nandi, *Nano Lett.*, 2015, **15**, 8300–8305.
134 A. O. da Silva, M. O. Rodrigues, M. H. Sousa and A. F. C. Campos, *Colloids Surf., A*, 2021, **621**, 126578.
135 K. Zhao, X. Zheng, H. Zhang, M. Xu, S. Wang, Q. Yang and C. Xiong, *J. Alloys Compd.*, 2019, **793**, 613–619.
136 L. Yang, S. Liu, T. Quan, Y. Tao, M. Tian, L. Wang, J. Wang, D. Wang and D. Gao, *J. Colloid Interface Sci.*, 2022, **612**, 650–663.
137 T. V. de Medeiros, J. Manioudakis, F. Noun, J.-R. Macairan, F. Victoria and R. Naccache, *J. Mater. Chem. C*, 2019, **7**, 7175–7195.
138 X. Sun and Y. Lei, *TrAC, Trends Anal. Chem.*, 2017, **89**, 163–180.
139 W. Meng, X. Bai, B. Wang, Z. Liu, S. Lu and B. Yang, *Energy Environ. Mater.*, 2019, **2**, 172–192.
140 O. Polat, S. G. Gizer, M. Sahiner and N. Sahiner, in *Functionalized Carbon Nanomaterials for Theranostic Applications*, ed. S. Mallakpour and C. M. Hussain, Elsevier, 2023, pp. 19–53, DOI: **10.1016/B978-0-12-824366-4.00012-1**.
141 R. Jelinek, in *Carbon Quantum Dots: Synthesis, Properties and Applications*, ed. R. Jelinek, Springer International Publishing, Cham, 2017, pp. 29–46, DOI: **10.1007/978-3-319-43911-2_3**.
142 Y. Choi, Y. Choi, O.-H. Kwon and B.-S. Kim, *Chem. – Asian J.*, 2018, **13**, 586–598.
143 Y. Ganjkhanlou, J. J. E. Maris, J. Koek, R. Riemersma, B. M. Weckhuysen and F. Meirer, *J. Phys. Chem. C*, 2022, **126**, 2720–2727.
144 V. Michaud, J. Pracht, F. Schilfarth, C. Damm, B. Platzer, P. Haines, C. Harreiß, D. M. Guldi, E. Spiecker and W. Peukert, *Nanoscale*, 2021, **13**, 13116–13128.
145 P. Bag, R. K. Maurya, A. Dadwal, M. Sarkar, P. A. Chawla, R. K. Narang and B. Kumar, *ChemistrySelect*, 2021, **6**, 2774–2789.
146 C. He, P. Xu, X. Zhang and W. Long, *Carbon*, 2022, **186**, 91–127.
147 S. Mallakpour and C. M. Hussain, *Environmental Applications of Carbon Nanomaterials-Based Devices*, Wiley Online Library, 2021.
148 A. A. Kokorina, A. V. Sapelkin, G. B. Sukhorukov and I. Y. Goryacheva, *Adv. Colloid Interface Sci.*, 2019, **274**, 102043.
149 J. B. Essner, J. A. Kist, L. Polo-Parada and G. A. Baker, *Chem. Mater.*, 2018, **30**, 1878–1887.
150 A. L. Himaja, P. S. Karthik and S. P. Singh, *Chem. Rec.*, 2015, **15**, 595–615.
151 A. L. Himaja, P. S. Karthik, B. Sreedhar and S. P. Singh, *J. Fluoresc.*, 2014, **24**, 1767–1773.
152 M. Irfan, M. Irfan, A. Idris, N. Baig, T. A. Saleh, R. Nasiri, Y. Iqbal, N. Muhammad, F. Rehman and H. Khalid, *J. Biomed. Mater. Res., Part A*, 2019, **107**, 513–525.
153 S. Paul, S. Hazra and A. Banerjee, *ACS Sustain. Chem. Eng.*, 2021, **9**, 12912–12921.
154 Y. Song, S. Zhu, S. Zhang, Y. Fu, L. Wang, X. Zhao and B. Yang, *J. Mater. Chem. C*, 2015, **3**, 5976–5984.
155 Y.-P. Sun, X. Wang, F. Lu, L. Cao, M. J. Meziani, P. G. Luo, L. Gu and L. M. Veca, *J. Phys. Chem. C*, 2008, **112**, 18295–18298.
156 P. Li, A. Kumar, J. Ma, Y. Kuang, L. Luo and X. Sun, *Sci. Bull.*, 2018, **63**, 645–662.
157 J. Chen, Z. Gong, W. Tang, K. H. Row and H. Qiu, *TrAC, Trends Anal. Chem.*, 2021, **134**, 116135.
158 F. de Andrés and Á. Ríos, *Microchem. J.*, 2021, **161**, 105773.
159 Y. Shen, M. Y. Gee and A. B. Greytak, *Chem. Commun.*, 2017, **53**, 827–841.
160 Z. Liu, F. Li, Y. Luo, M. Li, G. Hu, X. Pu, T. Tang, J. Wen, X. Li and W. Li, *Molecules*, 2021, **26**, 3922.
161 Y. Zhou, E. M. Zahran, B. A. Quiroga, J. Perez, K. J. Mintz, Z. Peng, P. Y. Liyanage, R. R. Pandey, C. C. Chusuei and R. M. Leblanc, *Appl. Catal., B*, 2019, **248**, 157–166.
162 A. M. P., S. Pardhiya and P. Rajamani, *Small*, 2022, **18**, 2105579.
163 S. Xiong, R. Tang, D. Gong, Y. Deng, J. Zheng, L. Li, Z. Zhou, L. Yang and L. Su, *Chin. J. Catal.*, 2022, **43**, 1719–1748.
164 Y. Park, J. Yoo, B. Lim, W. Kwon and S. W. Rhee, *J. Mater. Chem. A*, 2016, **4**, 11582–11603.
165 A. Loukanov, R. Sekiya, M. Yoshikawa, N. Kobayashi, Y. Moriyasu and S. Nakabayashi, *J. Phys. Chem. C*, 2016, **120**, 15867–15874.
166 L. Liu and Z. Xu, *Anal. Methods*, 2019, **11**, 760–766.
167 Z. Zhou, P. Tian, X. Liu, S. Mei, D. Zhou, D. Li, P. Jing, W. Zhang, R. Guo, S. Qu and A. L. Rogach, *Adv. Sci.*, 2018, **5**, 1800369.
168 S. Mukherjee, E. Prasad and A. Chadha, *Phys. Chem. Chem. Phys.*, 2017, **19**, 7288–7296.
169 C. M. Singaravelu, X. Deschanels, C. Rey and J. Causse, *ACS Appl. Nano Mater.*, 2021, **4**, 6386–6397.
170 S. Chernyak, A. Podgornova, S. Dorofeev, S. Maksimov, K. Maslakov, S. Savilov and V. Lunin, *Appl. Surf. Sci.*, 2020, **507**, 145027.
171 H. Tetsuka, A. Nagoya, T. Fukusumi and T. Matsui, *Adv. Mater.*, 2016, **28**, 4632–4638.
172 B. Zhang, B. Wang, E. V. Ushakova, B. He, G. Xing, Z. Tang, A. L. Rogach and S. Qu, *Small*, 2204158.
173 Y. Ma, X. Zhang, J. Bai, K. Huang and L. Ren, *Chem. Eng. J.*, 2019, **374**, 787–792.
174 F. Yan, Y. Jiang, X. Sun, J. Wei, L. Chen and Y. Zhang, *Nano Res.*, 2020, **13**, 52–60.
175 K. Jiang, S. Sun, L. Zhang, Y. Lu, A. Wu, C. Cai and H. Lin, *Angew. Chem., Int. Ed.*, 2015, **54**, 5360–5363.
176 B. Wang, J. Yu, L. Sui, S. Zhu, Z. Tang, B. Yang and S. Lu, *Adv. Sci.*, 2021, **8**, 2001453.
177 X. Yang, L. Ai, J. Yu, G. I. N. Waterhouse, L. Sui, J. Ding, B. Zhang, X. Yong and S. Lu, *Sci. Bull.*, 2022, **67**, 1450–1457.
178 B. Lyu, H.-J. Li, F. Xue, L. Sai, B. Gui, D. Qian, X. Wang and J. Yang, *Chem. Eng. J.*, 2020, **388**, 124285.
179 M. Zheng, L. Qiao, Y. Su, P. Gao and Z. Xie, *J. Mater. Chem. B*, 2019, **7**, 3840–3845.
180 H. Song, X. Liu, B. Wang, Z. Tang and S. Lu, *Sci. Bull.*, 2019, **64**, 1788–1794.

181 B.-P. Jiang, B. Zhou, X.-C. Shen, Y.-X. Yu, S.-C. Ji, C.-C. Wen and H. Liang, *Chem. –Eur. J.*, 2015, **21**, 18993–18999.
182 L. Li, R. Zhang, C. Lu, J. Sun, L. Wang, B. Qu, T. Li, Y. Liu and S. Li, *J. Mater. Chem. B*, 2017, **5**, 7328–7334.
183 H. Ding, X. Zhou, B. Qin, Z. Zhou and Y. Zhao, *J. Lumin.*, 2019, **211**, 298–304.
184 Y. Li, G. Bai, S. Zeng and J. Hao, *ACS Appl. Mater. Interfaces*, 2019, **11**, 4737–4744.
185 J. Liu, Y. Geng, D. Li, H. Yao, Z. Huo, Y. Li, K. Zhang, S. Zhu, H. Wei, W. Xu, J. Jiang and B. Yang, *Adv. Mater.*, 2020, **32**, 1906641.
186 A. Bhati, S. R. Anand, Gunture, A. K. Garg, P. Khare and S. K. Sonkar, *ACS Sustain. Chem. Eng.*, 2018, **6**, 9246–9256.
187 M. Zheng, Y. Li, S. Liu, W. Wang, Z. Xie and X. Jing, *ACS Appl. Mater. Interfaces*, 2016, **8**, 23533–23541.
188 S. Ghosh, H. Ali and N. R. Jana, *ACS Sustain. Chem. Eng.*, 2019, **7**, 12629–12637.
189 L. Pan, S. Sun, L. Zhang, K. Jiang and H. Lin, *Nanoscale*, 2016, **8**, 17350–17356.
190 R.-S. Juang, C.-T. Hsieh, C.-P. Kao, Y. A. Gandomi, C.-C. Fu, S.-H. Liu and S. Gu, *Carbon*, 2021, **176**, 61–70.
191 C. Dan, Z. Zhao, J. Feng, Y. Xin, Y. Yang and L. Shi, *Sens. Actuators, B*, 2021, **349**, 130774.
192 D. Song, J. Tian, W. Xu, H. Wen, C. Wang, J. Tang, J. Zhang and M. Guo, *Carbon*, 2021, **174**, 741–749.
193 D. P. Damera, V. Krishna, V. V. K. Venuganti and A. Nag, *J. Photochem. Photobiol., B*, 2021, **225**, 112335.
194 Y. Qu, X. Bai, D. Li, X. Zhang, C. Liang, W. Zheng and S. Qu, *J. Colloid Interface Sci.*, 2022, **613**, 547–553.
195 H. Li, Z. Wei, X. Zuo, H. Chen, C. Ren, Y. Dong and X. Chen, *Dyes Pigm.*, 2022, **206**, 110614.
196 M.-J. Fu, N. Wei, L.-F. Pang, X.-F. Guo and H. Wang, *Sens. Actuators, B*, 2022, **351**, 130939.
197 W. Wang, J. Wu, Y. Xing and Z. Wang, *Sens. Actuators, B*, 2022, **360**, 131645.
198 L. Cao, T. Zhu, M. Zan, Y. Liu, X. Xing, Q. Qian, Q. Mei, W.-F. Dong and L. Li, *Sens. Actuators, B*, 2022, **370**, 132424.
199 X. Li, Q. Hu, K. Yang, S. Zhao, S. Zhu, B. Wang, Y. Zhang, J. Yi, X. Song and M. Lan, *Sens. Actuators, B*, 2022, **371**, 132534.
200 W. Zhao, Y. Wang, K. Liu, R. Zhou and C. Shan, *Chin. Chem. Lett.*, 2022, **33**, 798–802.
201 L. Jin, Y. Shao, X. Chen, X. Wang, Q. Wang, Y. Wang, Y. Zhu, H. Yu, L. Han and F. Tian, *J. Photochem. Photobiol., A*, 2022, **425**, 113702.
202 Y. Jing, G. Liu, C. Zhang, B. Yu, J. Sun, D. Lin and J. Qu, *ACS Appl. Bio Mater.*, 2022, **5**, 1187–1193.
203 C. Xia, S. Zhu, T. Feng, M. Yang and B. Yang, *Adv. Sci.*, 2019, **6**, 1901316.
204 S. A. Shaik, S. Sengupta, R. S. Varma, M. B. Gawande and A. Goswami, *ACS Sustain. Chem. Eng.*, 2021, **9**, 3–49.
205 Z. Hallaji, Z. Bagheri, S.-O. Kalji, E. Ermis and B. Ranjbar, *FlatChem*, 2021, **29**, 100271.
206 S. K. Tammina, A. Khan and J.-W. Rhim, *Chemosphere*, 2023, **313**, 137433.
207 M. Dyksik, S. Wang, W. Paritmongkol, D. K. Maude, W. A. Tisdale, M. Baranowski and P. Plochocka, *J. Phys. Chem. Lett.*, 2021, **12**, 1638–1643.
208 D. Thureja, A. Imamoglu, T. Smoleński, I. Amelio, A. Popert, T. Chervy, X. Lu, S. Liu, K. Barmak, K. Watanabe, T. Taniguchi, D. J. Norris, M. Kroner and P. A. Murthy, *Nature*, 2022, **606**, 298–304.
209 N. N. Negulyaev, V. S. Stepanyuk, L. Niebergall, P. Bruno, W. Hergert, J. Repp, K. H. Rieder and G. Meyer, *Phys. Rev. Lett.*, 2008, **101**, 226601.
210 R. W. Kelsall, I. W. Hamley and M. Geoghegan, *Nanoscale Science and Technology*, 2005.
211 X. Li, Z. Lu and T. Wang, *Nano Res.*, 2021, **14**, 1233–1243.
212 J. Shamsi, A. S. Urban, M. Imran, L. De Trizio and L. Manna, *Chem. Rev.*, 2019, **119**, 3296–3348.
213 F. A. Permatasari, M. A. Irham, S. Z. Bisri and F. Iskandar, *Nanomaterials*, 2021, **11**, 91.
214 T. T. Tran, J. R. Panella, J. R. Chamorro, J. R. Morey and T. M. McQueen, *Mater. Horiz.*, 2017, **4**, 688–693.
215 M. S. Rudner and N. H. Lindner, *Nat. Rev. Phys.*, 2020, **2**, 229–244.
216 J. Even, L. Pedesseau, C. Katan, M. Kepenekian, J.-S. Lauret, D. Sapori and E. Deleporte, *J. Phys. Chem. C*, 2015, **119**, 10161–10177.
217 Y. E. Panfil, M. Oded and U. Banin, *Angew. Chem., Int. Ed.*, 2018, **57**, 4274–4295.
218 R. Negishi, M. Akabori, T. Ito, Y. Watanabe and Y. Kobayashi, *Sci. Rep.*, 2016, **6**, 1–10.
219 S. Winkler, P. Amsalem, J. Frisch, M. Oehzelt, G. Heimel and N. Koch, *Mater. Horiz.*, 2015, **2**, 427–433.
220 X. Wang, F. Wang, Y. Sang and H. Liu, *Adv. Energy Mater.*, 2017, **7**, 1700473.
221 S. Kanungo, G. Ahmad, P. Sahatiya, A. Mukhopadhyay and S. Chattopadhyay, *npj 2D Mater. Appl.*, 2022, **6**, 83.
222 J. Jin, N. Hu and H. Hu, *Int. J. Mech. Sci.*, 2022, **219**, 107100.
223 A. Chaves, J. G. Azadani, H. Alsalman, D. R. da Costa, R. Frisenda, A. J. Chaves, S. H. Song, Y. D. Kim, D. He, J. Zhou, A. Castellanos-Gomez, F. M. Peeters, Z. Liu, C. L. Hinkle, S.-H. Oh, P. D. Ye, S. J. Koester, Y. H. Lee, P. Avouris, X. Wang and T. Low, *npj 2D Mater. Appl.*, 2020, **4**, 29.
224 M. J. Molaei, *Talanta*, 2019, **196**, 456–478.
225 K. Barve, U. Singh, P. Yadav and D. Bhatia, *Mater. Chem. Front.*, 2023, **7**, 1781–1802.
226 H.-L. Yang, L.-F. Bai, Z.-R. Geng, H. Chen, L.-T. Xu, Y.-C. Xie, D.-J. Wang, H.-W. Gu and X.-M. Wang, *Mater. Today Adv.*, 2023, **18**, 100376.
227 K. Davis, R. Yarbrough, M. Froeschle, J. White and H. Rathnayake, *RSC Adv.*, 2019, **9**, 14638–14648.
228 Y. Yan, J. Gong, J. Chen, Z. Zeng, W. Huang, K. Pu, J. Liu and P. Chen, *Adv. Mater.*, 2019, **31**, 1808283.
229 Z.-G. Yu, *Phys. Chem. Chem. Phys.*, 2017, **19**, 14907–14912.
230 F. Murphy-Armando, M. Brehm, P. Steindl, M. T. Lusk, T. Fromherz, K. Schwarz and P. Blaha, *Phys. Rev. B*, 2021, **103**, 085310.
231 E. Cerrato, M. C. Paganini and E. Giamello, *J. Photochem. Photobiol., A*, 2020, **397**, 112531.

232 V. L. John, Y. Nair and T. P. Vinod, *Part. Part. Syst. Charact.*, 2021, **38**, 2100170.
233 N. Li, F. Lei, D. Xu, Y. Li, J. Liu and Y. Shi, *Opt. Mater.*, 2021, **111**, 110618.
234 B. Yang, X. Mao, F. Hong, W. Meng, Y. Tang, X. Xia, S. Yang, W. Deng and K. Han, *J. Am. Chem. Soc.*, 2018, **140**, 17001–17006.
235 C. Kang, S. Tao, F. Yang and B. Yang, *Aggregate*, 2022, **3**, e169.
236 Z. Zhu, Y. Zhai, Z. Li, P. Zhu, S. Mao, C. Zhu, D. Du, L. A. Belfiore, J. Tang and Y. Lin, *Mater. Today*, 2019, **30**, 52–79.
237 X.-D. Tang, H.-M. Yu, W. Nguyen, E. Amador, S.-P. Cui, K. Ma, M.-L. Chen, S.-Y. Wang, Z.-Z. Hu and W. Chen, *Adv. Photonics Res.*, 2023, **4**, 2200314.
238 Y. Liu, X. Kang, Y. Xu, Y. Li, S. Wang, C. Wang, W. Hu, R. Wang and J. Liu, *ACS Appl. Mater. Interfaces*, 2022, **14**, 22363–22371.
239 G. A. Medeiros, C. V. da Silva Rodrigues, J. Spencer and B. A. D. Neto, in *Quantum Materials, Devices, and Applications*, ed. M. Henini and M. O. Rodrigues, Elsevier, 2023, pp. 201–213, DOI: 10.1016/B978-0-12-820566-2.00004-1.
240 C. Han, Y.-H. Li, M.-Y. Qi, F. Zhang, Z.-R. Tang and Y.-J. Xu, *Sol. RRL*, 2020, **4**, 1900577.
241 H. A. Nguyen, I. Srivastava, D. Pan and M. Gruebele, *ACS Nano*, 2020, **14**, 6127–6137.
242 J. Shen, Y. Zhu, X. Yang, J. Zong, J. Zhang and C. Li, *New J. Chem.*, 2012, **36**, 97–101.
243 J. Shen, Y. Zhu, X. Yang and C. Li, *Chem. Commun.*, 2012, **48**, 3686–3699.
244 S. Ahirwar, S. Mallick and D. Bahadur, *ACS Omega*, 2017, **2**, 8343–8353.
245 M. Nirmal, C. B. Murray and M. G. Bawendi, *Phys. Rev. B: Condens. Matter Mater. Phys.*, 1994, **50**, 2293–2300.
246 J. E. Abraham and M. Balachandran, *J. Fluoresc.*, 2022, **32**, 887–906.
247 K. A. Wepasnick, B. A. Smith, K. E. Schrote, H. K. Wilson, S. R. Diegelmann and D. H. Fairbrother, *Carbon*, 2011, **49**, 24–36.
248 J. T. Paci, T. Belytschko and G. C. Schatz, *J. Phys. Chem. C*, 2007, **111**, 18099–18111.
249 T. Szabó, O. Berkesi, P. Forgó, K. Josepovits, Y. Sanakis, D. Petridis and I. Dékány, *Chem. Mater.*, 2006, **18**, 2740–2749.
250 P. Chingombe, B. Saha and R. J. Wakeman, *Carbon*, 2005, **43**, 3132–3143.
251 Z. Gan, H. Xu and Y. Hao, *Nanoscale*, 2016, **8**, 7794–7807.
252 C. Hu, M. Li, J. Qiu and Y.-P. Sun, *Chem. Soc. Rev.*, 2019, **48**, 2315–2337.
253 F. Vetrone, R. Naccache, V. Mahalingam, C. G. Morgan and J. A. Capobianco, *Adv. Funct. Mater.*, 2009, **19**, 2924–2929.
254 R. Arppe, I. Hyppänen, N. Perälä, R. Peltomaa, M. Kaiser, C. Würth, S. Christ, U. Resch-Genger, M. Schäferling and T. Soukka, *Nanoscale*, 2015, **7**, 11746–11757.
255 Z. Liu, H. Zou, N. Wang, T. Yang, Z. Peng, J. Wang, N. Li and C. Huang, *Sci. China: Chem.*, 2018, **61**, 490–496.
256 Y. Zhang, R. Yuan, M. He, G. Hu, J. Jiang, T. Xu, L. Zhou, W. Chen, W. Xiang and X. Liang, *Nanoscale*, 2017, **9**, 17849–17858.
257 S. Chen, N. Ullah, T. Wang and R. Zhang, *J. Mater. Chem. C*, 2018, **6**, 6875–6883.
258 L. Jia, W. Zheng and F. Huang, *PhotoniX*, 2020, **1**, 22.
259 H. Zhang, G. Chen and D. W. Bahnemann, *J. Mater. Chem.*, 2009, **19**, 5089–5121.
260 A. Alhebshi, E. Sharaf Aldeen, R. S. Mim, B. Tahir and M. Tahir, *Int. J. Energy Res.*, 2022, **46**, 5523–5584.
261 N. Joshi, *Photoconductivity: Art: Science & Technology*, CRC Press, 1990.
262 S. Wang, I. S. Cole, D. Zhao and Q. Li, *Nanoscale*, 2016, **8**, 7449–7458.
263 R. Wang, H. Fan, W. Jiang, G. Ni and S. Qu, *Appl. Surf. Sci.*, 2019, **467–468**, 446–455.
264 N. Dhenadhayalan, K.-C. Lin, R. Suresh and P. Ramamurthy, *J. Phys. Chem. C*, 2016, **120**, 1252–1261.
265 X. Zheng, Y. Huang, D. Xiao, S. Yang, Z. Lin and Q. Ling, *Mater. Chem. Front.*, 2021, **5**, 6960–6968.
266 B. Wang, Z. Wei, L. Sui, J. Yu, B. Zhang, X. Wang, S. Feng, H. Song, X. Yong, Y. Tian, B. Yang and S. Lu, *Light: Sci. Appl.*, 2022, **11**, 172.
267 H. Matsuo, Y. Noguchi and M. Miyayama, *Nat. Commun.*, 2017, **8**, 207.
268 P. N. O. Gillespie and N. Martsinovich, *ACS Appl. Mater. Interfaces*, 2019, **11**, 31909–31922.
269 L. Tang, L. Ai, Z. Song, L. Sui, J. Yu, X. Yang, H. Song, B. Zhang, Y. Hu, Y. Zhang, Y. Tian and S. Lu, *Adv. Funct. Mater.*, 2303363.
270 P. Lesani, Z. Lu, G. Singh, M. Mursi, M. Mirkhalaf, E. J. New and H. Zreiqat, *Nanoscale*, 2021, **13**, 11138–11149.
271 H. Wang, C. Sun, X. Chen, Y. Zhang, V. L. Colvin, Q. Rice, J. Seo, S. Feng, S. Wang and W. W. Yu, *Nanoscale*, 2017, **9**, 1909–1915.
272 P. R. Kharangarh, S. Umapathy and G. Singh, *Integr. Ferroelectr.*, 2017, **184**, 114–123.
273 X. Yang, X. Li, B. Wang, L. Ai, G. Li, B. Yang and S. Lu, *Chin. Chem. Lett.*, 2022, **33**, 613–625.
274 M. A. Sk, A. Ananthanarayanan, L. Huang, K. H. Lim and P. Chen, *J. Mater. Chem. C*, 2014, **2**, 6954–6960.
275 C. Huang, M. Feng, X. Zhu, Q. Zhou, S. Zeng, Y. Huang and H. Zhang, *Macromolecules*, 2021, **54**, 11497–11507.
276 G. Liu, D. Kong, J. Han, R. Zhou, Y. Gao, Z. Wu, L. Zhao, C. Wang, L. Wang and G. Lu, *Sens. Actuators, B*, 2021, **342**, 129963.
277 J. Zhan, B. Geng, K. Wu, G. Xu, L. Wang, R. Guo, B. Lei, F. Zheng, D. Pan and M. Wu, *Carbon*, 2018, **130**, 153–163.
278 T. Gao, X. Wang, L.-Y. Yang, H. He, X.-X. Ba, J. Zhao, F.-L. Jiang and Y. Liu, *ACS Appl. Mater. Interfaces*, 2017, **9**, 24846–24856.
279 L. Li and T. Dong, *J. Mater. Chem. C*, 2018, **6**, 7944–7970.
280 H. Ding, X.-H. Li, X.-B. Chen, J.-S. Wei, X.-B. Li and H.-M. Xiong, *J. Appl. Phys.*, 2020, **127**, 231101.
281 Y. Alqaheem and A. A. Alomair, *Membranes*, 2020, **10**, 33.

282 U. Issar and R. Arora, in *Environmental Applications of Carbon Nanomaterials-Based Devices*, 2021, pp. 395–422, DOI: 10.1002/9783527830978.ch17.
283 A. Kumar, S. Thota, S. Varma and J. Kumar, *J. Lumin.*, 2011, **131**, 640–648.
284 N. Soni, S. Singh, S. Sharma, G. Batra, K. Kaushik, C. Rao, N. C. Verma, B. Mondal, A. Yadav and C. K. Nandi, *Chem. Sci.*, 2021, **12**, 3615–3626.
285 D. Li, P. Jing, L. Sun, Y. An, X. Shan, X. Lu, D. Zhou, D. Han, D. Shen, Y. Zhai, S. Qu, R. Zbořil and A. L. Rogach, *Adv. Mater.*, 2018, **30**, 1705913.
286 H. Ding, S.-B. Yu, J.-S. Wei and H.-M. Xiong, *ACS Nano*, 2016, **10**, 484–491.
287 D. Gao, Y. Zhang, A. Liu, Y. Zhu, S. Chen, D. Wei, J. Sun, Z. Guo and H. Fan, *Chem. Eng. J.*, 2020, **388**, 124199.
288 K. Hola, A. B. Bourlinos, O. Kozak, K. Berka, K. M. Siskova, M. Havrdova, J. Tucek, K. Safarova, M. Otyepka, E. P. Giannelis and R. Zboril, *Carbon*, 2014, **70**, 279–286.
289 H. Ding, X.-X. Zhou, Z.-H. Zhang, Y.-P. Zhao, J.-S. Wei and H.-M. Xiong, *Nano Res.*, 2022, **15**, 3548–3555.
290 J. Tong, Y. Wang, J. Mei, J. Wang, A. Qin, J. Z. Sun and B. Z. Tang, *Chem. –Eur. J.*, 2014, **20**, 4661–4670.
291 A. Marini, A. Muñoz-Losa, A. Biancardi and B. Mennucci, *J. Phys. Chem. B*, 2010, **114**, 17128–17135.
292 P. Suppan, *J. Photochem. Photobiol., A*, 1990, **50**, 293–330.
293 S. Dhar, S. Singha Roy, D. K. Rana, S. Bhattacharya, S. Bhattacharya and S. C. Bhattacharya, *J. Phys. Chem. A*, 2011, **115**, 2216–2224.
294 Y. Hu, C. Neumann, L. Scholtz, A. Turchanin, U. Resch-Genger and S. Eigler, *Nano Res.*, 2023, **16**, 45–52.
295 J. Basavaraja, S. R. Inamdar and H. M. Suresh Kumar, *Spectrochim. Acta, Part A*, 2015, **137**, 527–534.
296 B. Omogo, J. F. Aldana and C. D. Heyes, *J. Phys. Chem. C*, 2013, **117**, 2317–2327.
297 H. Ding, J.-S. Wei, P. Zhang, Z.-Y. Zhou, Q.-Y. Gao and H.-M. Xiong, *Small*, 2018, **14**, 1800612.
298 D. Gao, A. Liu, Y. Zhang, Y. Zhu, D. Wei, J. Sun, H. Luo and H. Fan, *Chem. Eng. J.*, 2021, **415**, 128984.
299 S. Lin, C. Lin, M. He, R. Yuan, Y. Zhang, Y. Zhou, W. Xiang and X. Liang, *RSC Adv.*, 2017, **7**, 41552–41560.
300 M. Ö. Alaş and R. Genç, *ACS Appl. Nano Mater.*, 2021, **4**, 7974–7987.
301 R. Sato, Y. Iso and T. Isobe, *Langmuir*, 2019, **35**, 15257–15266.
302 S. Wu, W. Li, Y. Sun, X. Zhang, J. Zhuang, H. Hu, B. Lei, C. Hu and Y. Liu, *J. Colloid Interface Sci.*, 2019, **555**, 607–614.
303 J. Fan, W. Zhou, J. Chen, R. Liu, Q. Pang, L. Zhou, Z.-c. Wu and X. Zhang, *Ceram. Int.*, 2023, **49**, 23197–23205.
304 C. Hu, D. Liu, Y. Xiao and L. Dai, *Prog. Nat. Sci.: Mater. Int.*, 2018, **28**, 121–132.
305 Q. Xu, T. Kuang, Y. Liu, L. Cai, X. Peng, T. Sreenivasan Sreeprasad, P. Zhao, Z. Yu and N. Li, *J. Mater. Chem. B*, 2016, **4**, 7204–7219.
306 G. Yang, C. Wu, X. Luo, X. Liu, Y. Gao, P. Wu, C. Cai and S. S. Saavedra, *J. Phys. Chem. C*, 2018, **122**, 6483–6492.
307 S. Miao, K. Liang, J. Zhu, B. Yang, D. Zhao and B. Kong, *Nano Today*, 2020, **33**, 100879.
308 X. Feng, Y. Bai, M. Liu, Y. Li, H. Yang, X. Wang and C. Wu, *Energy Environ. Sci.*, 2021, **14**, 2036–2089.
309 B. B. Karakoçak, J. Liang, S. Kavadiya, M. Y. Berezin, P. Biswas and N. Ravi, *ACS Appl. Nano Mater.*, 2018, **1**, 3682–3692.
310 F. Du, Z. Cheng, Z. Lai, G. Ruan and C. Zhao, *New J. Chem.*, 2019, **43**, 18695–18701.
311 Y. Li, H. Lin, C. Luo, Y. Wang, C. Jiang, R. Qi, R. Huang, J. Travas-sejdic and H. Peng, *RSC Adv.*, 2017, **7**, 32225–32228.
312 M. Jiao, Y. Wang, W. Wang, X. Zhou, J. Xu, Y. Xing, L. Chen, Y. Zhang, M. Chen, K. Xu and S. Zheng, *Chem. Eng. J.*, 2022, **440**, 135965.
313 J. Liu, D. Li, K. Zhang, M. Yang, H. Sun and B. Yang, *Small*, 2018, **14**, 1703919.
314 V. Arul, P. Chandrasekaran, G. Sivaraman and M. G. Sethuraman, *Mater. Res. Bull.*, 2023, **162**, 112204.
315 M. Azami, J. Wei, M. Valizadehderakhshan, A. Jayapalan, O. O. Ayodele and K. Nowlin, *J. Phys. Chem. C*, 2023, **127**, 7360–7370.
316 Q. Zhang, R. Wang, B. Feng, X. Zhong and K. Ostrikov, *Nat. Commun.*, 2021, **12**, 6856.
317 W. Yang, H. Zhang, J. Lai, X. Peng, Y. Hu, W. Gu and L. Ye, *Carbon*, 2018, **128**, 78–85.
318 S. Tao, C. Zhou, C. Kang, S. Zhu, T. Feng, S.-T. Zhang, Z. Ding, C. Zheng, C. Xia and B. Yang, *Light: Sci. Appl.*, 2022, **11**, 56.
319 W. Wang, Y. Zhang and W. Liu, *Prog. Polym. Sci.*, 2017, **71**, 1–25.
320 H. Wang, B. Aydıner, Z. Seferoglu, F. Bureš and J. Liu, *Dyes Pigm.*, 2022, **205**, 110354.
321 B. Fei, Z. Yang, S. Shao, S. Wan and J. H. Xin, *Polymer*, 2010, **51**, 1845–1852.
322 H.-T. Feng, J. Zeng, P.-A. Yin, X.-D. Wang, Q. Peng, Z. Zhao, J. W. Y. Lam and B. Z. Tang, *Nat. Commun.*, 2020, **11**, 2617.
323 Y. Chen, G. Xiong, L. Zhu, J. Huang, X. Chen, Y. Chen and M. Cao, *ACS Omega*, 2022, **7**, 6834–6842.
324 R. Wang, Z. Huang, L. Ding, F. Yang and D. Peng, *ACS Appl. Nano Mater.*, 2022, **5**, 2214–2221.
325 P. Li and Z. Sun, *Light: Sci. Appl.*, 2022, **11**, 81.
326 M. Nieddu, M. Patrian, S. Ferrara, J. P. Fuenzalida Werner, F. Kohler, E. Anaya-Plaza, M. A. Kostiainen, H. Dietz, J. R. Berenguer and R. D. Costa, *Adv. Sci.*, 2023, **10**, 2300069.
327 A. Selim, S. Kaur, A. H. Dar, S. Sartaliya and G. Jayamurugan, *ACS Omega*, 2020, **5**, 22603–22613.
328 H. Faghihi, M. R. Mozafari, A. Bumrungpert, H. Parsaei, S. V. Taheri, P. Mardani, F. M. Dehkharghani, M. Y. Pudza and M. Alavi, *Photodiagn. Photodyn. Ther.*, 2023, **42**, 103614.
329 A. V. Nomoev, S. P. Bardakhanov, M. Schreiber, D. G. Bazarova, N. A. Romanov, B. B. Baldanov, B. R. Radnaev and V. V. Syzrantsev, *Beilstein J. Nanotechnol.*, 2015, **6**, 874–880.
330 X. He, Z. Zhao, L.-H. Xiong, P. F. Gao, C. Peng, R. S. Li, Y. Xiong, Z. Li, H. H. Y. Sung, I. D. Williams,

R. T. K. Kwok, J. W. Y. Lam, C. Z. Huang, N. Ma and B. Z. Tang, *J. Am. Chem. Soc.*, 2018, **140**, 6904–6911.
331 C. Wei, J. Li, X. Xiao, T. Yue and D. Zhao, *RSC Adv.*, 2018, **8**, 20016–20024.
332 X. Wu, F. Yu, Y. Han, L. Jiang, Z. Li, J. Zhu, Q. Xu, A. C. Tedesco, J. Zhang and H. Bi, *Nanoscale*, 2023, **15**, 376–386.
333 C. Li, Y. Zhu, X. Zhang, X. Yang and C. Li, *RSC Adv.*, 2012, **2**, 1765–1768.
334 Y. Lin, C. Wang, L. Li, H. Wang, K. Liu, K. Wang and B. Li, *ACS Appl. Mater. Interfaces*, 2015, **7**, 27262–27270.
335 Y.-P. Ho and K. W. Leong, *Nanoscale*, 2010, **2**, 60–68.
336 A. B. Cook and P. Decuzzi, *ACS Nano*, 2021, **15**, 2068–2098.
337 M. Goldsmith, L. Abramovitz and D. Peer, *ACS Nano*, 2014, **8**, 1958–1965.
338 P. Nayak, R. Nanda and M. Mishra, in *Medical Imaging Methods*, CRC Press, 2021, pp. 107–144.
339 M. Kim, J. Jang and C. Cha, *Drug Discovery Today*, 2017, **22**, 1430–1437.
340 B. Wang, H. Cai, G. I. N. Waterhouse, X. Qu, B. Yang and S. Lu, *Small Sci.*, 2022, **2**, 2200012.
341 L. Li, C. Lu, S. Li, S. Liu, L. Wang, W. Cai, W. Xu, X. Yang, Y. Liu and R. Zhang, *J. Mater. Chem. B*, 2017, **5**, 1935–1942.
342 S. Wang, B. Li and F. Zhang, *ACS Cent. Sci.*, 2020, **6**, 1302–1316.
343 J. Wallyn, N. Anton, S. Akram and T. F. Vandamme, *Pharm. Res.*, 2019, **36**, 78.
344 H. Li, X. Yan, D. Kong, R. Jin, C. Sun, D. Du, Y. Lin and G. Lu, *Nanoscale Horiz.*, 2020, **5**, 218–234.
345 L. Yue, H. Li, Q. Sun, J. Zhang, X. Luo, F. Wu and X. Zhu, *ACS Appl. Nano Mater.*, 2020, **3**, 869–876.
346 R. Su, H. Yan, X. Jiang, Y. Zhang, P. Li and W. Su, *J. Mater. Chem. B*, 2022, **10**, 1250–1264.
347 F. Huo, W. Liang, Y. Tang, W. Zhang, X. Liu, D. Pei, H. Wang, W. Jia, P. Jia and F. Yang, *J. Mater. Sci.*, 2019, **54**, 6815–6825.
348 C. Liu, W. Fan, W.-X. Cheng, Y. Gu, Y. Chen, W. Zhou, X.-F. Yu, M. Chen, M. Zhu, K. Fan and Q.-Y. Luo, *Adv. Funct. Mater.*, 2023, 2213856.
349 J. Ge, Q. Jia, W. Liu, M. Lan, B. Zhou, L. Guo, H. Zhou, H. Zhang, Y. Wang, Y. Gu, X. Meng and P. Wang, *Adv. Healthcare Mater.*, 2016, **5**, 665–675.
350 L. Jiang, H. Cai, W. Zhou, Z. Li, L. Zhang and H. Bi, *Adv. Mater.*, 2023, **35**, 2210776.
351 C. Liu, W. Fan, W.-X. Cheng, Y. Gu, Y. Chen, W. Zhou, X.-F. Yu, M. Chen, M. Zhu, K. Fan and Q.-Y. Luo, *Adv. Funct. Mater.*, 2023, **33**, 2213856.
352 D. Kim, H. G. Ryu and K. H. Ahn, *Org. Biomol. Chem.*, 2014, **12**, 4550–4566.
353 P. Lesani, A. H. Mohamad Hadi, Z. Lu, S. Palomba, E. J. New and H. Zreiqat, *Commun. Mater.*, 2021, **2**, 108.
354 H. Zhang, G. Wang, Z. Zhang, J. H. Lei, T.-M. Liu, G. Xing, C.-X. Deng, Z. Tang and S. Qu, *Light: Sci. Appl.*, 2022, **11**, 113.
355 L.-L. Feng, Y.-X. Wu, D.-L. Zhang, X.-X. Hu, J. Zhang, P. Wang, Z.-L. Song, X.-B. Zhang and W. Tan, *Anal. Chem.*, 2017, **89**, 4077–4084.
356 W.-S. Kuo, X.-C. Shen, C.-Y. Chang, H.-F. Kao, S.-H. Lin, J.-Y. Wang and P.-C. Wu, *ACS Nano*, 2020, **14**, 11502–11509.
357 Y. Liu, H. Gou, X. Huang, G. Zhang, K. Xi and X. Jia, *Nanoscale*, 2020, **12**, 1589–1601.
358 J. Gröhl, M. Schellenberg, K. Dreher and L. Maier-Hein, *Photoacoustics*, 2021, **22**, 100241.
359 C. Yang, H. Lan, F. Gao and F. Gao, *Photoacoustics*, 2021, **21**, 100215.
360 J. E. Lemaster and J. V. Jokerst, *Wiley Interdiscip. Rev.: Nanomed. Nanobiotechnology*, 2017, **9**, e1404.
361 J. Weber, P. C. Beard and S. E. Bohndiek, *Nat. Methods*, 2016, **13**, 639–650.
362 A. B. E. Attia, G. Balasundaram, M. Moothanchery, U. S. Dinish, R. Bi, V. Ntziachristos and M. Olivo, *Photoacoustics*, 2019, **16**, 100144.
363 M. Erfanzadeh and Q. Zhu, *Photoacoustics*, 2019, **14**, 1–11.
364 Y. Liu, P. Bhattarai, Z. Dai and X. Chen, *Chem. Soc. Rev.*, 2019, **48**, 2053–2108.
365 J. Ge, Q. Jia, W. Liu, L. Guo, Q. Liu, M. Lan, H. Zhang, X. Meng and P. Wang, *Adv. Mater.*, 2015, **27**, 4169–4177.
366 N. Parvin and T. K. Mandal, *Microchim. Acta*, 2017, **184**, 1117–1125.
367 Q. Jia, J. Ge, W. Liu, S. Liu, G. Niu, L. Guo, H. Zhang and P. Wang, *Nanoscale*, 2016, **8**, 13067–13077.
368 X. Bao, Y. Yuan, J. Chen, B. Zhang, D. Li, D. Zhou, P. Jing, G. Xu, Y. Wang, K. Holá, D. Shen, C. Wu, L. Song, C. Liu, R. Zbořil and S. Qu, *Light: Sci. Appl.*, 2018, **7**, 91.
369 W. Xu, J. Chen, S. Sun, Z. Tang, K. Jiang, L. Song, Y. Wang, C. Liu and H. Lin, *Nanoscale*, 2018, **10**, 17834–17841.
370 H. S. Jung, P. Verwilst, A. Sharma, J. Shin, J. L. Sessler and J. S. Kim, *Chem. Soc. Rev.*, 2018, **47**, 2280–2297.
371 H. Ma and M. Xue, *J. Mater. Chem. A*, 2021, **9**, 17569–17591.
372 F. A. Permatasari, H. Fukazawa, T. Ogi, F. Iskandar and K. Okuyama, *ACS Appl. Nano Mater.*, 2018, **1**, 2368–2375.
373 C. Scialabba, A. Sciortino, F. Messina, G. Buscarino, M. Cannas, G. Roscigno, G. Condorelli, G. Cavallaro, G. Giammona and N. Mauro, *ACS Appl. Mater. Interfaces*, 2019, **11**, 19854–19866.
374 M. Lan, S. Zhao, Z. Zhang, L. Yan, L. Guo, G. Niu, J. Zhang, J. Zhao, H. Zhang, P. Wang, G. Zhu, C.-S. Lee and W. Zhang, *Nano Res.*, 2017, **10**, 3113–3123.
375 Y. Weng, S. Guan, H. Lu, X. Meng, A. Y. Kaassis, X. Ren, X. Qu, C. Sun, Z. Xie and S. Zhou, *Talanta*, 2018, **184**, 50–57.
376 C. Hou, S. Chen and M. Wang, *Dalton Trans.*, 2018, **47**, 1777–1781.
377 P. Agostinis, K. Berg, K. A. Cengel, T. H. Foster, A. W. Girotti, S. O. Gollnick, S. M. Hahn, M. R. Hamblin, A. Juzeniene, D. Kessel, M. Korbelik, J. Moan, P. Mroz, D. Nowis, J. Piette, B. C. Wilson and J. Golab, *Ca-Cancer J. Clin.*, 2011, **61**, 250–281.
378 S. Kwiatkowski, B. Knap, D. Przystupski, J. Saczko, E. Kędzierska, K. Knap-Czop, J. Kotlińska, O. Michel, K. Kotowski and J. Kulbacka, *Biomed. Pharmacother.*, 2018, **106**, 1098–1107.
379 M. Lan, S. Zhao, W. Liu, C.-S. Lee, W. Zhang and P. Wang, *Adv. Healthcare Mater.*, 2019, **8**, 1900132.

380 J. Xie, Y. Wang, W. Choi, P. Jangili, Y. Ge, Y. Xu, J. Kang, L. Liu, B. Zhang, Z. Xie, J. He, N. Xie, G. Nie, H. Zhang and J. S. Kim, *Chem. Soc. Rev.*, 2021, **50**, 9152–9201.
381 J. Dobson, G. F. de Queiroz and J. P. Golding, *Vet. J.*, 2018, **233**, 8–18.
382 J. M. Dąbrowski and L. G. Arnaut, *Photochem. Photobiol. Sci.*, 2015, **14**, 1765–1780.
383 U. Chilakamarthi and L. Giribabu, *Chem. Rec.*, 2017, **17**, 775–802.
384 J. Zhao, F. Li, S. Zhang, Y. An and S. Sun, *New J. Chem.*, 2019, **43**, 6332–6342.
385 S. Yi, S. Deng, X. Guo, C. Pang, J. Zeng, S. Ji, H. Liang, X.-C. Shen and B.-P. Jiang, *Carbon*, 2021, **182**, 155–166.
386 Y. Xu, C. Wang, G. Ran, D. Chen, Q. Pang and Q. Song, *ACS Appl. Nano Mater.*, 2021, **4**, 4820–4828.
387 W. Liu, H. Gu, B. Ran, W. Liu, W. Sun, D. Wang, J. Du, J. Fan and X. Peng, *Sci. China Mater.*, 2022, **65**, 845–854.
388 J. Ge, M. Lan, B. Zhou, W. Liu, L. Guo, H. Wang, Q. Jia, G. Niu, X. Huang, H. Zhou, X. Meng, P. Wang, C.-S. Lee, W. Zhang and X. Han, *Nat. Commun.*, 2014, **5**, 4596.
389 S. Zhao, K. Yang, L. Jiang, J. Xiao, B. Wang, L. Zeng, X. Song and M. Lan, *ACS Appl. Nano Mater.*, 2021, **4**, 10528–10533.
390 D.-W. Zheng, B. Li, C.-X. Li, J.-X. Fan, Q. Lei, C. Li, Z. Xu and X.-Z. Zhang, *ACS Nano*, 2016, **10**, 8715–8722.
391 Y. Yang, H. Ding, Z. Li, A. C. Tedesco and H. Bi, *Molecules*, 2022, **27**, 8627.
392 H. Cai, X. Wu, L. Jiang, F. Yu, Y. Yang, Y. Li, X. Zhang, J. Liu, Z. Li and H. Bi, *Chin. Chem. Lett.*, 2023, 108946.
393 W. Fan, B. Yung, P. Huang and X. Chen, *Chem. Rev.*, 2017, **117**, 13566–13638.
394 J. Huo, Q. Jia, H. Huang, J. Zhang, P. Li, X. Dong and W. Huang, *Chem. Soc. Rev.*, 2021, **50**, 8762–8789.
395 Y. Bai, J. Zhao, S. Wang, T. Lin, F. Ye and S. Zhao, *ACS Appl. Mater. Interfaces*, 2021, **13**, 35365–35375.
396 V. R. Shinde, S. Khatun, A. M. Thanekar, A. Hak and A. K. Rengan, *Photodiagn. Photodyn. Ther.*, 2023, **41**, 103314.
397 Q. Jia, X. Zheng, J. Ge, W. Liu, H. Ren, S. Chen, Y. Wen, H. Zhang, J. Wu and P. Wang, *J. Colloid Interface Sci.*, 2018, **526**, 302–311.
398 S. Sun, J. Chen, K. Jiang, Z. Tang, Y. Wang, Z. Li, C. Liu, A. Wu and H. Lin, *ACS Appl. Mater. Interfaces*, 2019, **11**, 5791–5803.
399 L. Song, H. Cheng, Z. Ren, H. Wang, J. Lu, J. Zhang, Q. Zhao and S. Wang, *Colloids Surf., A*, 2023, **659**, 130763.
400 X. Chu, P. Zhang, Y. Wang, B. Sun, Y. Liu, Q. Zhang, W. Feng, Z. Li, K. Li, N. Zhou and J. Shen, *Carbon*, 2021, **176**, 126–138.
401 X. Wang, X. Zhong, F. Gong, Y. Chao and L. Cheng, *Mater. Horiz.*, 2020, **7**, 2028–2046.
402 R. Wang, Q. Liu, A. Gao, N. Tang, Q. Zhang, A. Zhang and D. Cui, *Nanoscale*, 2022, **14**, 12999–13017.
403 A. P. McHale, J. F. Callan, N. Nomikou, C. Fowley and B. Callan, in *Therapeutic Ultrasound*, ed. J.-M. Escoffre and A. Bouakaz, Springer International Publishing, Cham, 2016, pp. 429–450, DOI: 10.1007/978-3-319-22536-4_22.
404 X. Pan, H. Wang, S. Wang, X. Sun, L. Wang, W. Wang, H. Shen and H. Liu, *Sci. China: Life Sci.*, 2018, **61**, 415–426.
405 Y. Zhang, X. Zhang, H. Yang, L. Yu, Y. Xu, A. Sharma, P. Yin, X. Li, J. S. Kim and Y. Sun, *Chem. Soc. Rev.*, 2021, **50**, 11227–11248.
406 L. Rengeng, Z. Qianyu, L. Yuehong, P. Zhongzhong and L. Libo, *Photodiagn. Photodyn. Ther.*, 2017, **19**, 159–166.
407 Y.-Y. Ju, X.-X. Shi, S.-Y. Xu, X.-H. Ma, R.-J. Wei, H. Hou, C.-C. Chu, D. Sun, G. Liu and Y.-Z. Tan, *Adv. Sci.*, 2022, **9**, 2105034.
408 B. Geng, J. Hu, Y. Li, S. Feng, D. Pan, L. Feng and L. Shen, *Nat. Commun.*, 2022, **13**, 5735.
409 B. Wei, F. Dong, W. Yang, C. Luo, Q. Dong, Z. Zhou, Z. Yang and L. Sheng, *J. Adv. Res.*, 2020, **23**, 13–23.
410 M. J. Mitchell, M. M. Billingsley, R. M. Haley, M. E. Wechsler, N. A. Peppas and R. Langer, *Nat. Rev. Drug Discovery*, 2021, **20**, 101–124.
411 A. P. Subramanian, S. K. Jaganathan, A. Manikandan, K. N. Pandiaraj, N. Gomathi and E. Supriyanto, *RSC Adv.*, 2016, **6**, 48294–48314.
412 J. Ayub, M. U. Saeed, N. Hussain, I. Zulfiqar, T. Mehmood, H. M. N. Iqbal and M. Bilal, *Top. Catal.*, 2023, **66**, 625–648.
413 K. Ulbrich, K. Holá, V. Šubr, A. Bakandritsos, J. Tuček and R. Zbořil, *Chem. Rev.*, 2016, **116**, 5338–5431.
414 W. Su, R. Guo, F. Yuan, Y. Li, X. Li, Y. Zhang, S. Zhou and L. Fan, *J. Phys. Chem. Lett.*, 2020, **11**, 1357–1363.
415 W. Ren, F. Nan, S. Li, S. Yang, J. Ge and Z. Zhao, *ChemMedChem*, 2021, **16**, 646–653.
416 Z. Chen, T. Liao, L. Wan, Y. Kuang, C. Liu, J. Duan, X. Xu, Z. Xu, B. Jiang and C. Li, *Nano Res.*, 2021, **14**, 4264–4273.
417 H.-L. Cong, M.-Z. Wang, Y.-H. Xu, S. Wang, Y.-Q. Shen and B. Yu, *Integr. Ferroelectr.*, 2020, **206**, 151–159.
418 C. Anichini, W. Czepa, D. Pakulski, A. Aliprandi, A. Ciesielski and P. Samorì, *Chem. Soc. Rev.*, 2018, **47**, 4860–4908.
419 D. Sarkar, W. Liu, X. Xie, A. C. Anselmo, S. Mitragotri and K. Banerjee, *ACS Nano*, 2014, **8**, 3992–4003.
420 Y. Song, F. Chen, Y. Zhang, S. Zhang, F. Liu, P. Sun, X. Yan and G. Lu, *Sens. Actuators, B*, 2019, **287**, 191–198.
421 D. Wu, A. C. Sedgwick, T. Gunnlaugsson, E. U. Akkaya, J. Yoon and T. D. James, *Chem. Soc. Rev.*, 2017, **46**, 7105–7123.
422 Z. G. Khan and P. O. Patil, *Microchem. J.*, 2020, **157**, 105011.
423 L. A. Malik, A. Bashir, A. Qureashi and A. H. Pandith, *Environ. Chem. Lett.*, 2019, **17**, 1495–1521.
424 V. Singh and A. K. Mishra, *Sens. Actuators, B*, 2016, **227**, 467–474.
425 W. Gao, H. Song, X. Wang, X. Liu, X. Pang, Y. Zhou, B. Gao and X. Peng, *ACS Appl. Mater. Interfaces*, 2018, **10**, 1147–1154.
426 C. Tan, X. Su, C. Zhou, B. Wang, Q. Zhan and S. He, *RSC Adv.*, 2017, **7**, 40952–40956.
427 J. Zeng, L. Liao, X. Lin, G. Liu, X. Luo, M. Luo and F. Wu, *Int. J. Mol. Sci.*, 2022, **23**, 9213.
428 S. Pawar, S. Kaja and A. Nag, *ACS Omega*, 2020, **5**, 8362–8372.
429 A. Bhati, S. R. Anand, D. Saini, P. Khare, P. Dubey and S. K. Sonkar, *New J. Chem.*, 2018, **42**, 19548–19556.

430 A. Mirzaei, S. G. Leonardi and G. Neri, *Ceram. Int.*, 2016, **42**, 15119–15141.
431 C. Sonne, C. Xia, P. Dadvand, A. C. Targino and S. S. Lam, *J. Build. Eng.*, 2022, **62**, 105344.
432 D. Bharathi, B. Siddlingeshwar, R. H. Krishna, V. Singh, N. Kottam, D. D. Divakar and A. A. Alkheraif, *J. Fluoresc.*, 2018, **28**, 573–579.
433 Y. Hu, Z. Yang, X. Lu, J. Guo, R. Cheng, L. Zhu, C.-F. Wang and S. Chen, *Nanoscale*, 2020, **12**, 5494–5500.
434 B. Chen, L. Li, Y. Hu, B. Liu, M. Guo, Q. Zhang, Q. Yang and M. Zhang, *Microchem. J.*, 2022, **178**, 107350.
435 E. Martínez-Periñán, Á. Martínez-Sobrino, I. Bravo, T. García-Mendiola, E. Mateo-Martí, F. Pariente and E. Lorenzo, *Anal. Bioanal. Chem.*, 2022, **414**, 5537–5548.
436 R. Dai and Y. Hu, *Sens. Actuators, B*, 2022, **370**, 132420.
437 X. Zhu, X. Yuan, L. Han, H. Liu and B. Sun, *Biosens. Bioelectron.*, 2021, **191**, 113460.
438 J. Bai, Y. Ma, G. Yuan, X. Chen, J. Mei, L. Zhang and L. Ren, *J. Mater. Chem. C*, 2019, **7**, 9709–9718.
439 M. Zhang, R. Su, J. Zhong, L. Fei, W. Cai, Q. Guan, W. Li, N. Li, Y. Chen, L. Cai and Q. Xu, *Nano Res.*, 2019, **12**, 815–821.
440 Y. Chen, C. Wang, Y. Xu, G. Ran and Q. Song, *New J. Chem.*, 2020, **44**, 7210–7217.
441 J. Guo, W. Lu, Y. Meng, H. Wang, C. Dong and S. Shuang, *Dyes Pigm.*, 2022, **208**, 110766.
442 X. Ye, Y. Xiang, Q. Wang, Z. Li and Z. Liu, *Small*, 2019, **15**, 1901673.
443 J. Huang, Y. He, Z. Zhang, B. Lei and W. Wu, *J. Lumin.*, 2019, **215**, 116640.
444 L. Li, L. Shi, J. Jia, O. Eltayeb, W. Lu, Y. Tang, C. Dong and S. Shuang, *Sens. Actuators, B*, 2021, **332**, 129513.
445 M. Yu, H. Zhang, Y. Liu, Y. Zhang, M. Shang, L. Wang, Y. Zhuang and X. Lv, *Food Chem.*, 2022, **374**, 131768.
446 X. Wang, X. Teng, X. Sun, W. Pan and J. Wang, *Spectrochim. Acta, Part A*, 2022, **267**, 120547.
447 Y. Liu, J. Zhang, X. Zhao, W. Li, J. Wang, Y. Gao, Y. Cui, S. Xu and X. Luo, *Chem. Commun.*, 2020, **56**, 4074–4077.
448 Y. Chen, X. Sun, X. Wang, W. Pan, G. Yu and J. Wang, *Spectrochim. Acta, Part A*, 2020, **233**, 118230.
449 N. Zhao, J. Song, H. Ye and L. Zhao, *Colloids Surf., B*, 2023, **221**, 112985.
450 W. He, W. Weng, X. Sun, Y. Pan, X. Chen, B. Liu and J. Shen, *ACS Appl. Nano Mater.*, 2020, **3**, 7420–7427.
451 G. B. Nair and S. J. Dhoble, *Luminescence*, 2015, **30**, 1167–1175.
452 J. D. Bergesen, L. Tähkämö, T. Gibon and S. Suh, *J. Ind. Ecol.*, 2016, **20**, 263–275.
453 J. Cho, J. H. Park, J. K. Kim and E. F. Schubert, *Laser Photonics Rev.*, 2017, **11**, 1600147.
454 J. Legendre and P.-O. Chapuis, *Sol. Energy Mater. Sol. Cells*, 2022, **238**, 111594.
455 H. Xiang, R. Wang, J. Chen, F. Li and H. Zeng, *Light: Sci. Appl.*, 2021, **10**, 206.
456 L. Jin, L. Zhang, L. Yang, X. Wu, C. Zhang, K. Wei, L. He, X. Han, H. Qiao, A. M. Asiri, K. A. Alamry and K. Zhang, *J. Mater. Sci. Technol.*, 2020, **50**, 184–191.
457 B. Zhao and Z. a. Tan, *Adv. Sci.*, 2021, **8**, 2001977.
458 V. Singh and A. K. Mishra, *J. Mater. Chem. C*, 2016, **4**, 3131–3137.
459 X. Zhang, H. Yang, Z. Wan, T. Su, X. Zhang, J. Zhuang, B. Lei, Y. Liu and C. Hu, *Adv. Opt. Mater.*, 2020, **8**, 2000251.
460 W. Cai, T. Zhang, M. Xu, M. Zhang, Y. Guo, L. Zhang, J. Street, W.-J. Ong and Q. Xu, *J. Mater. Chem. C*, 2019, **7**, 2212–2218.
461 J. Zhu, X. Bai, X. Chen, Z. Xie, Y. Zhu, G. Pan, Y. Zhai, H. Zhang, B. Dong and H. Song, *Dalton Trans.*, 2018, **47**, 3811–3818.
462 Y. Zhai, Y. Wang, D. Li, D. Zhou, P. Jing, D. Shen and S. Qu, *J. Colloid Interface Sci.*, 2018, **528**, 281–288.
463 Y. An, X. Lin, Z. Guo, Q. Yin, Y. Li, Y. Zheng, Z. Shi, W. Zhang and C. Liu, *Materials*, 2021, **14**, 4716.
464 R. Kumari, A. Kumar, K. Negi and S. K. Sahu, *ACS Appl. Nano Mater.*, 2023, **6**, 918–929.
465 X. Yang and D. Wang, *ACS Appl. Energy Mater.*, 2018, **1**, 6657–6693.
466 M. B. Tahir, M. Sohaib, M. Sagir and M. Rafique, in *Encyclopedia of Smart Materials*, ed. A.-G. Olabi, Elsevier, Oxford, 2022, pp. 578–589.
467 A. J. Bard, *Science*, 1980, **207**, 139–144.
468 C. Kerzig and M. Goez, *Chem. Sci.*, 2016, **7**, 3862–3868.
469 E. Contreras, C. Palacios, I. B. Becerril-Castro and J. M. Romo-Herrera, *Micromachines*, 2021, **12**, 577.
470 Z. Zhang, G. Yi, P. Li, X. Zhang, H. Fan, Y. Zhang, X. Wang and C. Zhang, *Nanoscale*, 2020, **12**, 13899–13906.
471 R. Aggarwal, D. Saini, B. Singh, J. Kaushik, A. K. Garg and S. K. Sonkar, *Sol. Energy*, 2020, **197**, 326–331.
472 P. Khare, A. Bhati, S. R. Anand, Gunture and S. K. Sonkar, *ACS Omega*, 2018, **3**, 5187–5194.
473 H. Li, R. Liu, S. Lian, Y. Liu, H. Huang and Z. Kang, *Nanoscale*, 2013, **5**, 3289–3297.
474 D.-X. Yang, D. Qu, X. Miao, W.-S. Jiang, L. An, Y.-J. Wen, D.-D. Wu and Z.-C. Sun, *Rare Met.*, 2019, **38**, 404–412.
475 N. Kannan and D. Vakeesan, *Renewable Sustainable Energy Rev.*, 2016, **62**, 1092–1105.
476 Z. Fan, Y. Zhao, X. Liu, Y. Shi and D. Jiang, *RSC Adv.*, 2022, **12**, 12303–12309.
477 M. B. Hayat, D. Ali, K. C. Monyake, L. Alagha and N. Ahmed, *Int. J. Energy Res.*, 2019, **43**, 1049–1067.
478 J. Hu, X. Xiong, W. Guan and H. Long, *Mater. Today Energy*, 2021, **21**, 100769.
479 M. O. Alas, F. B. Alkas, A. Aktas Sukuroglu, R. Genc Alturk and D. Battal, *J. Mater. Sci.*, 2020, **55**, 15074–15105.
480 M. G. Debije, R. C. Evans and G. Griffini, *Energy Environ. Sci.*, 2021, **14**, 293–301.
481 G. Liu, M. Zavelani-Rossi, G. Han, H. Zhao and A. Vomiero, *J. Mater. Chem. A*, 2023, **11**, 8950–8960.
482 Y. Han, X. Zhao, A. Vomiero, X. Gong and H. Zhao, *J. Mater. Chem. C*, 2021, **9**, 12255–12262.
483 K.-B. Cai, H.-Y. Huang, M.-L. Hsieh, P.-W. Chen, S.-E. Chiang, S. H. Chang, J.-L. Shen, W.-R. Liu and C.-T. Yuan, *ACS Nano*, 2022, **16**, 3994–4003.
484 J. Li, H. Zhao, X. Zhao and X. Gong, *Nanoscale*, 2021, **13**, 9561–9569.

485 M. Ali, A. S. Anjum, R. Riaz, A. Bibi, K. C. Sun and S. H. Jeong, *Carbon*, 2021, **181**, 155–168.
486 T. Dey, A. Ghorai, S. Das and S. K. Ray, *Sol. Energy*, 2022, **236**, 17–25.
487 W. Hong, Z. Yuan and X. Chen, *Small*, 2020, **16**, 1907626.
488 C. Yang, F. Guo, S. Wang, W. Chen, Y. Zhang, N. Wang, Z. Li and J. Wang, *RSC Adv.*, 2023, **13**, 10884–10892.
489 K. Y. Jung, *RSC Adv.*, 2020, **10**, 16323–16329.
490 S. Hussain, S. Haider, W. Al-Masry and S.-Y. Park, *RSC Adv.*, 2021, **11**, 37498–37503.
491 M. Li, W. Yao, J. Liu, Q. Tian, L. Liu, J. Ding, Q. Xue, Q. Lu and W. Wu, *J. Mater. Chem. C*, 2017, **5**, 6512–6520.
492 X. Yu, H. Zhang and J. Yu, *Aggregate*, 2021, **2**, 20–34.
493 P. Kumar, S. Singh and B. K. Gupta, *Nanoscale*, 2016, **8**, 14297–14340.
494 J. Wang, J. Ma, J. Zhang, Y. Fan, W. Wang, J. Sang, Z. Ma and H. Li, *ACS Appl. Mater. Interfaces*, 2019, **11**, 35871–35878.
495 A. Mondal and P. Chattopadhyay, *New J. Chem.*, 2023, **47**, 4984–4991.
496 X.-f. Li, W. Zhou, Y.-c. Liu, M. Hou, G.-l. Feng, Y.-m. Ji, Y. Zhang and G.-w. Xing, *Chem. Commun.*, 2022, **58**, 11547–11550.
497 Z. Fatahi, N. Esfandiari and Z. Ranjbar, *J. Anal. Test.*, 2020, **4**, 307–315.
498 J. Guo, H. Li, L. Ling, G. Li, R. Cheng, X. Lu, A.-Q. Xie, Q. Li, C.-F. Wang and S. Chen, *ACS Sustain. Chem. Eng.*, 2020, **8**, 1566–1572.
499 Y. Ni, H. Wan, W. Liang, S. Zhang, X. Xu, L. Li, Y. Shao, S. Ruan and W. Zhang, *Nanoscale*, 2021, **13**, 16872–16878.
500 X.-Y. Dong, X.-Q. Niu, Z.-Y. Zhang, J.-S. Wei and H.-M. Xiong, *ACS Appl. Mater. Interfaces*, 2020, **12**, 29549–29555.
501 K. Yuan, X. Zhang, X. Li, R. Qin, Y. Cheng, L. Li, X. Yang, X. Yu, Z. Lu and H. Liu, *Chem. Eng. J.*, 2020, **397**, 125487.
502 H. Yang, Y. Liu, Z. Guo, B. Lei, J. Zhuang, X. Zhang, Z. Liu and C. Hu, *Nat. Commun.*, 2019, **10**, 1789.
503 B. Liao, W. Wang, P. Long, X. Deng, B. He, Q. Liu and S. Yi, *Carbon*, 2015, **91**, 30–37.
504 H. Wei, Y. Zheng, X. Zhang, P. Liang, X. Xu, C. Hu, X. Zhang, B. Lei, Y. Liu and J. Zhuang, *Mater. Adv.*, 2022, **3**, 4542–4547.
505 D. Gust, T. A. Moore and A. L. Moore, *Faraday Discuss.*, 2012, **155**, 9–26.
506 N. Abas, E. Kalair, A. Kalair, Q. u. Hasan and N. Khan, *Int. J. Hydrogen Energy*, 2020, **45**, 20787–20799.
507 R. L. House, N. Y. M. Iha, R. L. Coppo, L. Alibabaei, B. D. Sherman, P. Kang, M. K. Brennaman, P. G. Hoertz and T. J. Meyer, *J. Photochem. Photobiol., C*, 2015, **25**, 32–45.
508 J. Su and L. Vayssieres, *ACS Energy Lett.*, 2016, **1**, 121–135.
509 T. Butburee, P. Chakthranont, C. Phawa and K. Faungnawakij, *ChemCatChem*, 2020, **12**, 1873–1890.
510 D. K. Dogutan and D. G. Nocera, *Acc. Chem. Res.*, 2019, **52**, 3143–3148.
511 A. J. Simkin, M. Faralli, S. Ramamoorthy and T. Lawson, *Plant J.*, 2020, **101**, 1001–1015.
512 S. Berardi, S. Drouet, L. Francàs, C. Gimbert-Suriñach, M. Guttentag, C. Richmond, T. Stoll and A. Llobet, *Chem. Soc. Rev.*, 2014, **43**, 7501–7519.
513 A. C. Benniston and A. Harriman, *Mater. Today*, 2008, **11**, 26–34.
514 Z. Wang, Y. Hu, S. Zhang and Y. Sun, *Chem. Soc. Rev.*, 2022, **51**, 6704–6737.
515 B. Guo, G. Liu, H. Wei, J. Qiu, J. Zhuang, X. Zhang, M. Zheng, W. Li, H. Zhang and C. Hu, *SmartMat*, 2022, **3**, 208–225.
516 Z. Wang, Y. Zhang, S. Zhang, M. Ge, H. Zhang, S. Wang, Z. Chen, S. Li and C. Yang, *J. Colloid Interface Sci.*, 2023, **629**, 12–21.
517 Z. Hallaji, Z. Bagheri, Z. Tavassoli and B. Ranjbar, *Sustainable Mater. Technol.*, 2022, **34**, e00493.
518 X. Xu, X. Mao, J. Zhuang, B. Lei, Y. Li, W. Li, X. Zhang, C. Hu, Y. Fang and Y. Liu, *ACS Sustain. Chem. Eng.*, 2020, **8**, 3938–3949.
519 C. Wang, H. Yang, F. Chen, L. Yue, Z. Wang and B. Xing, *Environ. Sci. Technol.*, 2021, **55**, 12317–12325.
520 D. Li, W. Li, H. Zhang, X. Zhang, J. Zhuang, Y. Liu, C. Hu and B. Lei, *ACS Appl. Mater. Interfaces*, 2020, **12**, 21009–21019.
521 X. Xu, W. Li, C. Hu, B. Lei, X. Zhang, Y. Li, Q. Zhan, Y. Liu and J. Zhuang, *ACS Sustain. Chem. Eng.*, 2020, **8**, 9751–9762.
522 Y. Wang, Z. Xie, X. Wang, X. Peng and J. Zheng, *J. Nanobiotechnol.*, 2021, **19**, 260.
523 D. Xiao, M. Jiang, X. Luo, S. Liu, J. Li, Z. Chen and S. Li, *ACS Sustain. Chem. Eng.*, 2021, **9**, 4139–4145.
524 T. Iizuka, H. Sezutsu, K.-i. Tatematsu, I. Kobayashi, N. Yonemura, K. Uchino, K. Nakajima, K. Kojima, C. Takabayashi, H. Machii, K. Yamada, H. Kurihara, T. Asakura, Y. Nakazawa, A. Miyawaki, S. Karasawa, H. Kobayashi, J. Yamaguchi, N. Kuwabara, T. Nakamura, K. Yoshii and T. Tamura, *Adv. Funct. Mater.*, 2013, **23**, 5232–5239.
525 D. W. Kim, O. J. Lee, S.-W. Kim, C. S. Ki, J. R. Chao, H. Yoo, S.-i. Yoon, J. E. Lee, Y. R. Park, H. Kweon, K. G. Lee, D. L. Kaplan and C. H. Park, *Biomaterials*, 2015, **70**, 48–56.
526 S. B. Bon, I. Chiesa, M. Degli Esposti, D. Morselli, P. Fabbri, C. De Maria, A. Morabito, R. Coletta, M. Calamai, F. S. Pavone, R. Tonin, A. Morrone, G. Giorgi and L. Valentini, *ACS Appl. Mater. Interfaces*, 2021, **13**, 21007–21017.
527 W. Chen, Y. Zhong, G. Fu, W. Lai, Z. Pan, Y. Yang, F. Chen and H. Yan, *Coatings*, 2023, **13**, 31.
528 S. Fan, X. Zheng, Q. Zhan, H. Zhang, H. Shao, J. Wang, C. Cao, M. Zhu, D. Wang and Y. Zhang, *Nano-Micro Lett.*, 2019, **11**, 75.
529 Q. Zhan, S. Fan, D. Wang, X. Yao, H. Shao and Y. Zhang, *Compos. Commun.*, 2020, **21**, 100414.
530 X. Zheng, M. Zhao, H. Zhang, S. Fan, H. Shao, X. Hu and Y. Zhang, *ACS Biomater. Sci. Eng.*, 2018, **4**, 4021–4027.
531 M. J. Haskew, B. Deacon, C. W. Yong, J. G. Hardy and S. T. Murphy, *ACS Omega*, 2021, **6**, 35494–35504.
532 N. C. Tansil, L. D. Koh and M.-Y. Han, *Adv. Mater.*, 2012, **24**, 1388–1397.

533 J. Liu, T. Kong and H.-M. Xiong, *Adv. Mater.*, 2022, **34**, 2200152.
534 E. S. Maltseva, V. O. Nikolaeva, A. M. Savin, M. Y. Dobryakov, E. I. Koshel, P. V. Krivoshapkin and E. F. Krivoshapkina, *ACS Biomater. Sci. Eng.*, 2022, **8**, 3310–3319.
535 K. Xue, C. Wang, J. Wang, S. Lv, B. Hao, C. Zhu and B. Z. Tang, *J. Am. Chem. Soc.*, 2021, **143**, 14147–14157.
536 X. Liu, X. Tang, Y. Hou, Q. Wu and G. Zhang, *RSC Adv.*, 2015, **5**, 81713–81722.
537 S. Kalytchuk, K. Poláková, Y. Wang, J. P. Froning, K. Cepe, A. L. Rogach and R. Zbořil, *ACS Nano*, 2017, **11**, 1432–1442.
538 C.-Y. Chen and C.-T. Chen, *Chem. Commun.*, 2011, **47**, 994–996.
539 J. Zhou, B. del Rosal, D. Jaque, S. Uchiyama and D. Jin, *Nat. Methods*, 2020, **17**, 967–980.
540 H. Gao, C. Kam, T. Y. Chou, M.-Y. Wu, X. Zhao and S. Chen, *Nanoscale Horiz.*, 2020, **5**, 488–494.
541 V. Kalaparthi, B. Peng, S. A. M. A. Peerzade, S. Palantavida, B. Maloy, M. E. Dokukin and I. Sokolov, *Nanoscale Adv.*, 2021, **3**, 5090–5101.
542 J.-R. Macairan, D. B. Jaunky, A. Piekny and R. Naccache, *Nanoscale Adv.*, 2019, **1**, 105–113.
543 C. Wang, T. Hu, T. Thomas, S. Song, Z. Wen, C. Wang, Q. Song and M. Yang, *Nanoscale*, 2018, **10**, 21809–21817.
544 Y. Xu, Y. Yang, S. Lin and L. Xiao, *Anal. Chem.*, 2020, **92**, 15632–15638.
545 Q. Wang, Z. Tang, L. Li, J. Guo, L. Jin, J. Lu, P. Huang, S. Zhang and L. Jiao, *Spectrochim. Acta, Part A*, 2022, **280**, 121538.
546 B. H. Lee, R. L. McKinney, M. T. Hasan and A. V. Naumov, *Materials*, 2021, **14**, 616.
547 C. Wang, K. Jiang, Q. Wu, J. Wu and C. Zhang, *Chem. –Eur. J.*, 2016, **22**, 14475–14479.